Theses and Dissertations

Fall 2017

Automated image analysis of corneal structures in anterior-segment optical coherence tomography and in-vivo confocal microscopy images

Victor Adrian Robles
University of Iowa

Recommended Citation

AUTOMATED IMAGE ANALYSIS OF CORNEAL STRUCTURES IN
ANTERIOR-SEGMENT OPTICAL COHERENCE TOMOGRAPHY AND
IN-VIVO CONFOCAL MICROSCOPY IMAGES

by

Victor Adrian Robles

A thesis submitted in partial fulfillment of the
requirements for the Doctor of Philosophy degree
in Electrical and Computer Engineering
in the Graduate College of
The University of Iowa

December 2017

Thesis Supervisor: Associate Professor Mona K. Garvin

Graduate College
The University of Iowa
Iowa City, Iowa

CERTIFICATE OF APPROVAL

_____

PH.D. THESIS

_____

This is to certify that the Ph.D. thesis of

Victor Adrian Robles

has been approved by the Examining Committee for the thesis requirement for the Doctor of Philosophy degree in Electrical and Computer Engineering at the December 2017 graduation.

Thesis Committee: _____
                  Mona K. Garvin, Thesis Supervisor

                  _____
                  Michael G. Anderson

                  _____
                  Mathews Jacob

                  _____
                  Todd Scheetz

                  _____
                  Xiaodong Wu

ACKNOWLEDGEMENTS

It is a great honor to be here right now reflecting upon the personal and professional relationships I've developed throughout the years. It has been a true blessing to see my peers come and go as they also begin and end their academic journeys. But to finally be one among them here sharing similar accomplishments is an honor I never thought I'd reach.

First and foremost, I want to thank Dr. Mona K. Garvin, a mentor, an advisor, and a friend. Without her guidance through all aspects of my graduate school life I would be but another speck of dust in this world, I mean, I'm still but a speck of dust in this world, but possibly a speck with a Ph.D. too. I also want to thank my committee for whom I've had the pleasure of interacting with in regards to all aspects of my academic life here. Dr. Michael G. Anderson, a lot of the voluntary work your team contributed for the completion of my thesis is something I will never take for granted and I hope to one day be able to repay in kind. Dr. Mathews Jacob, on my very first day of graduate school as I walked into your DSP course you boosted my confidence in understanding course material due to the effectiveness of your teaching style ultimately leading to the completion of my coursework with a 4.0 GPA, something that I considered truly beyond me. Dr. Todd Scheetz, there isn't a single statistical test that passes by me that I won't first verify in regards to power and effectiveness thanks to you. A notable moment that comes to mind is when, during my comprehensive exam, you asked me to calculate the Bonferroni correction for a theoretical example you proposed as I sat there frozen trying to multiply 3 by 9. Dr. Xiaodong Wu, I recall when Dr. Garvin first showed me your foundational and groundbreaking work in the field of graph-theoretic image segmentation. Wrapping my head around your work was one of the most difficult challenges for me here at UIowa. But I think I did ok for myself, having implemented a piece of it in some of my thesis work. Special thanks also to Dr. Randy Kardon, Jan M. Full, and Brice Critser for providing the quintessential

data necessary for me to be able to complete my thesis.

My list of colleagues and friends goes beyond anything an acknowledgments page can probably handle but I don't know where I'd be without the support of my friends and lab mates. Bhavna J. Antony, Jui-Kai Wang, Qiao Hu, Wenxiang Deng, Jason Agne, Mohammad Shafkat, John Miller, Mohammad Saleh Miri, Qingyang Su, Yashila Permeswaran, and Sam Johnson. Thank you all for making sure my time in the lab was not a lonely one.

Last, but definitely not least, is my one and only, my fiancée Christina Douglas who has stayed by my side throughout the 11 years of my journey in higher education and post-graduate work moving across the country in the process. Sticking with me through thick and thin. Thank you for all that you do.

ABSTRACT

Optical Coherence Tomography (OCT) is a noninvasive imaging modality that has significantly contributed to the quantitative assessment of ocular diseases. Another tool available to ophthalmic clinicians is in-vivo confocal microscopy, which allows anatomical structures to be observed live at the cellular level. Incorporating both of these modalities for imaging the cornea allows us to take structural measurements to characterize disease-related changes in corneal anatomy.

Notable diseases that directly impact or correlate with corneal structures include glaucoma and diabetic neuropathy. Given glaucoma's impact as the second leading cause of blindness in the world, great efforts have been made in researching and understanding the disease. Correlations have been found between the central corneal thickness (CCT) and the risk of developing visual field loss in patients diagnosed with glaucoma. It should come as no surprise that measuring CCT among glaucoma suspects has also now become a clinical standard of practice. Diabetes is a group of metabolic diseases where the body experiences high blood sugar levels over prolonged periods of time. It is a prominent disease that affects millions of Americans each day. While not necessarily an ocular disease in its own right, it has been shown that diabetes can still affect the corneal structures. Diabetics have decreased corneal sensitivity and a significant link has been established between neuropathic severity in diabetic patients and corneal nerve fiber density.

Given the availability of these imaging tools and the significant impact these prominent diseases have on society, a growing focus has developed on relating corneal structure measurements and ophthalmic diseases. However, manually acquiring structural measures of the cornea can be a labor-intensive and daunting task. Hence, experts have sought to develop automatic alternatives. The goals of our work include the ability to automatically segment the corneal structures from anterior segment-optical coherence tomography (AS-OCT) and in-vivo confocal microscopy (IVCM) to provide useful structural information from the cornea.

iv

The major contributions of this work include 1) utilizing the 3D information of AS-OCT imagery to segment the cornea layers simultaneously, 2) increasing the region-of-interest of IVCM imagery using a feature-based registration approach to develop a panorama from the images, 3) incorporating machine-learning techniques to segment the corneal nerves in the IVCM imagery, and 4) extracting structural measurements from the segmentation results to determine the correlation between the corneal structural measurements in various subject groups.

PUBLIC ABSTRACT

Anterior-Segment-Optical Coherence Tomography (AS-OCT) is a noninvasive imaging modality that has significantly contributed to the quantitative assessment of ocular diseases. Another tool available to ophthalmic clinicians is in-vivo confocal microscopy (IVCM), which allows anatomical structures to be observed live at the cellular level. Incorporating both of these modalities for imaging the cornea allows us to take structural measurements and characterize disease-related changes in corneal anatomy.

Notable diseases that directly impact or correlate with corneal structures include glaucoma and diabetic neuropathy. Given glaucoma's impact as the second leading cause of blindness in the world, great efforts have been made in researching and understanding the disease. Diabetes is a prominent disease that affects millions of Americans every day. While not necessarily a corneal disease in its own right, diabetes has been shown to affect the corneal structures. Diabetics have decreased corneal sensitivity and a significant link has been established between neuropathic severity in diabetic patients and corneal nerve fiber density.

Given the availability of these imaging tools and the significant impact these prominent diseases have on society a growing focus has developed on relating corneal structure measurements and ophthalmic diseases. However, manually acquiring structural measures of the cornea can be a labor-intensive and daunting task. Hence, experts have sought to develop automatic alternatives. The goals of this work include 1) utilizing the 3D information of AS-OCT imagery to segment all the corneal layers simultaneously, 2) increasing the region-of-interest of IVCM imagery using a feature-based registration approach to develop a panorama from the images, 3) incorporating machine-learning techniques to segment the corneal nerves in the IVCM imagery, and 4) extracting structural measurements from the segmentation results to determine correlation between the corneal structural measurements in various subject groups.

TABLE OF CONTENTS

LIST OF TABLES

LIST OF FIGURES

CHAPTER 1
INTRODUCTION

Optical Coherence Tomography (OCT) is an imaging technique that was first introduced in 1991 [1] to take high-resolution cross-sectional images of the retina. It was also to be later described for use in imaging the anterior segment of the eye, namely the cornea and its layers [2]. It is a noninvasive imaging modality that has significantly contributed to the quantitative assessment of ocular diseases. An example of an anterior segment-OCT (AS-OCT) image can be seen in Fig. 1.1a. With the introduction of spectral-domain OCT in 2007 a few options opened up for commercial products. This modality and its products have allowed for true volumetric imaging of the corneal layers to become more readily available.

Another noninvasive tool available to ophthalmic clinicians is the confocal microscope. In 1955, Marvin Lee Minsky proposed a modification to the traditional specular microscope wherein both the illumination (condenser) and observation (objective) system could be focused on a single point. This modification led to the development of the confocal microscope [4]. This increased resolution to an order of 1-2 μm laterally and 5-10 μm axially. As a result, anatomical structures could now be observed in situ at the cellular level [5] which in turn gave way to in-vivo confocal microscopy imaging (IVCM) modalities. An example of this imaging modality for the cornea is shown in Fig. 1.1b

Notable diseases that directly impact or correlate with corneal structures include glaucoma and diabetic neuropathy. Glaucoma is a group of ocular disorders that lead to progressive damage to the optic nerve ultimately resulting in loss of vision. It is the second leading cause of blindness in the U.S. affecting approximately 1-2% of our population [6, 7]. Correlations have been found between the central corneal thickness (CCT) and the risk of developing visual field loss in patients diagnosed with glaucoma [8]. Thus measuring CCT among glaucoma suspects using pachymetry has
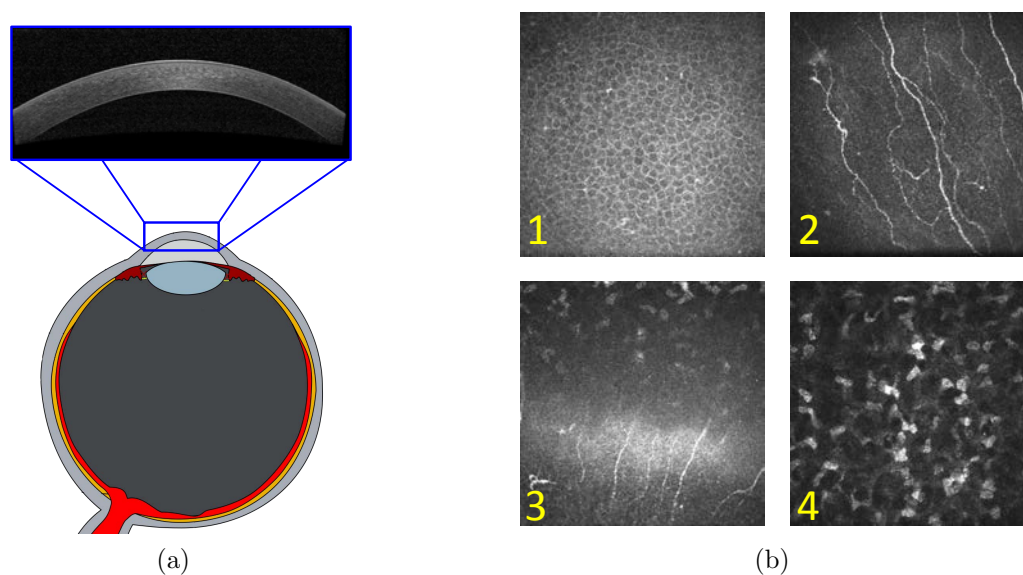
Figure 1.1: Subfigure (a) shows a 2D image of the cornea and a respective OCT slice (corneal cross-sectional image courtesy of [3]). Subfigure (b) shows 2D images of the 1) corneal epithelium 2) sub-basal nerve plexus 3) stroma and 4) deep stromal keratocytes acquired using confocal microscopy.

become a clinical standard of practice. Diabetes is a group of metabolic diseases where the body experiences high blood sugar levels over prolonged periods of time. It is a prominent disease that affects 29.1 million Americans [9]. A debilitating complication of this disease is diabetic neuropathy which affects the peripheral nervous system wherein advanced cases can lead to lower limb amputations. Patients with diabetes are known to have decreased corneal sensitivity [10] and a significant link has been established between neuropathic severity in diabetic patients and corneal nerve fiber density [11].

Given the availability of these imaging tools, and the significant impact these prominent diseases have on society, a growing focus has developed on relating corneal structure measurements and ophthalmic diseases. However, manually acquiring structural measures of the cornea can be a labor-intensive and daunting task. Hence, ex-

perts have sought to develop automatic alternatives. In the case of using AS-OCT imaging modalities to automatically segment corneal layers [12–20], only our previous works [15] have utilized using the information from the entire volume to segment multiple layers simultaneously and in 3D. Additionally, while methodologies exist to segment the corneal fiber layers in IVCM images [21–27] very little exists for creating a montage of such images [28–30] and to the best of our knowledge, only one other work exists that combines segmentation and registration techniques to segment montage images [31].

1.1   Thesis Aims

Our contributions utilize the 3D information of AS-OCT images, multiple regions of interests of the same scene spanning from stitching IVCM images, and the structural measures of the cornea for inter-structure and intra-structure statistical analysis among various subject groups. Our work is composed of three major aims. First an algorithm for the segmentation of corneal layers in AS-OCT images was developed. Secondly, an algorithm that automatically stitched multiple images of the corneal sub-basal nerve plexus and automatically segments corneal nerves in IVCM images was developed. Finally, these segmentation results were used to obtain structural measurements to determine correlations and statistical significance in and across the imaging modalities among various subject groups. Our specific aims are as follows:

- **Aim 1: Develop an algorithm that segments the corneal layers in the eye using AS-OCT of humans and mice.** This aim was completed by applying a 3D graph-based approach to segment the corneal layers. The surface segmentation problem was transformed into an optimization problem and solved using a graph-theoretic algorithm. The approach was designed to utilize the shape-prior information of the cornea to segment three surface boundaries in mice and humans, with all layers segmented simultaneously in 3D.

- **Aim 2: Develop an algorithm that creates a montage of in-vivo confocal microscopy (IVCM) images of the corneal sub-basal nerve plexus and segments the corneal nerves in the montage image.** This aim was completed by applying a feature-based approach to find the best matching features between multiple, corresponding 2D confocal corneal nerve images to register and stitch the images together. The method used a combination of features from accelerated segment test (FAST), histogram of oriented gradients (HOG) and random sample consensus (RANSAC) parameter estimation to construct an image with an increased field of view of the corneal nerves. Morphological operations and filter banks were also used as features for a machine learning technique to segment the corneal nerves across single images and montages developed from the imagery.

- **Aim 3: Determine the correlation and statistical significance of structural measures of the cornea from multiple imaging modalities for use in observing ophthalmic diseases known to affect the corneal nerves.** In this aim, we utilized AS-OCT and IVCM data from three subject groups: normal subjects, patients with diabetes, and patients with trigeminal nerve damage. We applied the methodologies of segmenting corneal structures as implemented in earlier aims to extract structural measurements, including the corneal thickness of the different layers and corneal nerve fiber density. We compared inter-group and intra-group corneal structural measurements to determine any statistical significance and correlations herein.

1.2 Thesis Overview

This thesis is organized into seven remaining chapters as follows:

- Chapter 2 provides clinical background specific to the anatomical structures incorporated in these works as well as some of the clinical motivation behind

our research.

- Chapter 3 summarizes the previous works in AS-OCT segmentation of the corneal layers and the image stitching and segmentation of IVCM of the sub-basal nerve plexus along with an overview of the graph-theoretic approach incorporated into our work and the previous works that have also utilized this approach in their applications.

- Chapter 4 is comprised of the development and verification of the algorithm that segments the corneal layers in the eye using AS-OCT imagery of humans and mice.

- Chapter 5 includes the development and validation of the algorithm used to montage and segment IVCM imagery of the corneal sub-basal nerve plexus.

- Chapter 6 explains the utilization of segmentation results from previous chapters to acquire structural measurements of the cornea and how they correlate with ophthalmic diseases.

- Chapter 7 concludes the remarks undertaken in this thesis in addition to any possible future works.

CHAPTER 2
CLINICAL BACKGROUND

In this chapter, a description of the anatomical layers in the cornea followed by background information of ophthalmic diseases as they pertain to corneal structures exhibited in the imagery from our work will be provided.

2.1 Corneal Structures

The cornea is a pellucid structure that is located at the front of the eye covering the iris, pupil, and anterior chamber. Along with the lens and anterior chamber, the cornea accounts for two-thirds of the optical power within the eye [32]. The structural anatomy of the cornea consists of three cellular layers between two basement membranes. From anterior to posterior the cornea consists of the epithelium, Bowman's layer, stroma, Descemet's membrane, and endothelium [32–34]. The structure of the human cornea and its respective layers can be seen in Fig. 2.1.

Due to the similarities between mice and human corneas, mice have become instrumental in the investigation of human ocular processes. Mice have allowed for an increase in understanding of the mechanisms driving corneal development as mice exhibit phenotypes that resemble human ocular diseases. As such, the use of murine imagery is included in our works. The structure of the mice cornea and its layers can be seen in Fig. 2.2.

2.1.1 Epithelium

The epithelium is the umbrella term given to one of the four basic types of tissue in animals (the others being connective tissue, muscle tissue, and nervous tissue). Specifically, corneal epithelium makes up the front of the cornea acting as a barrier of protection by resisting the free flow of fluids inherent in tears. It also helps to prevent foreign objects and bacteria from entering the cornea [32, 33].

The epithelium includes multiple layers of cells with basal cells in the deeper layer
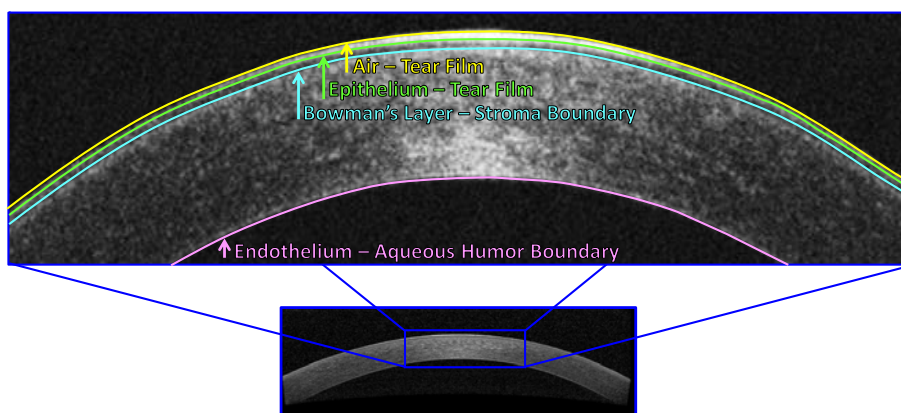
(a)

Figure 2.1: A 2D slice from an OCT volume of a human cornea and its respective layers.
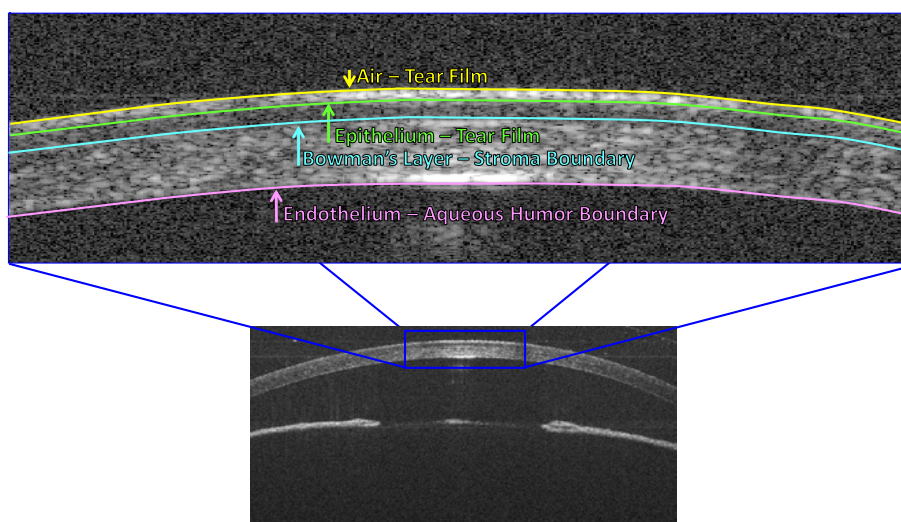
(a)

Figure 2.2: A 2D slice from an OCT volume of a mice cornea and its respective layers.
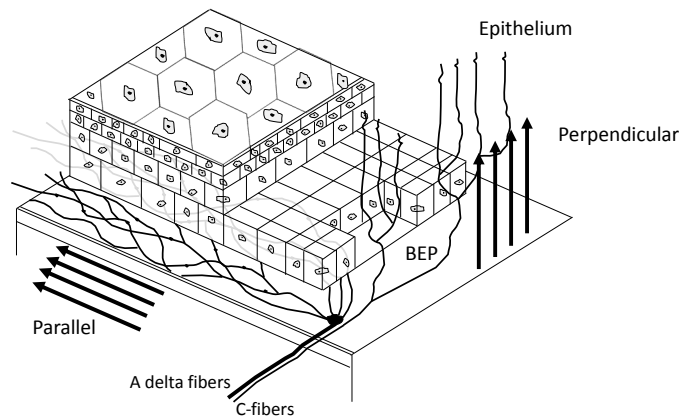
Figure 2.3: A cross-sectional view of the corneal nerves as they branch out perpendicular and parallel to the epithelium layer. The nerves we segment are the ones perpendicular to the epithelial layer. Image inspired by illustrations in [37]

down near the stroma followed by two to three layers of wing cells, and three or four layers of squamous cells closer to the tear film and outer part of the eye [32].

2.1.2   Bowman's Layer

The Bowman's membrane is a smooth nonregenerative layer right above the base of the stroma and below the epithelium [33]. It's composed of fibrils of collagen wherein the anterior smooth surfaces face the epithelial basement membrane and the posterior surfaces meet with the lamellae of the stroma [33]. The current functions of Bowman's layer are still unclear but recent postulations have stated that the layer exhibits itself as a physical barrier to protect the subepithelial nerve plexus [35, 36].

The IVCM imagery that contains the corneal nerve fibers we register and segment in our methodologies are at the sub-basal nerve plexus correspondingly located at the base of the epithelial layer parallel to the epithelium encapsulated by Bowman's layer. The location of the corneal nerve fibers can be seen in Fig. 2.3.

2.1.2.1   Stroma

The stroma is the thickest layer of the cornea in humans representing about 90% of its total thickness and most of the resilience and strength of the cornea. The human stroma is made up of approximately 300 lamellae of parallel collagen fibrils around the middle of the corneal radius and can reach upwards of 500 lamellae as the cornea expands out towards the limbus. The lamellae can differ in orientation with each other but are all parallel to the surface of the cornea. In the center, they are orientated in the inferior-superior and nasal-temporal directions. Outwards near the limbus, these collagen fibrils are oriented in a circumferential manner, providing support and resistance to anything perpendicular to the axis of the fibrils [32, 33].

2.1.3   Descemet's Membrane

While not distinctively viewable as a separate surface via AS-OCT imagery, Descemet's membrane is still a component of the cornea and is designated as a part of the corneal endothelium. Descemet's membrane is a type of basement membrane. Basement membranes are thin, fibrous matrices of tissue that separate the epithelium, mesothelium, or endothelium from connective tissue throughout areas of the body. Descemet's membrane, like other basement membranes, is made up of two different layers 1) the posterior layer adjacent to the endothelium also similarly made up of endothelial cells and 2) an anterior layer consisting of collagen lamellae and proteoglycans like the stroma which it shares with its other boundary [32, 33, 38].

2.1.4   Endothelium

The corneal endothelium is the innermost surface of the cornea represented by a single layer of cells. It is the last surface of the cornea before reaching the anterior chamber of the eye followed by the iris and the posterior chamber. The endothelium is formed by specialized mitochondria cells that lie flat and line the posterior surface of the cornea [32].

The endothelium faces the anterior chamber to allow leakage of nutrients and solutes present in the transparent, gelatinous fluid between the iris and cornea known as the aqueous humor which flows out freely from the ciliary body into the anterior chamber. At the same time, the endothelium pumps water in the opposite direction from the other layers of the cornea, most specifically, the stroma [32, 33].

2.2   Glaucoma

Glaucoma is a group of ocular disorders that lead to progressive damage to the optic nerve. This damage is characterized by a loss of nerve tissue which ultimately results in an incurable loss of vision. Glaucoma affects more than 67 million people around the world and 2.2 million Americans [39]. Currently, glaucoma ranks as one of the highest causes of blindness worldwide and is estimated to affect approximately 80 million people by 2020 [40]. It should come as no surprise that one of the largest hurdles in regards to glaucoma is the diagnosis itself. Approximately 50% of patients are undiagnosed resulting in irreversible damage as the disease progresses to more advanced stages before it has even been detected. In the same vein, an estimated 50% of patients currently being treated for glaucoma do not require medication [41].

The most common type of glaucoma is called open-angle glaucoma, where there is an increase in internal eye pressure from clogging of the eye's drainage canals over time. This causes damage to the optic nerve and eventually leads to blindness in a patient. The problem with open-angle glaucoma is that patients don't often notice the initial loss of peripheral vision and by the time vision loss is noticed, the disease has advanced significantly. Fig. 2.4 shows an example of the peripheral vision loss that stems from open-angle glaucoma.

Glaucoma is currently detected on a patient by applying a comprehensive list of exams that include a visual acuity test, visual field test, dilated eye exam, tonometry, and pachymetry. A significant symptom of most types of glaucoma is an increase in intraocular pressure (IOP), which is determined using tonometry. This is analogous to
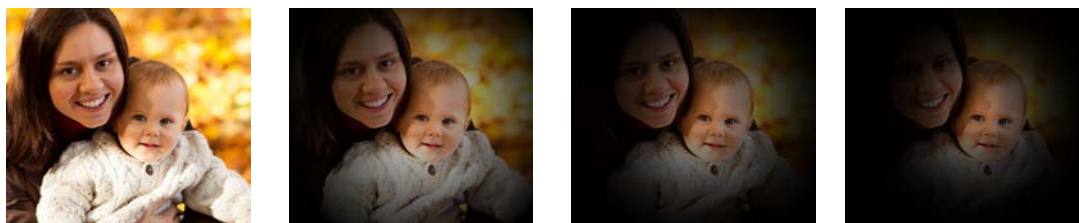
Figure 2.4: An example of the progression of peripheral vision loss stemming from open-angle glaucoma. Public domain image courtesy of [42].

checking the tire pressure of a car by kicking the tire. The problem with determining intraocular pressure using a tonometer is that corneal thickness can mask accurate readings. Again, analogous to tire pressure, a tire that has a thicker or thinner rubber thread can give a false "feeling" of pressure that is higher or lower than a "normal" tire. In essence, thin corneas will show artificially low IOP readings potentially "masking" the ability to recognize truly glaucomatous IOP readings [43]. Similarly, thick corneas will show artificially high IOP readings. Oftentimes this will result in unnecessary treatment, or worse, patients going untreated.

Central corneal thickness and intraocular pressure have become vital parameters on the path to the preventative treatment of glaucoma. In clinical practice, CCT and IOP are used to aid in the diagnosing of glaucoma, determining the progression of the disease, and for evaluating the response of treatments on patients [44]. CCT can be reliably measured via pachymetry but the use of IOP as a measurement hinges upon the reproducibility and reliability of the tools used to take said measurement. Unfortunately, the underlying core assumption behind the tool used for measuring IOP, the Goldman Applanation Tonometer, was that variations in corneal thickness occurred rarely in the absence of a corneal disease. Thus, it was assumed these variations need not be accounted for when measuring IOP [45]. Goldman and Schmidt merely acknowledged that *in theory*, CCT could influence applanation measurements.

It wasn't until two decades later that central corneal thickness would, in fact, be shown to significantly influence applanation measurements [46–48]. Additionally, it's been established that patients who have open-angle glaucoma exhibit a decreased overall central corneal thickness when compared to ethnically-matched and age-matched controls. Humans tend to display an overall mean value of 540 μm but can exhibit statistically vast interethnic differences. The ethnicities that don't differ significantly from the overall mean are Caucasians (550.4 μm), Chinese (555.6 μm), Filipino (550.6 μm) and Hispanics (548.1 μm). Ethnicities that do differ significantly from the overall mean include Japanese (531.7) μm and African Americans (521.0 μm) [49].

While glaucoma cannot be cured, if diagnosed early enough it can be treated and controlled accordingly. This is why studying the effects of glaucoma on the corneal structures is important. It promotes a better understanding of each specific layer in the cornea and its role in the diagnosis and treatment of glaucoma.

2.3 Diabetes

Diabetes mellitus (DM), also known as diabetes, constitutes a group of metabolic diseases where the body experiences high blood sugar levels over prolonged periods of time. It is a widespread disease that affects 9% of the American population making it the leading cause of blindness and the 7th leading cause of death in the United States [9]. It can develop acute complications like diabetic ketoacidosis and nonketotic hyperosmolar coma as well as severe long-term complications like cardiovascular disease, stroke, kidney failure, foot ulcers, and damage to the eyes [50].

It has also been shown that diabetic patients develop reduced corneal sensitivity [10], such that even a small sensitivity level significantly reduces reflex tear secretion [51–53]. In addition, patients are predisposed to corneal trauma and neurotrophic corneal ulcers [54]. Keratopathy, another complication led by diabetes, is a corneal disease that causes build up of calcium on the central cornea. It is treated by scraping

the calcium from the cornea but repeated treatment can make the cornea thinner and thinner eventually damaging the endothelial layer.

One impactful complication of the disease is diabetic neuropathy. Due to the high blood glucose levels from diabetes, nerve fibers can be injured, causing permanent damage to the limbs. It can affect sensory, autonomic, and motor neurons. Recently, studies have shown a correlation between corneal nerve fiber density and the severity of diabetic neuropathy [11].

Oftentimes when patients notice the symptoms of diabetic neuropathy it is an indicator that they've progressed beyond being able to take preventative measures or treatments eventually leading to irreversible damage. This is why it is important to develop early screening methods to better assess the progression of these complications before they get to this point.

2.4 Trigeminal Nerve Lesions

The trigeminal nerve (the fifth central nerve, CN V) is the largest cranial nerve and is in charge of sensation and motor functions of the face [55]. It supplies the muscles required for mastication giving the mandible access to the movements required to do so. In addition, it mediates corneal reflex, described as the bilateral blink response of the eye [56]. Furthermore, the trigeminal nerve resides over the touch-position and pain-temperature sensations of the somatosensory system for the face including the eyes, nasal passages, and oral cavity. [56, 57].

A nerve lesion is classified as an injury to the nerves in the body and can be caused by a variety of situations including physical trauma, degenerative diseases or as a result of surgical procedures. Lesions of the trigeminal nerve can erupt the sensory system of the face. They can affect the muscle functions of the face as well [57, 58]. The most common systems of trigeminal nerve lesions include reduced sensation over the affected area or the weakened ability of the motor functions including clenching or limited lateral movement of the mandible or reduced bilateral blink response when

measuring corneal reflex [59].

There are times when trigeminal nerve lesions are done purposely, like in the case of trigeminal neuralgia, where radiosurgery is used to damage the trigeminal nerves to stop transmission of pain signals to the brain. One consequence of this surgery is neurotrophic keratopathy (NK). Neurotrophic keratopathy is a degenerative disease characterized by poor corneal healing and decreased corneal sensitivity. Correlations have shown to exist between a decrease in corneal nerve fiber density and decreased corneal sensitivity stemming from NK [60, 61].

Current efforts for treating the symptoms of trigeminal nerve lesions exist in surgical form but no specific medical treatment exists as an alternative option. With the resources available through non-invasive imaging of the eye, it becomes imperative that we consider further studies on the correlations between trigeminal nerve lesions and corneal structures in order to provide such options.

CHAPTER 3
TECHNICAL BACKGROUND

In this section, contributions that have been made to the area of segmenting ophthalmic structures via OCT imaging modalities and to the area of image stitching for microscopy imagery will be described.

The groundwork for many of these contributions also includes a graph-theoretic approach [62] which has seen use in segmenting retinal and corneal layers. Due to its extensive use in these fields, specifically in our work of segmenting the corneal layers (Ch. 4), the graph-theoretic approach will also be explained more thoroughly.

3.1   Previous Work

3.1.1   Segmenting the Corneal Layers

Originally starting with time domain-OCT (TD-OCT) and then later on with the development of spectral domain-OCT (SD-OCT) (or Fourier domain-OCT, FD-OCT) [63–65] the imaging world was introduced to a new method of imaging ophthalmic structures allowing for the acquisition of volumes that covered an exceptional amount of physical structure in a reasonable amount of time. The principle of OCT relies on indirect interferometry. The intensity of each voxel in an OCT image is made by beaming a light into the biological tissue and comparing the backscatter, which travels an unknown distance, with a reference light beam whose length is known in order to calculate the echo time of delay. With the introduction of SD-OCT, image acquisition is slightly varied in that the interference is acquired with detectors separated in the spectral domain such that the depth scan is immediately calculated by a Fourier-transform without having to move the reference arm. The depth scan is calculated based on the principle of the Wiener-Khintchine theorem which states that an autocorrelation function of a wide-sense-stationary random process has a spectral decomposition given by the power spectrum of that process [66, 67]. One example of spectral domain-optical coherence tomographers includes the Zeiss Cirrus OCT (Carl

Zeiss Meditec, Dublin, CA) allowing for imaging of an ONH volume with a resolution of $200 \times 200 \times 1024$ voxels, expanding over $6 \times 6 \times 2$ mm^3 of the retina in the physical domain taking about two seconds for the volume. With these methods for reliable imaging becoming more readily available the ability to measure corneal and retinal properties using ophthalmic image analysis techniques was soon to follow. While SD-OCT paved the way for measurement of ophthalmic properties there are still inherent problems with this imaging modality [68]. One issue includes the presence of speckle noise, an intrinsic property of coherence imaging. This can cause a fuzzier border between boundaries making it difficult to find the optimal segmentation between layers. Similarly, while signal penetration continues to improve with the introduction of higher wavelengths in SD-OCT scanners, signal attenuation still poses a problem. Due to the very nature of coherent imaging, the light source will have a tougher time penetrating deeper structures which in turns causes their respective voxels to have a lower intensity. Another inherent property of ophthalmic imaging is the intrinsic movement of the eye. With the introduction of Fourier domain technology OCT devices have the ability to make upwards of 50,000 A-scans/second in the spectral domain but despite these fast scan speeds a saccade of the eye to unexpected stimuli can still move at an angular speed of 900°/sec. Typically a saccade will last 20-200 ms resulting in a successive shift in B-scans.

While the basis for some works in the field of corneal layer segmentation sprout from initial work on intraretinal segmentation [62,69,70] only an additional few methods to segment the corneal layers have been developed. A graph-theoretic approach is the most common [14,15,17] while other methods include a variation on the Hough Transform [13], active contours [12], or Gaussian Mixture Models [16] to segment the corneal layers.

Of all the works currently introduced to segment the corneal layers some are semi-automated [19,20] and some are fully automated [12–17,71]. Additionally, many of

the fully automated methods [12–14,16,17,71] are limited in their scope as they work strictly in 2D, segment only a few of the layers, and/or segment each of the layers individually. To the best of our knowledge only the foundations of our methodologies published in [15] and our work discussed in Ch. 4 have accomplished segmentation of all the layers simultaneously in 3D.

More specifically, of the fully automated approaches, Graglia et al. [12] only segment the top and bottom layers on a single slice using a contour detection approach. Similarly, Li et al. [71] use Fast Active Contours to segment all surfaces. Both of these methods rely on choosing the correct initial points for the contour and any deviation can produce incorrect results. Additionally, their scope is limited to iterative single-surface segmentation on a 2D slice.

The method proposed by Eichel et al. [13] uses a Hough transform and peak detection to automatically segment the corneal surfaces. The method uses a sample of images that have already been manually segmented in order to learn an initial quadratic curve shape model. Next, they optimize the curve based on Prewitt edge detection results of the top and bottom layers. This, in turn, creates a parameterization of the cornea model allowing for their Hough transform to find the remaining layers. The limit to this technique lies in its need for manually segmented images *a priori* and additionally, it only segments the volume slice-by-slice in 2D and each surface individually.

La Rocca et al. [14] proposed a dynamic programming technique for segmenting multiple corneal layers in AS-OCT images. After considerable preprocessing steps, their algorithm uses Dijkstra's method on a gradient image to segment a single surface starting with the air-tear film boundary. Then a flattening of the image slice based on these prior air-tear film boundary results is produced. Additionally, an estimation of the total thickness is needed to limit the region for finding the next surface. An assumption is made such that the thickness of the cornea at the apex approximates

the minimum thickness of the cornea. By searching for the largest decrease in mean intensity of adjacent rows within the assumed range (400 to 800 μm) below the air-tear film interface a limited region is developed to find the next surface. This same method is followed to find the third surface. The main limits of this approach are its assumptions on where noise occurs for its preprocessing steps, that it segments each surface individually only in 2D, and that it was evaluated on a small data set. Jahromi et al. [16] developed a technique based on the Gaussian Mixture Model (GMM). They applied a GMM to localize the epithelium and endothelium boundaries then applied a gradient response of a contrast enhanced version of the image into another GMM algorithm to get a better result around the Bowman's layer. Finally, the first layer is traced down to localize the true location of the Bowman's layer for their final results. However, their data set is very limited having only used 10 patients with 40 slices for each volume. Additionally, the surfaces are found individually and only in 2D.

Williams et al. [17] used a graph cut approach that takes regional and shape terms into consideration. Their preprocessing includes removing the iris and central noise from the full corneal slice followed by a quick threshold segmentation using an entropy filter to create a feasible ellipsoid region around the cornea for the graph cut algorithm to segment. The graph-cut algorithm used was constructed with a regional statistics term, a curvature term, and a shape term and used the Dynamic Boykov-Kolmogorov algorithm to find the optimal graph-cut solution to the segmentation problem. While fast and accurate, this method is also limited to 2D with individual surfaces found sequentially.

While OCT has revolutionized medical imaging many of the advantages it brings to anterior-segment imaging have not been utilized to their maximum potential. Firstly, many of the previous works segment layers sequentially without any utilization of the intersurface and intrasurface interactions. Furthermore, all these works, minus our own method, have not utilized the 3D information which can be vital to

providing more in-depth information of the structures in question. An implementation that uses all the 3D information of the OCT volume and can segment all the layers simultaneously is needed in utilizing all the advantages of OCT corneal imaging.

3.1.2 Image Stitching of Corneal Confocal Microscopy Images

Oftentimes, a specimen cannot be captured in a single microscopic image because at such a low optical magnification a significant portion of resolution will be lost. The trade-off then becomes image size versus resolution. A straightforward solution is achieved by taking a higher number of images around the same area at a higher optical magnification. The images can then be stitched together manually to provide a larger field of view. Given many data sets, and many images within a data set, manual alignment quickly prevents itself from still being a viable option. Thus, an automated approach must be developed in order to make use of the data efficiently. This is not to say that manual options are out of the question. In fact, for works in our field that involve confocal microscopy images of the human corneal sub-basal nerve plexus, Patel et al. [28] were the first to apply manual registration in order to elucidate the overall distribution of sub-basal nerves in the human cornea. However, it became obvious that with data sets that can reach upwards of 300 images per set, automated solutions were in need.

In his review of image alignment and stitching applications from a technical perspective, Szeliski [72] proposed the overall essential problem set of image alignment. The first step in solving the image stitching problem is to determine the appropriate mathematical *motion model* that relates the pixel coordinates between images in the set. In addition, an estimation of the correct alignments that relate pairs (or sets) of images must be considered via *direct* pixel-to-pixel comparison, or similarly, by finding distinctive *features* that establish a correspondence between pairs (or sets) of images. Consider further the fact that when multiple images exist, as in the case

of stitching or panoramas, a globally consistent set of alignments that matches the overall set of images must be developed to efficiently discover the correspondence between the sets of images. While this set of alignments can be found in a variety of ways, a final *compositing surface* must also be established in order to seamlessly blend the images together.

One of the most significant works in the field of feature-based image stitching is David Lowe's research on a scale-invariant feature transform (SIFT) which was first developed in 1999 [73] and shown to perform well in the applications of panoramic image stitching [74] and object recognition [75]. Lowe proposed a method for extracting invariant features between images to perform matching of an object or scene. The method proved to be reliable and robust in matching across various images that included affine distortion, a change in the viewpoint (3D), and any additions of noise or change in illumination. Single features proved to be very distinctive allowing for a feature to be highly recognizable among many different images. In addition to object recognition, the method was used in the creation of panoramic images due to its innate ability to deal with rotation, zoom, and illumination changes across a set of images.

Not long after, Dalal et al. [76] introduced another feature-based method for object detection, specifically for human detection in images, called the Histogram of Oriented Gradient (HoG) descriptors. Essentially, the method assumes that the appearance and shape of a local object can be described by its intensity gradient distributions and directions. Thus the image is subdivided into cells wherein HoGs are compiled for the pixels in each cell. The HoG descriptor is then described as the concatenation of all these histograms. This makes the descriptor resistant to translation or rotation so long as these geometric transforms are smaller than the local spatial/orientation bin size used to find the HoG descriptors. Similarly, the localized histograms are contrast-normalized to ensure invariance to illumination and shadowing. This is achieved by

measuring the intensity around a larger region, called a block, then using that result to normalize all the cells within that block. Since HoG has been used originally for detection of humans in scenes it was found that coarse spatial sampling, fine orientation sampling, and strong local photometric normalization worked the best for this purpose.

The most notable problems found in automatically registering microscopic images include variable background noise, the similarity of patterns in microscopic images, inter/intra image illumination differences, the low overlap between images, and the involuntary motion of objects found in microscopic images. Whereas in recreational panoramic stitching these problems are not as delimiting, they can pose a problem for microscopic image stitching. Nonetheless, with the great success of SIFT for automatic panoramic stitching, Fan et al. [29] proposed using it for microscopic images as well. Coupled with Best-Bin-First (BBF) and Random Sample Consensus (RANSAC), they managed to achieve good results though the data sets contained very few images, only around 8-10 images per set. Although they also showed registration on an image set wherein all the images have similar patterns, the shapes of most of the objects in the microscopic images were still distinctively different such that the SIFT features could also be distinctive enough between image pairs. For the corneal nerve fibers imagery registered in our works, many nerves have very similar structures such that the SIFT features were not distinctive enough between them as to be able to match the correct structures within image pairs resulting in unrealistic registrations or outright failure to register the images.

As noted earlier, a montage can include several hundred images making manual arrangements highly labor intensive not to mention the expertise required to ascertain a correct model. To the best of our knowledge, the only other methods developed for fully automated montaging of laser scanning IVCM images of the human corneal sub-basal nerve plexus are the works from Zhivov [77], Pritchard [78], Turuwhenua [30],

Poletti [79], and Allgeier [80].

Zhivov et al. and Allgeier et al. [77, 80] are the only known works to incorporate real-time online registration and/or modified hardware. An important element to consider here is their accessibility and modification of the imaging machine. Zhivov et al. incorporate the ART composite mode of the imaging device but this proved to require expert personnel and multiple attempts at the compositing in order to yield larger montages. Allgeier et al. use a small monitor up near the contralateral eye to provide a tracking object for the patient. Allgeier et al. also requested software modifications from the manufacturer allowing direct streaming to a hard disc file bypassing the 100 image limit of the Sequence Scan operating mode. These are components that would not be readily available for users not familiar with the hardware/software integrations of the confocal imaging device. Similar to the works of Allgeier et al., Pritchard et al. [78] also use an after-market display with a video of a moving object wherein patients were asked to track the object with their contralateral eye. Their montaging was also a semi-automatic process using commercial software.

Turuwhenua's offline method [30] starts by accepting or rejecting images, most notably, any images that contain epithelium cells as these can be found to transcend into the nerve plexus layer. The method continues by clustering the images using gross nerve direction detected using a Hough transform to find lines in an image and also based on the natural ordering of the images. Keypoint generators are then created on the binary images and random consensus sampling (RANSAC) is used to determine true matches robustly with a breadth-first walk used to cluster the final montage together. The works of Turuwhenua et al. provide adequate results but can take a few hours for a set of results on a single image set. The algorithm also makes an assumption of acquisition order and gross nerve orientation. These can become an issue if the acquisition order does not necessarily correspond to subsequent imagery overlapping. Additionally, nerve migration and orientation can cause imagery from

opposite ends of the corneal whorl to appear to have the same orientation leading to incorrect registration. The method also lacks a blending operation to seamlessly blend all the images together for further image processing and is quite unclear on the keypoints used to generate the feature set.

Poletti et al. [79] developed an offline algorithm that uses a common image registration technique of using phase correlation to determine which images should be registered. A high phase correlation indicates larger overlap between images while low phase correlation indicates little to no overlap exists between images. A score matrix is then developed from the phase correlation values between all images in a set. Because of the inability of the focal plane to stay constant in the same region of the cornea, that is to say, the z-depth can vary even if the region stays the same, Poletti also proposed filtering out redundant images of the same region by only keeping the image with the most nerves. This was determined by looking at the likelihood of an elongated structure in the image. The score matrix containing the phase correlations was then used to determine the order in which to register all the remaining images. To blend the montage, a weighting function was used that combines the intensity value of the pixel from each of the respective images versus the location of that image relative to the overlap in the montage. While the phase correlation method proposed by Poletti would be fast and efficient, it fails to provide adequate results for the imagery acquired by our photographers at the University of Iowa. The reason being that Poletti et al. included data sets where all the images in the data set had significantly large overlaps. Unfortunately, this is may not be feasible given the time constraints of the patients and photographers acquiring the imagery for the medical applications like those in our works.

Thus, the current works developed for registering corneal nerve fiber layers either rely on *a priori* knowledge of the imagery acquisition, on after-market hardware modifications, or on commercial software not readily available to the everyday user. Our

work is developed for imagery that is often obtained under typical clinical settings; the most notable being the typical time commitment of patients that still allows us to acquire meaningful data sets without any after-market hardware or software modifications. Some previous works are also missing components to further analyze the structure of corneal nerves to produce quantitative measurements necessary for further analysis. This is why the framework in our work also establishes a way to seamlessly blend the imagery in order to apply further analysis on the results (i.e. segmentation for quantitative analysis on the corneal structures).

3.1.3   Segmenting the Corneal Nerves

Previous works have proven to be effective in automatically recognizing the corneal nerve structures present in confocal microscopy images of the sub-basal nerve plexus. As such, in our works, we incorporated these techniques to segment the corneal nerves in single and montage imagery of the sub-basal nerve plexus. Scarpa et al. [21] were the first to succeed in finding corneal nerve fibers by detecting seed points used as starting points for a nerve tracing algorithm. The algorithm proceeds by detecting nerve direction and a fuzzy c-mean clustering technique to determine the next pixel that is most likely to be a nerve based on the cluster profiles. In a similar vein, Guimaraes et al. [25] also implemented a seed point technique coupled with a graph-based algorithm to segment the corneal nerves with great success. Dabbah et al. [22] incorporated a combination of image enhancement techniques from the results of 2D Gabor filters, Line Operator (developed for detection of asbestos fibers), Frangi vesselness features, and the Dual-Tree Complex Wavelet Transform combined to create a feature set trained on neural-network and random-forest classifiers to present a final segmentation of the nerves. Many previous works have also included log-Gabor filters as features for their segmentation analysis, be it as part of a morphological segmentation algorithm [23] or as features for their machine learning algorithm [31, 81]. Guimaraes et al., who originally used seed points coupled with a graph-based algo-

rithm in 2014 [25] also changed course and implemented machine learning techniques that included log-Gabor filters as features after its prominent success in the present literature. It proved to be vital to their more present work [31] in segmenting montage imagery. As it stands, Al-Fahdawi et al. [81] and Guimaraes et al [31] show the most current state-of-the-art in corneal nerve segmentation algorithms. They explore the optimal morphological operators, filters, machine learning algorithms, and quantification techniques shown to most effectively segment the corneal nerves. Therefore, their techniques are the standards of our works in single-image and montage image segmentation.

3.2 Graph-Theoretic Approach

The graph-theoretic approach is a technique that has been used extensively for the segmenting of multiple surfaces simultaneously. It was first introduced by Li et al. [62] to segment airway wall borders, airway segments, the diaphragm for in vivo CT images, and MR arterial walls. Since its introduction, it has been used in other segmentation applications including those in this work. At its core, the graph-theoretic approach takes the segmentation problem and transforms it into an optimization problem where the goal is to find a minimum-cost closed set. The minimum-cost closed set problem is then transformed into a minimum cut/maximum flow problem where the globally optimal solution with respect to the cost function is found using a minimum s–t cut. One key component to this approach is the feasibility constraints which govern the intrasurface smoothness and intersurface interactions. The other key component being the cost functions which are used to find the globally optimal solution.

3.2.1 Feasibility Constraints

Let us consider a volumetric image defined as $\mathcal{I}(x, y, z)$ with respective dimensions of $X \times Y \times Z$, and a surface $\mathcal{S}_i$ defined as a function $\mathcal{S}_i(x, y)$. This function would

in turn map (x, y) pairs to their respective z–values wherein $x \in \{0, 1, \cdots, X - 1\}$, $y \in \{0, 1, \cdots, Y - 1\}$, and $z \in \{0, 1, \cdots, Z - 1\}$. As such the surface $\mathcal{S}_i$ would only intersect one voxel in each column parallel to the z–axis as it spans the entire $x \times y$ domain. Such is the case for a B-scan in our AS-OCT volumes. From the outset [62,82], the smoothness constraints represent the maximum change in z allowed in the x–direction denoted as Δ_x and in the y–direction denoted as Δ_y. In other words, if $\mathcal{I}(x, y, z_1)$ and $\mathcal{I}(x + 1, y, z_2)$ are two adjacent voxels on a surface in the x–direction then $|z_1 - z_2| \leq \Delta_x$. Additionally, given two adjacent voxels on a surface in the y–direction $\mathcal{I}(x, y, z_1)$ and $\mathcal{I}(x, y + 1, z_2)$ we have $|z_1 - z_2| \leq \Delta_y$. It was later proposed by Garvin et al. [83, 84] to introduce a dynamic constraint in which the smoothness constraints varied with respect to the location (x, y) of voxels represented by the surfaces. Varying smoothness constraints as we go from (x_1, y_1) to (x_2, y_2) can be written as follows:

$$-\Delta^u_{\{(x_1,y_1),(x_2,y_2)\}} \leq \mathcal{S}(x_1, y_1) - \mathcal{S}(x_2, y_2) \leq \Delta^l_{\{(x_1,y_1),(x_2,y_2)\}}, \qquad (3.1)$$

where, $\Delta^u_{\{(x_1,y_1),(x_2,y_2)\}}$ and $\Delta^l_{\{(x_1,y_1),(x_2,y_2)\}}$ are the maximum upper and lower permitted changes in the z–direction, respectively.

The other feasibility constraint enforces the interactions between surfaces giving the minimum distance $\delta^l_{i,j}$ and the maximum distance $\delta^u_{i,j}$ between surface $\mathcal{S}_i$ and surface $\mathcal{S}_j$. Moreover, it provides an order to the surfaces, specifically which surfaces lie above or below the other ones. In its original form as proposed by [62] surface-interaction constraints were considered to have constant values for all pairs of adjacent surfaces but can also be defined as varying based on location (x, y) [83,84]. For surface $\mathcal{S}_i$ above a surface $\mathcal{S}_j$ it is written as follows:

$$\delta^l_{i,j}(x, y) \leq \mathcal{S}_i(x, y) - \mathcal{S}_j(x, y) \leq \delta^u_{i,j}(x, y), \qquad (3.2)$$
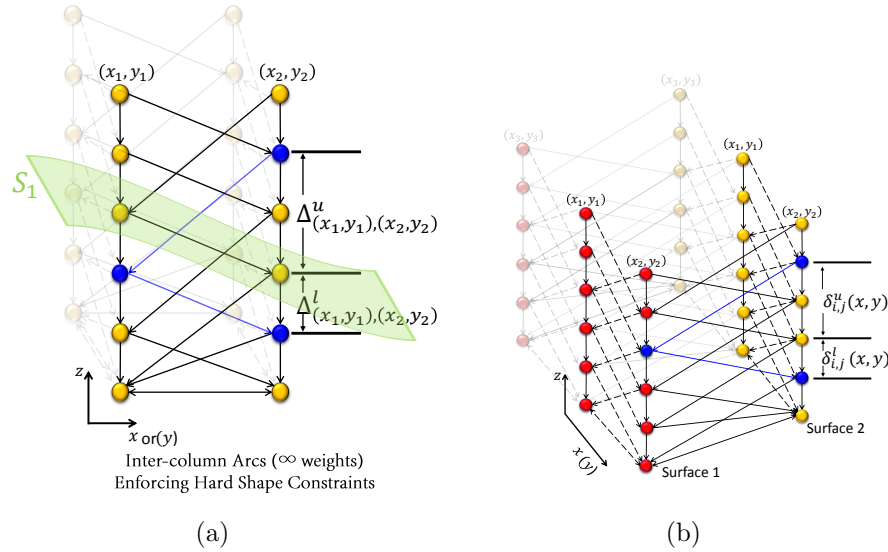
Figure 3.1: (a) Intra-surface smoothness constraints Δ^u and Δ^l. (b) Inter-surface interaction constraints δ^u and δ^l used in the s-t cut (figures adapted from [85]).

Fig. 3.1 illustrates the varying inter-surface and intra-surface interaction constraints explained above.

Of more critical importance to our work is the feasibility constraints proposed by Song et al. [86] who developed a method which further incorporates the shape prior information in the surface smoothness constraints. In its original form [62], surfaces were to be either feasible or non-feasible. This method did not grant the penalties to any deviation. This lead to unideal results where the boundaries appeared jagged or rough. Instead, Song et al. proposed additional soft constraints based on some given shape prior. This method allows for a convex function $f(h)$ that penalizes the cost of the surface set if the change of the surface deviates from the expected, mean shape. Given the shape prior between two adjacent columns (x_1, y_1) and (x_2, y_2) on the surface $\mathcal{S}_i(x, y)$ as $m_{(x_1, y_1), (x_2, y_2)}$ then the cost of the shape term is expressed as:

$$C_{Sp_i} = \sum_{\{(x_1,y_1),(x_2,y_2)\in\mathcal{N}_c\}} f(\mathcal{S}_i(x_1,y_1) - \mathcal{S}_i(x_2,y_2) - m_{(x_1,y_1),(x_2,y_2)}) \qquad (3.3)$$

where $\mathcal{N}_c$ is given as a set of neighboring columns. This method provides a suitable solution to the jagged surface problem. In order to incorporate soft smoothness constraints, the constructed graph must include additional arcs implemented in the minimum-cost s-t cut. Let us look at a typical creation of the arcs and for the sake of simplicity consider only arcs in the x-direction. This provides us with a simpler model without loss of generality. For a feasible surface $\mathcal{S}(x)$ consider that the smoothness constraint in the x-direction is Δ_x and that the mean shape prior $m_{(x_1,x_2)}$ for two adjacent columns x_1 and x_2 is known. Shape penalties are then considered when $\mathcal{S}(x_1) - \mathcal{S}(x_2) \neq m_{(x_1,x_2)}$. If we denote $h = \mathcal{S}(x_1) - \mathcal{S}(x_2) - m_{(x_1,x_2)}$ then we can express the shape prior penalty as $f(h)$. Then the first derivative and second derivative (discrete) of the convex function is given as $[f(h)]' = f(h+1) - f(h)$ and $[f(h)]'' = [f(h+1) - f(h)] - [f(h) - f(h-1)]$ respectively. The feasibility constraints are given as $-\Delta_x < h < \Delta_x$ and for each h that satisfies $[f(h)]' \geq 0$ we add an arc with a weight of $[f(h)]''$ from $node(x_1, z)$ to $node(x_2, z - m_{(x_1,x_2)} - h)$. In a similar fashion, for a feasible h where $[f(h)]' < 0$ an arc is added from $node(x_2, z)$ to $node(x_1, z + m_{(x_1,x_2)} + h)$ with a weight of $[f(h)]''$.

Fig. 3.2 illustrates the original hard shape constraints alongside the additional arc distribution added by incorporating shape prior information.

3.2.2   Cost Function Computations

In the graph-theoretic approach, the globally optimal solution for a set of feasible surfaces is computed with respect to the cost functions. Edge-based cost functions reflect the unlikelihood of a voxel location on a specific surface. For a surface $\mathcal{S}_i(x,y)$, the edge-based cost function can be expressed as $C_{\mathcal{S}_i(x,y)} = \sum_{\{(x,y,z)|z=\mathcal{S}_i(x,y)\}} \mathcal{I}_{c_{\mathcal{S}_i}}(x,y,z)$. In its original form and the form considered in our methods, the cost function is
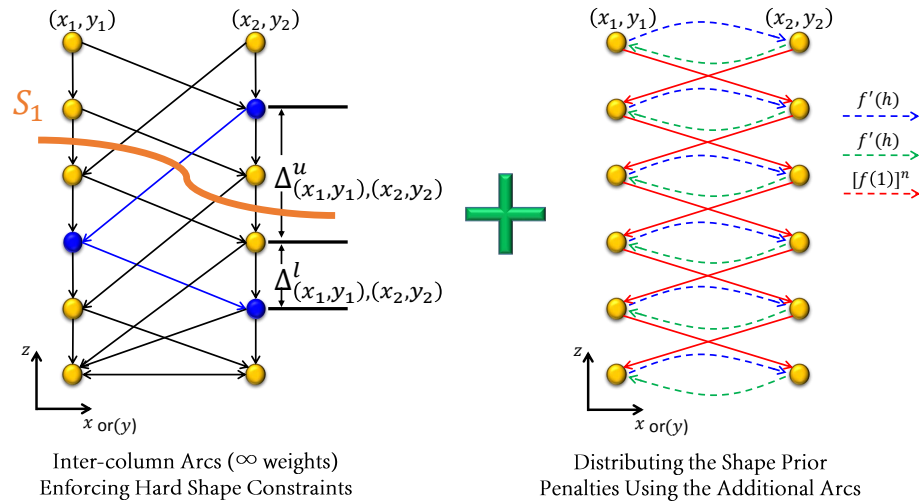
Figure 3.2: An example of intra-surface smoothness constraints Δ^u and Δ^l along with the incorporation of shape prior information as additional arcs in the *s-t cut* problem (figures adapted from [85]).

derived from using directed gradients of the images. These are called edge-based or *on-surface* cost functions because they consider only the cost derived from the gradient images along the edges between surfaces. Fig. 3.3 illustrates what these functions look like for a 2D slice of our images.

In 2007 Haeker/Garvin et al. [83,84] proposed adding additional region-based costs that took into account the region between surfaces. The region-based cost function, appropriately named as *in-region* cost function represents the unlikeliness that a voxel belongs to a specific region. Let us consider a region $\mathcal{R}_i$, we describe the in-region cost as $C_{\mathcal{R}_i} = \sum\limits_{(x,y,z) \in \mathcal{R}_i} \mathcal{I}_{c_{\mathcal{R}_i}}(x, y, z)$. With n non-intersecting surfaces the volume will be divided into $n+1$ regions. Therefore the total cost C_T of n surfaces can be written as
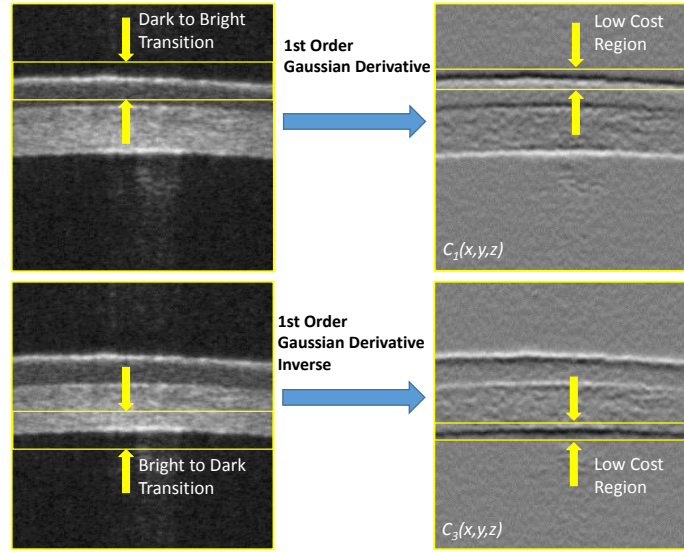
Figure 3.3: Image of the k'th 2D slice with its respective cost function for the top (i) and bottom (j) surfaces expressed as $C_{\mathcal{S}_{i,j}(x,k)} = \sum\limits_{\{(x,k,z)|z=\mathcal{S}_{i,j}(x,k)\}} \mathcal{I}_{c_{\mathcal{S}_{i,j}}}(x,k,z)$.

$$C_T = C_{\{\mathcal{S}_1(x,y),\dots,\mathcal{S}_n(x,y)\}} + C_{\{\mathcal{R}_0,\dots,\mathcal{R}_n\}}$$
$$= \sum_{i=1}^{n} C_{\mathcal{S}_i(x,y)} + \sum_{i=0}^{n} C_{\mathcal{R}_i} \tag{3.4}$$

If we consider edge-based costs $C_{\{\mathcal{S}_1(x,y),\dots,\mathcal{S}_n(x,y)\}}$, region-based costs $C_{\{\mathcal{R}_0,\dots,\mathcal{R}_n\}}$, and deviation penalties induced by the soft smoothness constraints $C_{\{\mathcal{S}_{S_{p_1}},\dots,\mathcal{S}_{S_{p_n}}\}}$ then the total cost induced by the cost functions is defined as C_{Total}. Therefore, the total cost C_{Total} can be computed as

$$C_{Total} = C_{\{\mathcal{S}_1(x,y),\dots,\mathcal{S}_n(x,y)\}} + C_{\{\mathcal{R}_0,\dots,\mathcal{R}_n\}} + C_{\{\mathcal{S}_{S_{p_1}},\dots,\mathcal{S}_{S_{p_n}}\}}$$
$$= \sum_{i=1}^{n} C_{\mathcal{S}_i(x,y)} + \sum_{i=0}^{n} C_{\mathcal{R}_i} + \sum_{i=1}^{n} C_{\mathcal{S}_{s_{p_i}}}. \tag{3.5}$$

CHAPTER 4
CORNEAL LAYER SEGMENTATION FROM AS-OCT IMAGERY OF HUMAN AND MICE USING A GRAPH-BASED APPROACH

The preliminary version of these works has been published in [15].

As the second leading cause of blindness in the US, glaucoma has introduced many clinical standards to help evaluate the changes in ophthalmic structures affected by the disease. With recent correlations between central corneal thickness and glaucoma, one such standard has included measuring CCT using a pachymeter to determine how at-risk a patient is of developing glaucoma [8]. Additional measurements consider intraocular pressure (IOP) and while these conclusions show possible evidence of this risk it has also been hypothesized that an artifact of IOP might be the reason leading to these conclusions. Attempts to correct the tonometer readings for CCT have all failed to eliminate CCT as a predictive factor from the Ocular Hypertension Treatment Study (OHTS) [87]. On that note, we should consider the use of AS-OCT imagery as a way to measure CCT to be able to support the correlation claims that thin CCT determines how at-risk a person is of developing glaucoma as another means of measuring CCT but also to extend its application to measuring other regional thicknesses of the cornea as well. We would also be well to consider that such correlations could also exist between this and similar structural measurements with respect to other diseases known to affect the cornea. Unfortunately, as it stands, most measurements derived from AS-OCT imagery have to be manually obtained making the acquisition of structural measurements difficult.

While manual measurements can be time-consuming, the noninvasive nature of AS-OCT images combined with algorithms that segment the corneal layers can provide an alternative automated approach for acquiring these measurements. Many efforts noted in Ch. 3 include a variety of approaches most of which do not take advantage of the 3D nature of AS-OCT images. Nor do these algorithms use the relation between surfaces to segment all the layers simultaneously.

Correspondingly, the mass effort for the work in this chapter is on developing an algorithm that utilizes the inter and intra surface relations in a 3D AS-OCT image of the cornea while addressing the challenges of such a highly curved structure to automatically segment all the respective surfaces simultaneously. The purpose of this aim is to develop a method for segmenting cornea layers in murine and human data to extract structural information from the corneal layers for further analysis.

4.1   Methods

Given the fact that mice have very similar ophthalmic structures to humans, it is no surprise that mice are frequently used to study the causes and progression of ophthalmic diseases. In addition, with the impact that diseases like glaucoma and diabetes have on society, it is imperative that the segmentation algorithm also be considered for ophthalmic structures in humans. The goal of this work is to develop a fully automated graph-theoretic approach that can take advantage of the shape prior information of the cornea to segment the air-tear film boundary, epithelium-tear film boundary, Bowman's layer-stroma boundary, and the endothelium-aqueous humor boundary in AS-OCT images of mice and humans. An overview of the method is shown in Fig. 4.1 with results of each step in the methodology shown in Fig. 4.2 for the murine data set and in Fig. 4.3 for the human data set. Note that while the acquisition of the murine and human images are similar, the properties of the images vary slightly due to the difference in the tomographers and physical dimensions of the structures. As such the preprocessing steps also vary slightly as can be seen in Fig. 4.1.

The method is described in several steps presented below as follows:

4.1.1 Course Outer Layer Segmentation

4.1.2 Polynomial Fit to Outer Layers

4.1.3 Image Flattening and Simultaneous Segmentation

4.1.4 Polynomial Fit for Final Segmentation
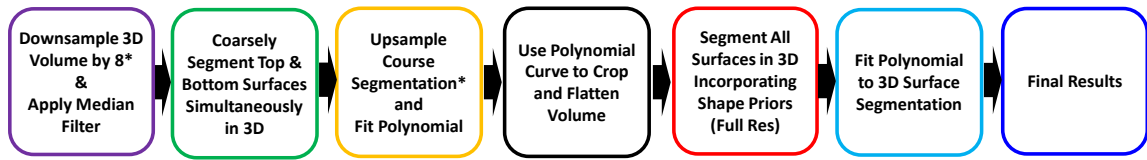
Figure 4.1: Overview of the methodology in Aim 1 to segment the corneal layers in AS-OCT images of murine and human data.
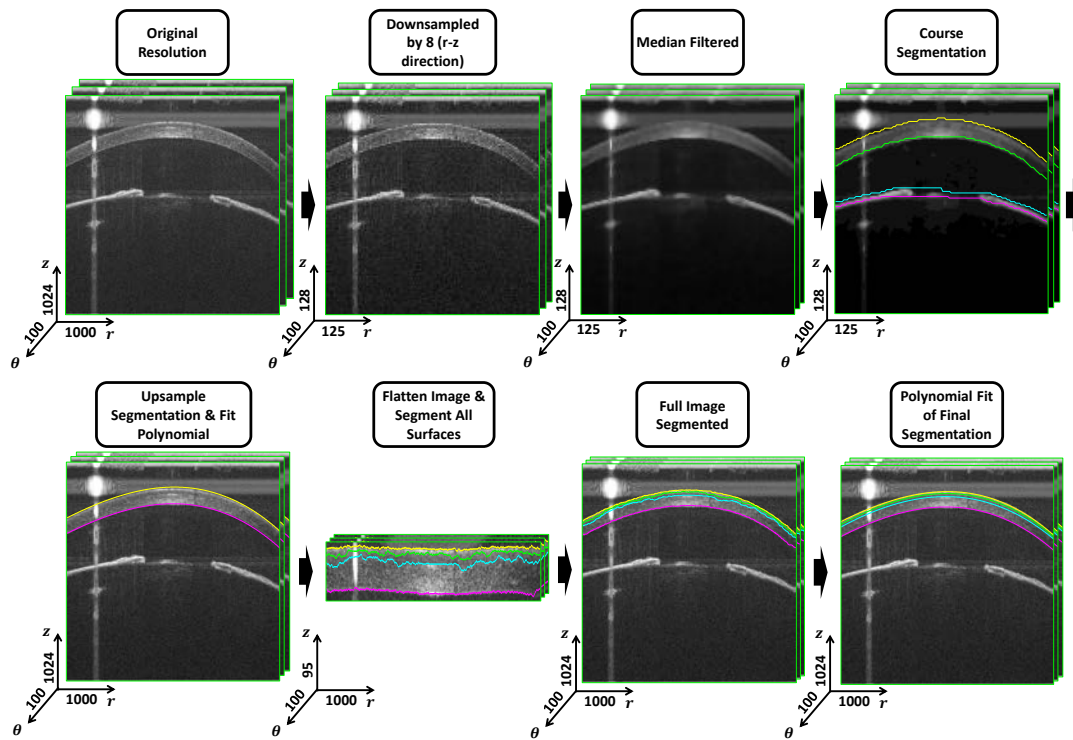
Figure 4.2: Results of the method in Aim 1 for murine corneas.
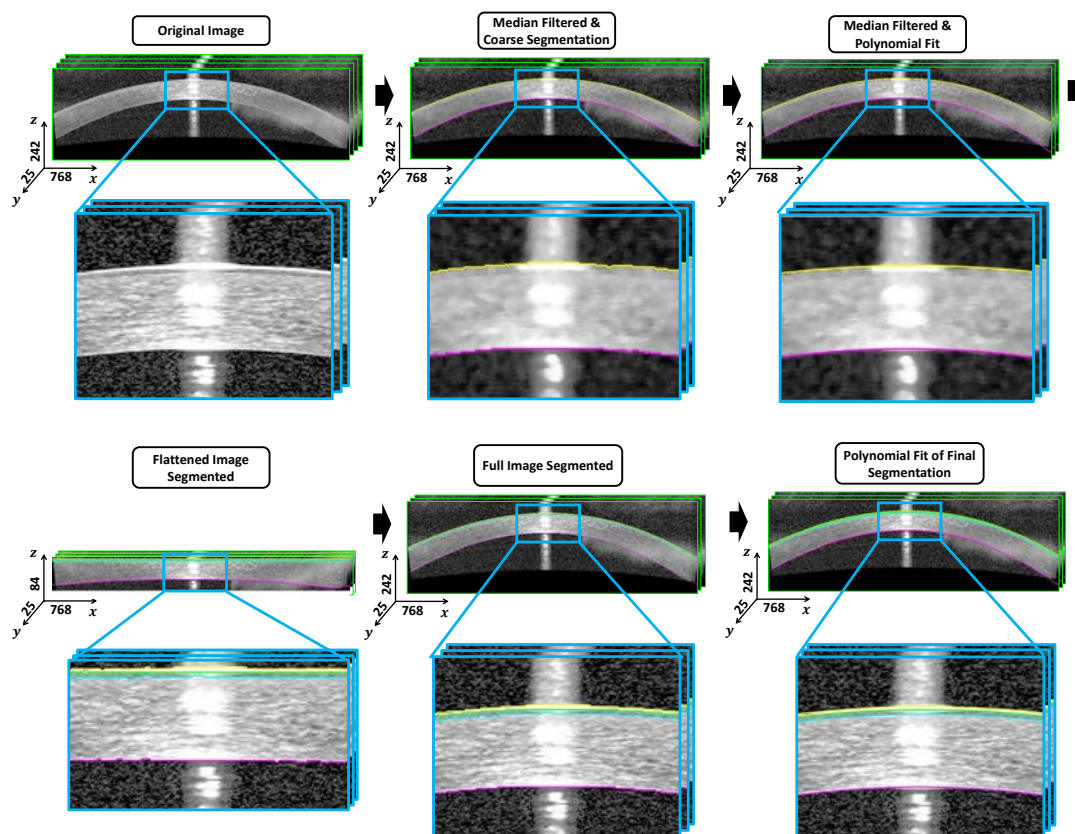
Figure 4.3: Results of the method in Aim 1 for human corneas.

4.1.1 Course Outer Layer Segmentation

With the iris appearing in most of the AS-OCT images of mice and often causing unintended interference in regards to inter-surfaces relations, it is important to develop an approach that can consider and prohibit such interference. This results in an approach with the ability to remove any parts of the image irrelevant to our segmentation process. The purpose of this section is to use the graph-theoretic approach to coarsely segment the outer layers of the cornea in human and mice data (also the pseudo-layers of the iris in mice data) to locate these respective structures in the volume. Let us first note the coordinate system for mice imagery which is in the r-θ-z directions and the human data coordinate system which is in the x-y-z directions.

To optimize for speed and memory efficiency, the mice imagery is first downsampled by eight in the r-z-direction. This is followed by a radial median filter in a 3×3 neighborhood to reduce any speckle noise. The graph-theoretic approach is used to determine an approximate surface location of the air-tear film boundary and endothelium-aqueous humor boundary while also providing a pseudo-surface that provides the approximate location of the iris. For this task, where the graph algorithm is segmenting four surfaces using only edge-based costs the cost function for all four surfaces for mice data will be of the form:

$$
\begin{aligned}
C_{Total} &= C_{\mathcal{S}_1(r,\theta)} + C_{\mathcal{S}_2(r,\theta)} + C_{\mathcal{S}_3(r,\theta)} + C_{\mathcal{S}_4(r,\theta)} \\
&= \sum_{i=1}^{4} C_{\mathcal{S}_i(r,\theta)}
\end{aligned}
\tag{4.1}
$$

where the edge-term costs of a given surface are represented for the mice data as:

$$
C_{\mathcal{S}_i(r,\theta)} = \sum_{\{(r,\theta,z)|z=\mathcal{S}_i(r,\theta)\}} \mathcal{I}_{c_{\mathcal{S}_i}}(r,\theta,z)
\tag{4.2}
$$

where $I_{c_{\mathcal{S}_i}}(r,\theta,z)$ is the edge-based cost function computed as the 1st order Gaussian

derivative in the vertical direction similar to the ones depicted in Fig. 3.3.

The human cornea images have a lower resolution than the murine ($768 \times 25 \times 242$ vs $1000 \times 100 \times 1024$) such that the downsampling as for the murine images is not required. In addition, the iris is not present in the human images; therefore the graph-theoretic approach only needs to find two surfaces, the tear film-air boundary and endothelium-aqueous humor boundary, before it is flattened. The cost functions for segmenting just two surfaces in the human data, which only include edge terms, are expressed as:

$$
\begin{aligned}
C_{Total} &= C_{\mathcal{S}_1(x,y)} + C_{\mathcal{S}_2(x,y)} \\
&= \sum_{i=1}^{2} C_{\mathcal{S}_i(x,y)}
\end{aligned}
\tag{4.3}
$$

These edge costs for a single surface are similar to those expressed in Eq. 4.2 shown again here in the human coordinate system:

$$
C_{\mathcal{S}_i(x,z)} = \sum_{\{(x,y,z)|z=\mathcal{S}_i(x,y)\}} \mathcal{I}_{c_{\mathcal{S}_i}}(x,y,z)
\tag{4.4}
$$

where $I_{c_{\mathcal{S}_i}}(x,y,z)$ is the edge-based cost function computed as the 1st order Gaussian derivative in the vertical direction similar to the ones depicted in Fig. 3.3.

4.1.2   Polynomial Fit to Outer Layers

Fitting a polynomial to the coarse segmentation helps in the presence of imaging artifacts as shown in Fig. 4.4. Additionally, this allows us to incorporate shape priors for the graph algorithm further down the methodology pipeline. With the coarse segmentation in place, the surfaces found between the air-tear film boundary and endothelium-aqueous humor boundary in the mice corneas are upsampled back to the original resolution using linear interpolation and smoothed to remove any waviness caused by the interpolation.

For both data sets, and in each B-scan individually, we fit a third-order polynomial
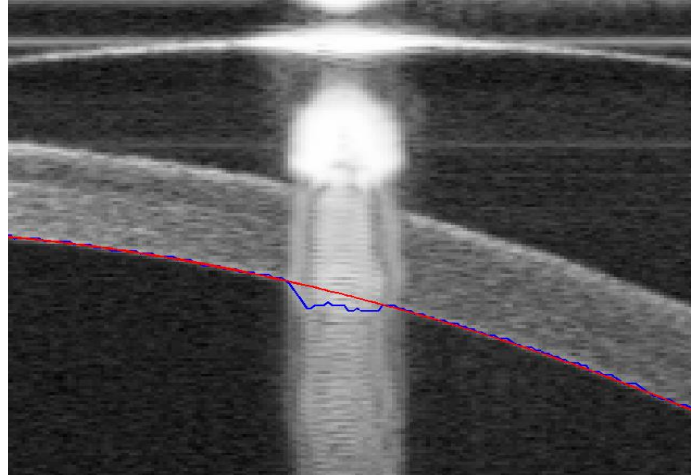
Figure 4.4: Common imaging artifact found in AS-OCT images. Fitting a polynomial to the initial coarse segmentation via weighted least squares prevents the image artifact from incorrectly flattening the image.

curve of the form shown in Eq. 4.5 to the top and bottom corneal surfaces using robust weighted least squares. The reason we use a third-order polynomial is that human corneas tend to increase in thickness as we reach the outer edges of the cornea where they meet the iris while murinate corneas tend to taper off. A third-order polynomial fit is robust enough to work for both cases.

$$p(x) = p_3 x^3 + p_2 x^2 + p_1 x + p_0 \qquad (4.5)$$

Let us consider first how to determine the least squares solution to the polynomial fit problem and for simplicity let us consider the case for a first-degree polynomial.

$$y = p_1 x + p_0 \qquad (4.6)$$

Suppose we have n data points that can be modeled by a first-degree polynomial. The least-squares method minimizes the summed square of residuals. Residuals are defined

as the difference between the observed response value y_i and the fitted response value $\hat{y}_i$ expressed as:

$$r_i = y_i - \hat{y}_i \tag{4.7}$$

Then given all the data points, the summed square of residuals can be expressed as a system of n simultaneous linear equations in two unknowns:

$$E = \sum_{i=1}^{n}(y_i - (p_1 x_i + p_2))^2 \tag{4.8}$$

To determine the coefficients, we differentiate E with respect to each of the parameters and set the results equal to zero.

$$\begin{aligned}
\frac{\delta E}{\delta p_1} &= -2\sum_{i=1}^{n} x_i(y_i - (p_1 x_i + p_2)) = 0 \\
\frac{\delta E}{\delta p_2} &= -2\sum_{i=1}^{n}(y_i - (p_1 x_i + p_2)) = 0
\end{aligned} \tag{4.9}$$

We express the estimates of the true parameters by a variable b where we substitute it in the previous equations as:

$$\begin{aligned}
\sum_{i=1}^{n} x_i(y_i - (b_1 x_i + b_2)) &= 0 \\
\sum_{i=1}^{n}(y_i - (b_1 x_i + b_2)) &= 0
\end{aligned} \tag{4.10}$$

Note the -2 has been omitted as it will be canceled when solving the equations. We can continue by arranging the equations in the following form commonly noted as the *normal equations*:

$$\begin{aligned}
b_1 \sum_{i=1}^{n} x_i^2 + b_2 \sum_{i=1}^{n} x_i &= \sum_{i=1}^{n} x_i y_i \\
b_1 \sum_{i=1}^{n} x_i + n b_2 &= \sum_{i=1}^{n} y_i
\end{aligned} \tag{4.11}$$

Solving for b_1 and then substituting the solution to find b_2 we get:

$$b_1 = \frac{n \sum_{i=1}^{n} x_i y_i - \sum_{i=1}^{n} x_i \sum_{i=1}^{n} y_i}{n \sum_{i=1}^{n} x_i^2 - (\sum_{i=1}^{n} x_i)^2}$$

$$b_2 = \frac{1}{n}(\sum_{i=1}^{n} y_i - b_1 \sum_{i=1}^{n} x_i)$$

(4.12)

The solution is similar for higher degree polynomials but obviously more tedious. Instead of similarly deriving the least-squares solution for the third-degree polynomial fit from Eq. 4.5 let us alternatively find the least-squares solution for the linear model expressed in matrix form. We can express the linear model in matrix form as:

$$y = X\beta + \epsilon$$

(4.13)

where

- y is an $n \times 1$ vector of responses (i.e. surface points in a B-scan)

- β is an $m \times 1$ vector of the coefficients we wish to find that best fit the surface points

- X is the $n \times m$ design matrix for the model

- ϵ is an $n \times 1$ vector of errors

For the third-degree polynomial, the n equations are expressed in terms of y, X, and β as

$$\begin{bmatrix} y_1 \\ y_2 \\ \vdots \\ y_n \end{bmatrix} = \begin{bmatrix} x_1^3 & x_1^2 & x_1 & 1 \\ x_2^3 & x_2^2 & x_2 & 1 \\ \vdots & \vdots & \vdots & \vdots \\ x_n^3 & x_n^2 & x_n & 1 \end{bmatrix} \times \begin{bmatrix} p_3 \\ p_2 \\ p_1 \\ p_0 \end{bmatrix}$$

(4.14)

The sum of squares error estimate can be expressed as:

$$E = \sum_{i=1}^{n} (y_i - (p_3 x_i^3 + p_2 x_i^2 + p_1 x_i + p_0))^2$$

(4.15)

The least squares solution to the problem is then a vector b that estimates the unknown coefficients in β. The normal equations are given as:

$$(X^T X)b = X^T y \tag{4.16}$$

where solving for b yields:

$$b = (X^T X)^{-1} X^T y \tag{4.17}$$

It is known that regular least-squares fitting is sensitive to outliers therefore instead we use a weighted scheme so as to minimize outliers like those in Fig. 4.4, from affecting our polynomial fit [88].

Then now let's look at the weighted least squares problem. For this application, it is formulated as a system of n simultaneous linear equations in four unknowns similar to regular least-squares fitting but with weights applied to minimize the error estimate E as follows:

$$E = \sum_{i=1}^{n} w_i (y_i - (p_3 x_i^3 + p_2 x_i^2 + p_1 x_i + p_0))^2 \tag{4.18}$$

where the weights are expressed according to the variance of the measurement errors as:

$$w_i = \frac{1}{\sigma_i^2} \tag{4.19}$$

and the least squares solution is again a vector b which estimates the unknown vector of coefficients β such that:

$$(X^T W X)b = X^T W y \tag{4.20}$$

or

$$b = (X^T W X)^{-1} X^T W y \tag{4.21}$$

where

$$W = diag(w_1, w_2, \cdots, w_n) \tag{4.22}$$

Plugging the solution back in for b gives us the predicted response $\hat{y}$, expressed as:

$$\hat{y} = Xb = X(X^T W X)^{-1} X^T W \tag{4.23}$$

and the residuals can simply be calculated as in Eq. 4.7.

At this point, there are two main options to consider with regards to the weighting influence of data points. The Least-Absolute-Residuals (LAR) method minimizes the absolute difference of the residuals rather than the squared differences. Bisquare weights minimize the weighted sum of squares of the residuals where the influential weight of a point to the fit diminishes the further away that data point is from the fitted line. In essence, LAR is better suited for cases where all data points are as equally viable as any other. Bisquare weight distribution is preferred in our case because it seeks to find an optimal fit with the majority of the data and it minimizes the effect of outliers caused by noise commonly seen in OCT images (Fig. 4.4) [88].

Let us now look at how bisquare weight distribution is applied to our polynomial fit regression problem. The algorithm to fit a polynomial to the surface by adapting bisquare weight distribution uses iterative reweighted least squared and is computed as follows:

1. Fit the model using weighted least squared as described above.

2. Compute the *adjusted residuals* and standardize them. The adjusted residuals are given as:

$$r_{adj} = \frac{r_i}{\sqrt{1 - h_i}} \tag{4.24}$$

where r_i are the least squares residuals described above and h_i, called the leverages, express how far a variable is from its mean. The leverages help by reducing

the weight of high leverage data-points which would otherwise have a larger effect on the least-squares fit. The standardized residuals are then:

$$u = \frac{r_{adj}}{Ks} \tag{4.25}$$

where K is a tuning constant set as 4.685 (chosen to provide 95% asymptotic efficiency as that of least-squares [89]) and s is the robust variance expressed as $MAD/0.6745$ where MAD is the median absolute deviation of the residuals expressed as $MAD = median(|r_i - median(r_i)|)$

3. Compute the robust weights as a function of u where the bisquare weights are expressed as:

$$w_i = \begin{cases} (1 - (u_i)^2)^2, & |u_i| < 1 \\ 0, & |u_i| \geq 1 \end{cases} \tag{4.26}$$

4. If the fit has converged, then we are done. Otherwise, continue iterating from step 1.

4.1.3 Image Flattening and Simultaneous Segmentation

With the polynomial estimation in place to determine an approximation of the outer surfaces, the image can be further cropped and flattened. The remaining volume is now only compromised of the corneal structures we are interested in segmenting reducing computation time and memory usage. Following suit, now all the layers in the volume can be segmented using the graph-theoretic approach with the addition of incorporating shape-prior information. The edge-based cost functions are developed using Gaussian derivative functions similar to those depicted in (Fig. 3.3) and are

expressed as in Eq. 4.2 shown again here for convenience. For mice they are:

$$C_{\mathcal{S}_i(r,\theta)} = \sum_{\{(r,\theta,z)|z=\mathcal{S}_i(r,\theta)\}} \mathcal{I}_{c_{\mathcal{S}_i}}(r,\theta,z) \tag{4.27}$$

and for humans they are:

$$C_{\mathcal{S}_i(x,y)} = \sum_{\{(x,y,z)|z=\mathcal{S}_i(x,y)\}} \mathcal{I}_{c_{\mathcal{S}_i}}(x,y,z) \tag{4.28}$$

where $\mathcal{I}_{c_{\mathcal{S}_i}}(r,\theta,z)$ and $\mathcal{I}_{c_{\mathcal{S}_i}}(x,y,z)$ are the edge-based cost functions computed as the 1st order Gaussian derivatives in the vertical direction. With the incorporation of shape-term prior information, additional cost functions are introduced and are expressed in the mice data as:

$$C_{Sp_i} = \sum_{\{(r_1,\theta_1),(r_2,\theta_2)\in\mathcal{N}_c\}} f(\mathcal{S}_i(r_1,\theta_1) - \mathcal{S}_i(r_2,\theta_2) - m_{(r_1,\theta_1),(r_2,\theta_2)}) \tag{4.29}$$

and for human data as:

$$C_{Sp_i} = \sum_{\{(x_1,y_1),(x_2,y_2)\in\mathcal{N}_c\}} f(\mathcal{S}_i(x_1,y_1) - \mathcal{S}_i(x_2,y_2) - m_{(x_1,y_1),(x_2,y_2)}) \tag{4.30}$$

The equation for all the cost functions is then expressed for the mice data as:

$$\begin{aligned} C_{Total} &= C_{\{\mathcal{S}_1(r,\theta),\mathcal{S}_2(r,\theta),...,\mathcal{S}_4(r,\theta)\}} + C_{\{\mathcal{S}_{Sp_1},\mathcal{S}_{Sp_2},...,\mathcal{S}_{Sp_4}\}} \\ &= \sum_{i=1}^{4} C_{\mathcal{S}_i(r,\theta)} + \sum_{i=1}^{4} C_{\mathcal{S}_{sp_i}}. \end{aligned} \tag{4.31}$$

where $C_{\mathcal{S}_i(r,\theta)}$ is the edge-based cost function and $C_{\mathcal{S}_{sp_i}}$ is the shape-term cost function for the $i'th$ surface. The human data is expressed similarly but in the human data

coordinate system as:

$$C_{Total} = C_{\{\mathcal{S}_1(x,y),\mathcal{S}_2(x,y),...,\mathcal{S}_4(x,y)\}} + C_{\{\mathcal{S}_{Sp_1},\mathcal{S}_{Sp_2},...,\mathcal{S}_{Sp_4}\}}$$
$$= \sum_{i=1}^{4} C_{\mathcal{S}_i(x,y)} + \sum_{i=1}^{4} C_{\mathcal{S}_{sp_i}}. \tag{4.32}$$

where $C_{\mathcal{S}_i(x,y)}$ is the edge-based cost function and $C_{\mathcal{S}_{sp_i}}$ is the shape-term cost functions for the $i'th$ surface.

The method, as discussed in section 3.2, allows for a convex function $f(h)$ that penalizes the cost of the surface set if it deviates from the expected, mean shape. The convex function used in our work takes the form of a second order polynomial. In this flattened image, the expected mean shape is 0, that is, the surface is not expected to deviate from the straight-flat direction. If it does deviate from this expected mean shape it will pay a penalty cost to do so. Once all four surfaces have been segmented they will then be translated back to the original image space.

4.1.4 Polynomial Fit for Final Segmentation

Due to the well-behaved shape of the cornea, the graph-theoretic segmentation can be optimized further by fitting another polynomial to the final segmentation results The same procedure is used as that in Section 4.1.2 but is now applied to all the surfaces. This method provides a smooth boundary between all surfaces in question which provides more accurate results for thicknesses measurements and further analysis.

4.2 Experimental Methods

4.2.1 Data and Reference Standard

The murine dataset included 58 AS-OCT radial-protocol scans of mice with varying degrees of corneal thickness ranging from 54 μm at their thinnest to 138 μm at their thickest. Examples of the imaging protocol used to acquire the AS-OCT im-

agery of mice can be seen in Fig. 4.5. The images were acquired using the Bioptigen optical coherence tomographer (Bioptigen Inc., Durham, NC) at the University of Iowa. The size of each scan was $1000 \times 100 \times 1024$ voxels given in the r-θ-z direction, respectively. The images were acquired at an 8-bit grayscale bit depth. The physical dimensions were 2mm in the r-direction and 1.57mm in the z direction. Physical dimension in between slices can vary due to radial acquisition but can be expressed as $y_i = \frac{1.8\pi}{180}r$ where r corresponds to the distance from the center of the radial scan.

The human dataset included 37 AS-OCT raster-protocol scans of humans with varying degrees of corneal thickness ranging from 554 μm at their thinnest to 998 μm at their thickest. Examples of the imaging protocol used to acquire human AS-OCT imagery can be seen in Fig. 4.5. The images were acquired using a Spectralis optical coherence tomographer (Heidelberg Engineering Inc., Carlsbad, CA) at the University of Iowa. The size of each scan was $768 \times 25 \times 242$ voxels given in the x-y-z direction, respectively. The images were acquired at an 8-bit grayscale bit depth. The physical dimensions were 8.3mm in the x-direction and 2.61mm in the z-direction with a distance of 0.69mm in the y-direction between slices.

The graph-based segmentation portion of the algorithm was run on a Linux server with the openSUSE 13.2 operating system, AMD Opteron 6180 SE processor (12 cores) at 2.5Ghz, and 264GB of RAM. The polynomial fitting algorithm was run on a Windows 7 64-bit operating system with an Intel Xeon E5 1620 (4 cores) at 3.7Ghz and 64GB of RAM.

The reference standards for the cornea layer segmentation were obtained from manual segmentations of the corneal layers given by experts familiar with corneal structures. The reference standards were acquired similarly for both human and murine data. For each volume in all the data sets five random slices from that volume were chosen to be manually segmented. A total of 290 AS-OCT slices were manually segmented from the murine data set. While there were 185 AS-OCT slices available
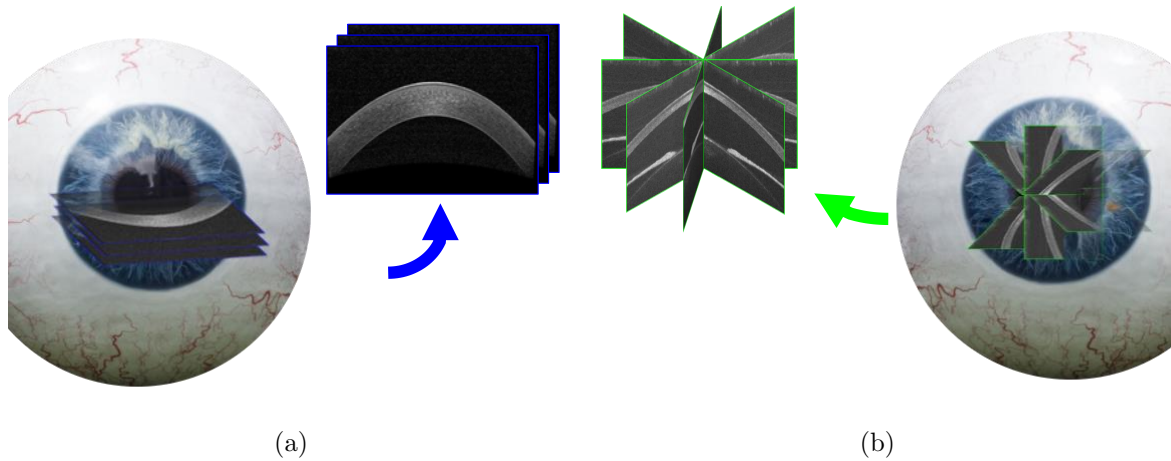
Figure 4.5: (a) Rectangular (raster) scanning protocol for corneal AS-OCT of humans. (b) Radial scanning protocol for corneal AS-OCT of mice. 3D eyeball imagery courtesy of [90].

from the randomly selected human data set for manual tracings, the expert omitted 8 of the 185 human AS-OCT slices from the manual segmentation due to corruption in the image, namely due to significantly incoherent and corrupt surface information, leaving 177 manually segmented human AS-OCT slices. An example of the imagery omitted can be found in Fig 4.6. The expert-based segmentation was performed on all three surfaces with in-house software designed for manual image tracing. The software had the user choose points corresponding to the surface in the image fitting splines to the chosen points.

4.2.2 Experiments

The images were evaluated based on a comparison between manually delineated slices and automatically segmented slices using unsigned border positioning error (UBPE). That is, the average unsigned mean differences between the delineated points and automated algorithm results were computed in each B-scan. We first took the mean of these results from each B-scan followed by the overall mean and standard
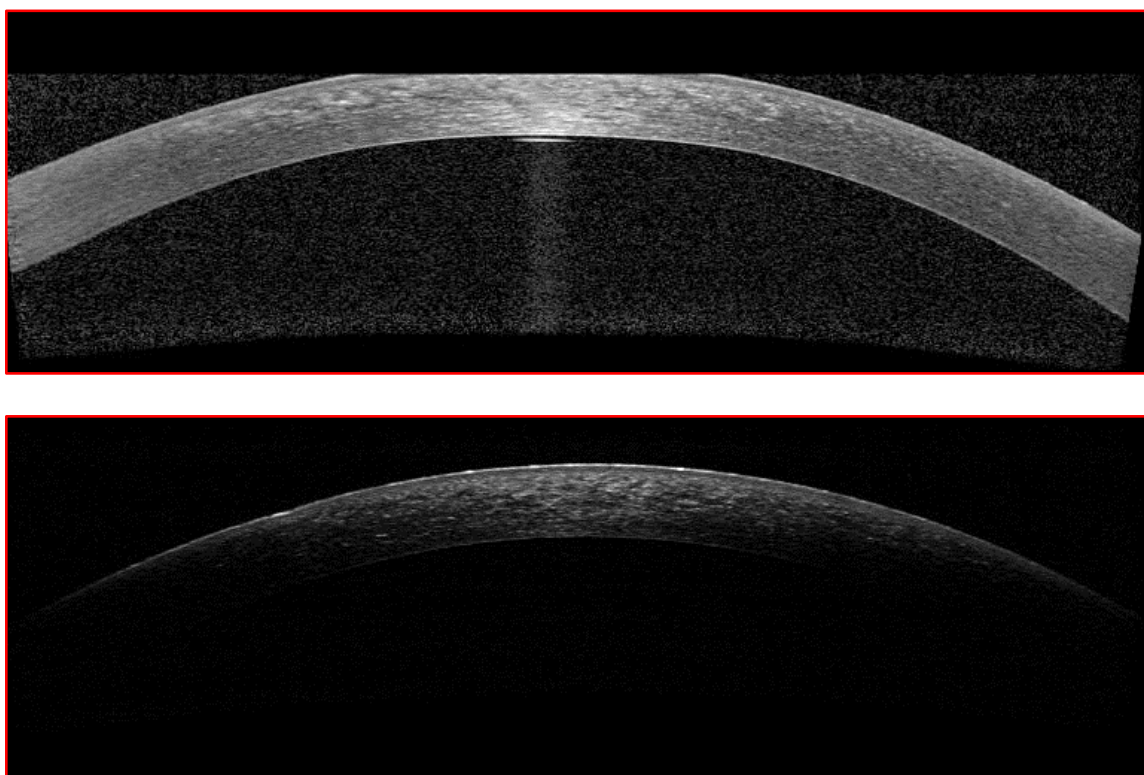
Figure 4.6: Examples of images omitted by the expert for manual segmentation due to incoherent and corrupt surface information.

Table 4.1: Accuracy of segmentation results of murine
data (Mean UBPE ± SD across B-scans).

Layer Boundary	Pixels	Microns
Air-Epithelium	1.47 ± 1.62	2.26 ± 2.47
Bowman's Layer-Stroma	3.22 ± 2.73	4.92 ± 4.18
Endothelium-Aqueous Humor	3.86 ± 2.95	5.91 ± 4.51
Total	2.85 ± 2.70	4.36 ± 4.13

deviation of these results across all B-scans from all the volumes. The UBPE was considered for each individual surface in mice, for each individual surface in humans, for all surfaces in mice, and for all surfaces in humans. Furthermore, the imagery also exhibited lighting discrepancies toward the edges where no coherent surface information could be had or no surface information existed at all. This is why we also considered error versus location wherein we explored how the error varies based on its distance from the center of the image where lighting discrepancy was at its lowest.

4.3 Results

Examples of the segmentation for mice corneas are shown in Fig. 4.7 and similar results for human corneas are shown in Fig 4.8.

The unsigned border positioning errors are reported in Table 4.1 and Table 4.2 for mice and human data respectively. The mean unsigned border positioning error was computed as described in the previous section and was found to be 4.36 ± 4.13 μm (2.85 ± 2.70 pixels) for the mice data set and for the human data set it was 13.67 ± 12.72 μm (1.27 ± 1.18 pixels).

The variation in unsigned border positioning error versus the distance from the center of the image can be seen in Fig. 4.9 for the human data set coupled with an example of a slice illustrating the common artifacts and corrupted surface information at the edge of the image. Similarly, Fig. 4.10 depicts a similar plot and imagery example for the mice data set.
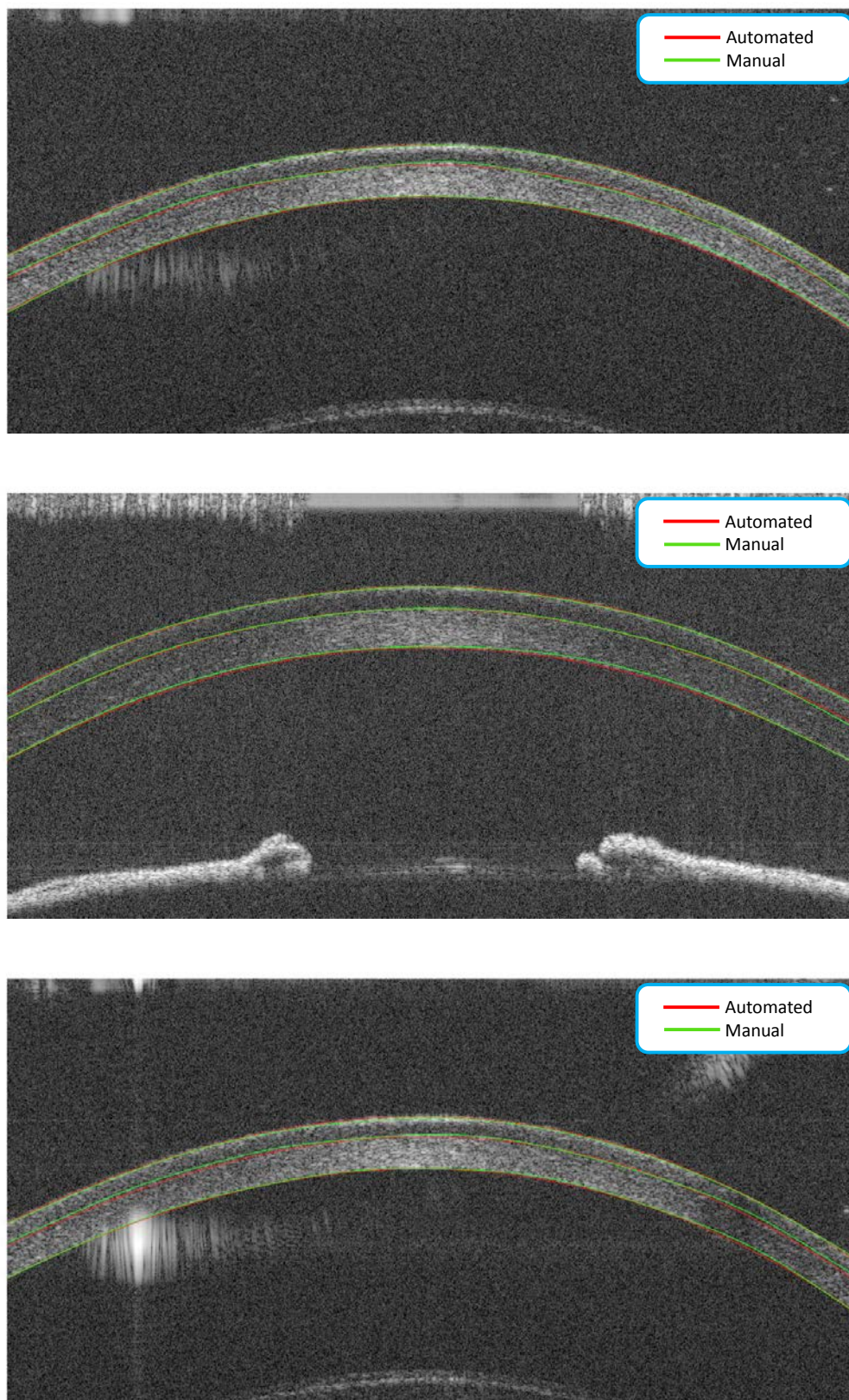
Figure 4.7: Examples of the automated results of our method versus manually delineated surfaces in corneal AS-OCTs of mice. Automated segmentation results are depicted in red while manual segmentations are shown in green.
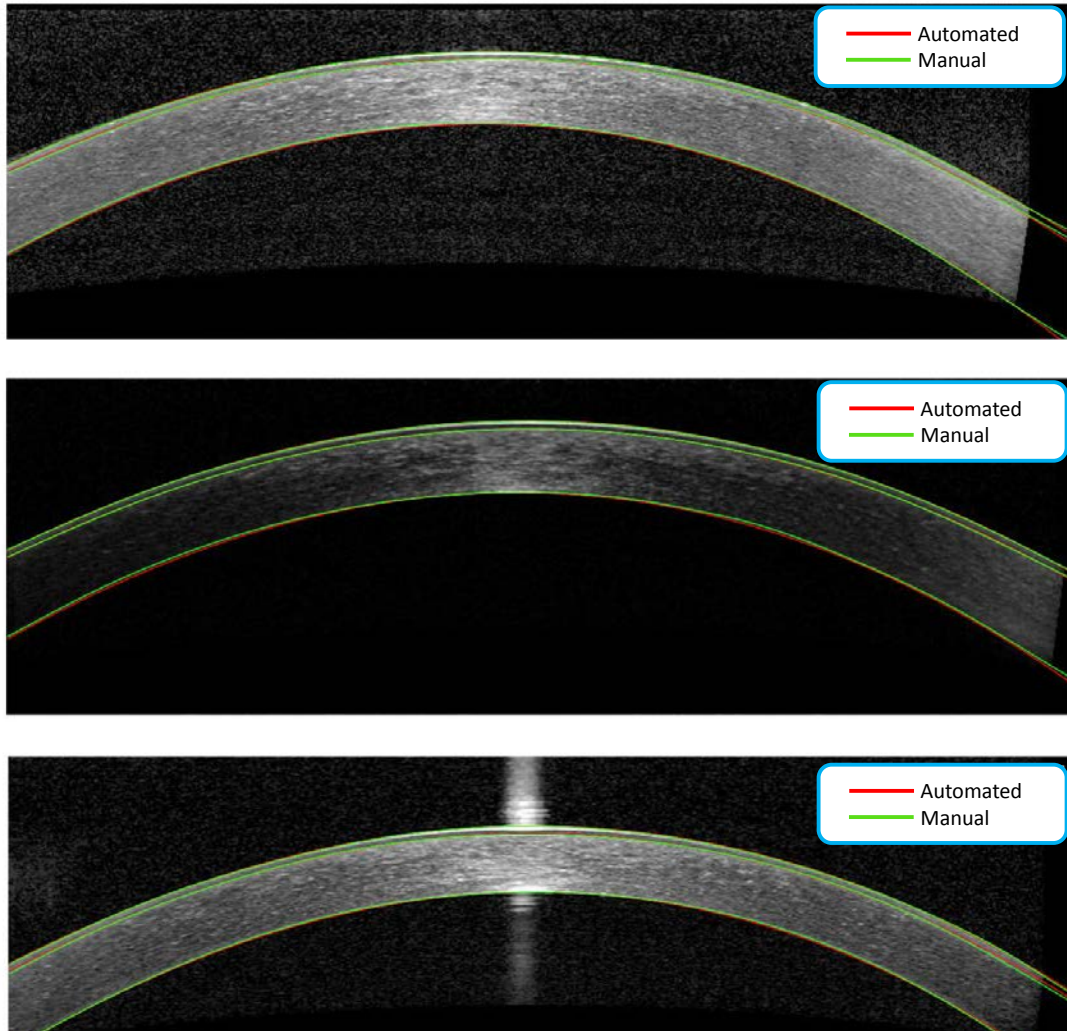
Figure 4.8: Examples of the automated results of our method versus manually delineated surfaces in corneal AS-OCTs of humans. Automated segmentation results are depicted in red while manual segmentations are shown in green.

Table 4.2: Accuracy of segmentation results of human data (Mean UBPE $\pm$ SD across B-scans).

Layer Boundary	Pixels	Microns
Air-Epithelium	0.74 ± 0.49	8.02 ± 5.32
Bowman's Layer-Stroma	0.99 ± 0.61	10.67 ± 6.59
Endothelium-Aqueous Humor	2.07 ± 1.6	22.33 ± 17.25
Total	1.27 ± 1.18	13.67 ± 12.72
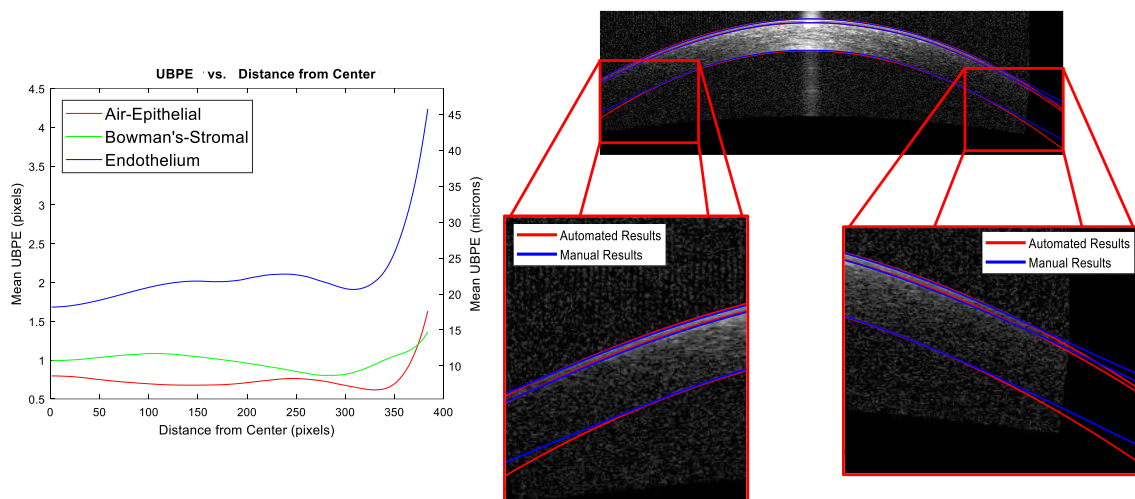
Figure 4.9: The plot showing the increase in unsigned border positioning error as we stray from the center of the image along with an image illustrating the missing image information found in the outer boundaries of the human corneal AS-OCTs.
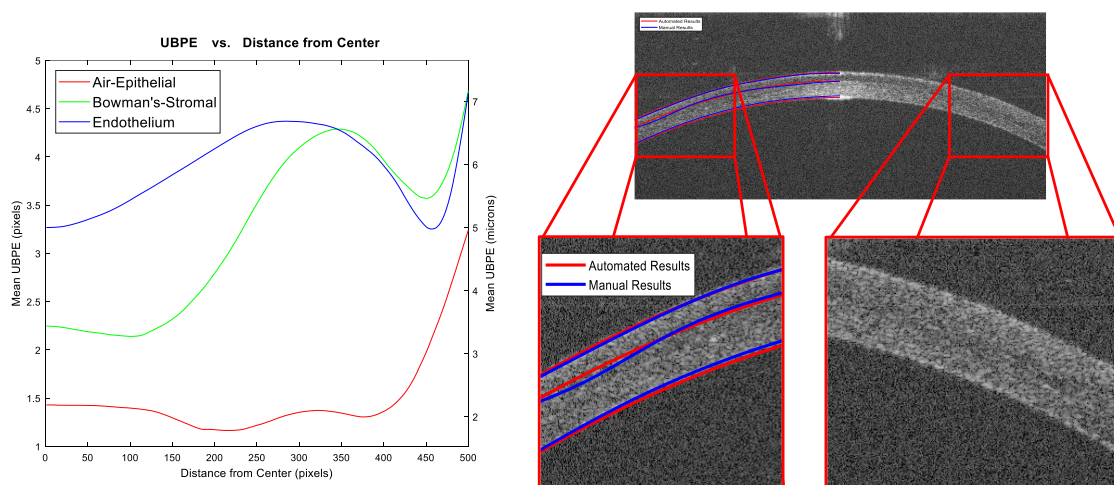
Figure 4.10: The plot showing the increase in unsigned border positioning error as we stray from the center of the image along with an image illustrating the missing surface information found on the edges of the corneal AS-OCTs of mice.

4.4 Discussion and Conclusion

In this chapter, we implemented an algorithm that could successfully segment the corneal layers in AS-OCT imagery to find the air-epithelium, Bowman's layer-stroma boundary, and the endothelium-aqueous humor boundary. The approach was tested on 58 murine images and 37 human images. The method was able to successfully find the boundaries in AS-OCT images utilizing the shape-prior information of the cornea that was incorporated into the graph-theoretic approach.

Results showed a comparable accuracy versus manual segmentation (Table 4.1 and Table 4.2) allowing for a possible alternative to manual segmentation without the need for manual interaction, which is often times an impractical time-consuming option in a clinical setting.

Our method differs significantly to prior works discussed in Ch. 3 due mainly to its novelty in segmenting all the surface simultaneously in 3D whereas previous approaches segment boundaries only in 2D and individually. This allows for more relevant structural information to be extracted including volume and area measurements that encompass the entire cornea and also utilize this 3D volume information *a priori*, incorporating it into the graph-based segmentation algorithm.

The limitations of the approach become apparent when nonexistent surface information in the outer boundaries of the imagery can be seen to affect the overall accuracy when compared to expert tracings. Fig. 4.9 and Fig. 4.10 support these findings but it must be noted that at these outer boundaries of the image the expert is also using a best-guess approach due to the lack of surface information and as such is also extrapolating in their efforts to find the surfaces manually. Future consideration could be made for having multiple experts segment the volumes while minimizing inter-observer variability and incorporating machine-learning techniques that consider previous segmentation results to enhance the accuracy of the segmentation at locations with missing surface information.

To the best of our knowledge, this is also the only approach to have segmented murine data. This gives evidence to robustness in being able to evaluate corneal structures from varying sources, namely between the significantly varying physical sizes between human and murine corneas, and between different manufacturers of AS-OCT imagery. With the similarities in corneal structures between humans and mice, it becomes apparent that this robustness can aid in correlating any relative structure information commonly shared between human and mice corneas.

In summary, we showed strong evidence of an automated surface segmenting algorithm, the first of its kind for the application of simultaneously finding boundaries in 3D corneal AS-OCT imagery. The method proved effective in the imagery of different manufacturers of AS-OCT imagery as well as significantly varying corneal structures both in murine and human data. We believe it to prove effective for extracting corneal structure measurements for future works studying the dynamic effect of ophthalmic diseases on the corneal structures.

CHAPTER 5
PANORAMA AND CORNEAL NERVE SEGMENTATION FROM IVCM IMAGERY OF THE SUB-BASAL NERVE PLEXUS

The clinical background and previous works laid out in Ch. 2 and Ch. 3 discuss notable ophthalmic diseases and how they can impact corneal structures. As such, it is critical to be able to determine the relation that ophthalmic diseases have with corneal structures. In-vivo confocal microscopy (IVCM) is a non-invasive modality that can help us achieve these goals. IVCM provides images of the sub-basal nerve plexus which allow us to measure the corneal nerve density; one downside to this imaging protocol is that it can be limited by its field of view. Establishing an approach that can expand on the field of view of IVCM coupled with an automated method to segment the corneal fiber layers can provide a larger area of interest and more accurate criterion for assessing the change to corneal structures from ophthalmic diseases. Not only can it help determine the impact of ophthalmic diseases for cross-sectional studies, but with a larger area of interest, being able to find the same areas in the nerve plexus over longitudinal studies can help monitor the progression of possible treatments as well.

The works presented in this section are described in two parts. First, we developed an algorithm to create panoramas of IVCM imagery to provide a larger field of view of the sub-basal nerve plexus. Secondly, we developed an approach wherein we adapt prior machine learning and segmentation techniques to segment the corneal nerves contained within single IVCM images and in the panoramas as well.

5.1 Methods

5.1.1 Registering Multiple IVCM Images of the Sub-Basal Nerve Plexus

Registering medical images from the in-vivo acquisition can pose a challenge. Due to inherent motions from the acquisition, problems can arise including significant spatial differences, textural differences, and illumination variation between the

images. This is why feature-based registration is more suited for this application as opposed to image intensity-based methods. The purpose of these works is to provide a registration algorithm that is less sensitive to these inherent properties and can reliably register the set of images. This includes a feature set that is scale-invariant, rotation-invariant, and illumination-invariant where the features can be reproduced. We describe a method below that uses a pair-wise feature-based registration algorithm to first develop an image pair metric system for all images in a set. The algorithm then builds a graph using the metrics from the pair-wise registration to determine connectivity and ultimately evaluate what image groups form each panorama. In addition, we use the properties of the graph to determine the optimal order in which to register the images. The method follows by using a distance weighting scheme shown in previous works to work for retinal and corneal imagery [25,91] to seamlessly blend the images together. The algorithm continues iteratively using the resulting panoramas from the initial image-pair results to determine if any more connections exist between the panoramas created in the first pass. We stop when there are no more possible matches between results.

5.1.1.1 Pair-Wise Feature-Based Similarity Registration

Registering the images will require using feature-based descriptors that are invariant to the properties described in Ch.3. The registration is similar to the method described in [85] but rather than registering a single pair of images we will utilize the method to perform pair-wise image registration between all image pairs in a set in order to determine which images can be registered w.r.t. each other to produce viable panoramas from each image set. That is, given a set of images $\{I_1(x,y), I_2(x,y), ..., I_n(x,y)\}$ we perform pairwise registration between an image $I_i(x,y)$ and all other images $\{I_1(x,y), I_2(x,y), ..., I_{i-1}(x,y), I_{i+1}(x,y), ...I_n(x,y)\}$ for each image in the set. The method will also be used for sequential image registration when building the final panoramas later on. The feature-based registration method

is described below:

- **Feature Detection**

  Strictly using common features like the results of FAST corner detection [92] as a point-based registration method can provide moderate results for most applications; unfortunately this cannot be guaranteed for microscopy images due to significant illumination differences between images, the dynamic z-depth change from a moving patient, and the curved nature of the cornea. Thus further incorporating a more detailed feature set around the neighborhood of the FAST corner detection aids us in finding the actual corresponding control points shared between images.

  The feature detection algorithm we employed is that of Dalal et al. [76], the histogram of oriented gradient (HoG). The method determines a neighborhood around the detected corner points labeled as blocks wherein HoGs are compiled for the pixels in 4x4 pixel cells within that block. This makes the descriptor resistant to translation or rotation so long as these geometric transforms are smaller than the local spatial/orientation bin size used to find the HoG descriptors. Similarly, the localized histograms are contrast-normalized to ensure invariance to illumination and shadowing. This is achieved by measuring the intensity around the block, then using that result to normalize all the cells within that block. An example of the feature generation is shown in Fig. 5.1.

- **Feature Point Matching**

  With the features generated to describe points of the image we next determine the closest feature vector between images $I(x, y)$ and $J(x, y)$. Given all feature vectors corresponding to $I(x, y)$ denoted as $H_I = \{h_{I,1}, h_{I,2}, \cdots, h_{I,n}\}$ and all feature vectors for image $J(x, y)$ denoted as $H_J = \{h_{J,1}, h_{J,2}, \cdots, h_{J,n}\}$ where $h_{I,k}$ is the k'th HoG feature vector corresponding to image $I(x, y)$ then the best matching feature is found as follows [93]:

HoG features around the corner points
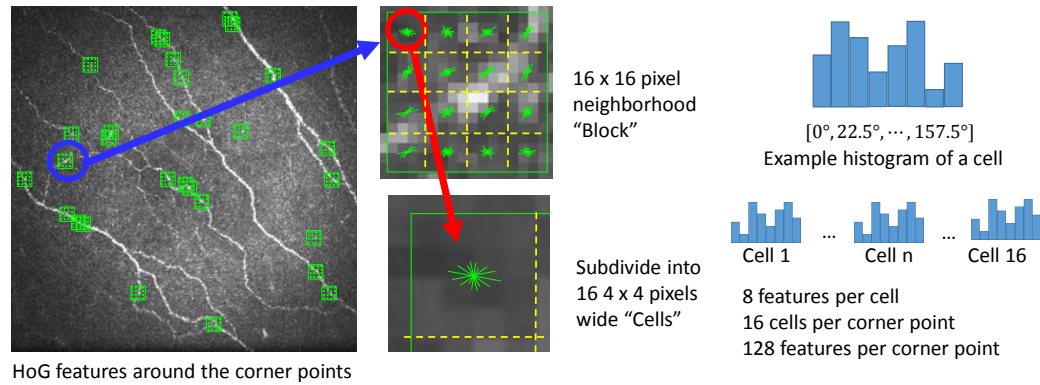
Figure 5.1: Feature design using FAST corner detection followed by Histogram of Oriented Gradients generation on the detected fast corners. Each corner is surrounded by a 16x16 pixel-wide block subdivided into sixteen 4x4 pixel-wide cells.

1. First, we determine the sum of squared differences between all feature vectors H_I from the first image and a feature vector $h_{J,1}$ from the second image for all said feature vectors as so:

$$E_{SSD}(1,i) = \sum_{j}^{128}[h_{I,1}(j) - h_{J,i}(j)]^2, i = 1, 2, \cdots, M \qquad (5.1)$$

2. Features having a distance larger than a threshold (0.2) are eliminated from further investigation.

3. Ambiguous matches, determined by dividing distances of subsequent feature vectors are also eliminated from a predetermined threshold (a conservative threshold of 0.8 works to prevent too much elimination).

- **Feature Pair Matching & Optimization**

  We continue by finding optimal corresponding points between images in order to compute the transformation matrix. The algorithm is expected to find a multitude of matching features between images in the forward direction, but
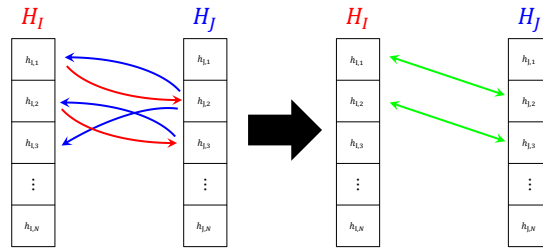
Figure 5.2: Optimized bilateral feature vector matching using approximate nearest neighbor [74, 93] where the final matching feature vector set between the forward direction (red) and backward direction (blue) is shown in green.

to ensure an optimal set of corresponding match points the method keeps any points from image $I(x, y)$ that are said to match with image $J(x, y)$ only if the reverse is also true. Corresponding bilateral matching points are determined using nearest neighbor approximation as proposed in [75]. The assumption here being that we have found more matching than mismatching points. An illustration of this feature vector matching technique is shown in Fig. 5.2.

In addition to finding optimal feature points, the method allows for refinement of control point pairs in a small neighborhood (5x5) to prevent any erroneous control point detection from image artifacts or illumination variance.

- **Transformation Matrix**

  When it is the case that we find significantly more than the set of three points required for image registration we will utilize random sample consensus (RANSAC) to take advantage of all these matching points. In its fundamental form, for registration, RANSAC works as follows:

  1. Randomly select a set of corresponding point pairs

  2. Fit a registration to the selected point pairs

  3. Determine the number of outliers from the registration

4. Repeat steps 1-3 for a prearranged set of iterations

The transformation matrix that we need to compute will be a similarity matrix, one that can scale, translate, and rotate the corresponding moving image. It is of the form:

$$T(x,y) = \begin{bmatrix} s\cos\theta & -s\sin\theta & x_c \\ s\sin\theta & s\cos\theta & y_c \\ 0 & 0 & 1 \end{bmatrix} \tag{5.2}$$

where s is the scaling factor, x_c, y_c are the translations in the x and y directions respectively, and θ is the rotation angle. RANSAC will help to find the optimal matching points from which to develop the transformation matrix.

- **Matching Metrics** When performing the pair-wise registration we must also consider metrics used to determine whether two images are registered well. This will aid further down in the methodology when determining what images are part of a panorama. The metrics we calculate are the following:

  1. **Inlier Mean Distance:** Inlier mean distance (IMD) is the mean distance between all the inlier point pairs chosen through the RANSAC algorithm.

  2. **Rotation & Scaling:** We also consider the rotation and scale in the x-direction and y-direction of the moving image to verify any distortions or rotations beyond reasonable means.

  3. **Mutual Information:** Mutual information describes the statistical dependence between two variables. For two discrete random variables X and Y, which represent the intensities from two overlapping images respectively, the mutual information can be described as:

$$I(X;Y) = \sum_{y \in Y} \sum_{x \in X} p(x,y) log(\frac{p(x,y)}{p(x)p(y)}) \tag{5.3}$$

where $p(x,y)$ is the joint probability distribution of X and Y and $p(x)$ and

$p(y)$ are the marginal probability distribution functions of X and Y respectively [94]. In general, aligned images will contain higher mutual information than misaligned images. The general limitation for using mutual information lies in the difficulty of obtaining reasonable estimates of $log(\frac{p(x,y)}{p(x)p(y)})$ since the probability density functions are usually not known. Instead, we use the mutual information estimation from Ceccarelli et al. [95] wherein the expectation is replaced by a sample mean and the probability density functions are derived using superposition of multiple Gaussian kernels where estimation maximation is applied to the Gaussian Mixture model. With N samples for X and Y described as (X_i, Y_i), $= 1 \ldots N$ then the kernel is expressed as:

$$K_i(\mathbf{u}; \mu_i, \sum_i) = \frac{1}{2\pi|\sum_i|^{\frac{1}{2}}} e^{-\frac{1}{2}(\mathbf{u}-\mu_i)^T \sum_i^{-1}(\mathbf{u}-\mu_i)} \tag{5.4}$$

and the model for the probability density function can be expressed as:

$$p(x,y) = \frac{1}{N} \sum_{i=1}^{N} K_i(x - X_i, y - Y_i) \tag{5.5}$$

with the mutual information estimated as:

$$I(X;Y) = \frac{1}{N} \sum_{j=1}^{N} log\left(\frac{\sum_i K_i(X_j - X_i, Y_j - Y_i)}{\sum_i K_i(X_j - X_i) \sum_i K_i(Y_j - Y_i)}\right) \tag{5.6}$$

4. **Normalized Cross-Correlation:** Normalized cross-correlation (NCC) is a measure of similarity between two functions via the displacement of one function with respect to the other. Naturally, this makes normalized cross-correlation a good candidate metric for determining the success of a registration. Consider two images $I_1(x,y)$ and $I_2(x,y)$ with some overlapping region $R_{I_1,I_2}(x,y)$ between them. The normalized cross-correlation in

the overlapping region is described as [96]:

$$NCC(I_1, I_2) = \frac{\sum\limits_{(i,j)\in R} I_1(i,j) \sum\limits_{(i,j)\in R} I_2(i,j)}{\sqrt{\sum\limits_{(i,j)\in R} I_1^2(i,j)}\sqrt{\sum\limits_{(i,j)\in R} I_2^2(i,j)}} \qquad (5.7)$$

5. **Mean-Squared Error:** Mean square error (MSE) is a measure of similarity between two images based on the difference in intensity values of the overlapping region between the images. This gives precedence for using MSE as a metric for evaluating the accuracy of registration. Consider two images $I_1(x,y)$ and $I_2(x,y)$ with some overlapping region $R_{I_1,I_2}(x,y)$ between them with M-number of rows and N-number of columns. The mean square error in the overlapping region is described as:

$$MSE(R_{I_1,I_2}(x,y)) = \frac{1}{MN} \sum_{i\in R}^{M} \sum_{j\in R}^{N} (I_1(i,j) - I_2(i,j))^2 \qquad (5.8)$$

5.1.1.2 *Image-Pair Metric Matrix*

Using the metrics from the pair-wise image registration we can construct a matrix relating all the various metrics between images. We want this metric to be represented in such a way that the higher the metric the higher probability that two images should be registered. To compute the final metric for each entry of the image-pair metric matrix (IPMM) we consider all the computed metrics and the total number of inliers found when we performed the image-pair registration. For the mean distance of the inlier points and the mean-squared error, higher values correspond to a lower matching probability; therefore, their inverse is taken before computing the final metric in order to have a direct relation to the overall matching metric.

Given image $I_1(x,y)$ and $I_2(x,y)$ we denote the inverse of the mean distance of the RANSAC inliers as $InlierDist^{-1}_{I_1,I_2}$, the normalized cross-correlation as NCC_{I_1,I_2}, the inverse mean square error as $MSE^{-1}_{I_1,I_2}$, the mutual information as MI_{I_1,I_2}, and

the number of inlier points between the images as $NumInliers_{I_1, I_2}$ then the entry for the final metric in the metric matrix between $I_1(x, y)$ and $I_2(x, y)$ would then be:

$$IPMM_{I_1, I_2} = [(InlierDist_{I_1, I_2}^{-1})(MSE_{I_1, I_2}^{-1})(NCC_{I_1, I_2})(MI_{I_1, I_2})]NumInliers \quad (5.9)$$

This is done for all possible image pairs in the data set to completely fill the metric matrix.

We also consider the scaling factors and rotations calculated from the pair-wise registration. To calculate the scaling, rotation, (and also the translation) parameters let us consider the general form of the similarity transformation matrix as expressed in Eq. 5.2. If we equate this to the transformation matrix computed through the automated pair-wise registration that we call T_a, we can compute these parameters. We define T_a as:

$$T_a = \begin{bmatrix} a & -b & t_x \\ b & a & t_y \\ 0 & 0 & 1 \end{bmatrix} \quad (5.10)$$

Equating it to Eq. 5.2 we get:

$$T_a = \begin{bmatrix} a & -b & t_x \\ b & a & t_y \\ 0 & 0 & 1 \end{bmatrix} = \begin{bmatrix} s\cos\theta & -s\sin\theta & x_c \\ s\sin\theta & s\cos\theta & y_c \\ 0 & 0 & 1 \end{bmatrix} \quad (5.11)$$

then as a result we get:

$$x_c = t_x \quad (5.12)$$

$$y_c = t_y \quad (5.13)$$

assuming s is positive:

$$s = \sqrt{a^2 + b^2} \qquad (5.14)$$

$$\theta = \begin{cases} tan^{-1}(\frac{b}{a}) & \text{if } a \neq 0 \\ 90°, & \text{if } a = 0 \text{ and } b > 0 \\ -90°, & \text{if } a = 0 \text{ and } b < 0 \end{cases} \qquad (5.15)$$

Empirically, we've noted that any images scaled beyond 10% or rotated more than $\pm 15°$ in either direction are considered a false positive and therefore their entry in the metric matrix will be reduced to 0. At this point in the methodology, there exists a maximum metric value for each image in the set.

Before proceeding further, additional thresholding is recommended to remove any metric values wherein a metric value for an image $I_i(x,y)$ may exist as the local maximum metric value for that corresponding image as $max(IPMM(I_i(x,y)))$ but that metric may be of a significantly low score at the overall global level $max(IPMM(I_i(x,y))) \ll IPMM_{global}$. This would indicate that, while an image-pair registration may exist, it might not provide a sanely reasonable or accurate registration. To solve this issue, Otsu's thresholding is performed on the histogram of the entire metric matrix to determine a sufficient threshold value to help determine an appropriate global metric value. Given the computed Otsu's threshold value as T_{IPMM} then for an entry in the IPMM between images $I_i(x,y)$ and $I_j(x,y)$ we keep the computed metric if it meets or exceeds T_{IPMM} otherwise we set it to 0 (Eq. 5.16).

$$IPMM_{I_i,I_j} = \begin{cases} IPMM_{I_i,I_j}, & IPMM_{I_i,I_j} \geq T_{IPMM} \\ 0, & otherwise \end{cases} \qquad (5.16)$$

5.1.1.3   Graph Construction

With multiple registration metrics in place, we consider then a means of grouping images together to form clusters and essentially form the panoramas themselves. To make the most use of the metric matrix we transform the metric matrix into a graph indicating an ideal image-to-image correspondence. Given an image in the data set, we look up the maximum metric value in the metric matrix for that respective image; this indicates the optimal corresponding image to register with respect to. In addition, we also consider any other metric values (and their corresponding images) that are within 90% of the maximum metric value for a given image. These subsets of image groups make up a subgraph, and eventually, also a panorama.

The graph is constructed by connecting edges between all images in the data set where the edge weights are related to the metric value as its inverse. Higher metric values can then correspond to lower edge weights in the graph. Given a set of images in a data set, the graph constructed relating the possible registration of image pairs is given as $G = (V, E)$ where $V(G)$ is a set of nodes (or vertices) corresponding to each image in the data set and $E(G)$ is the set of edges where each set describes the weighted connection between the two vertices. Let us consider the match metric between two images $s(x, y)$ and $t(x, y)$ and denote it as $f_{s,t}(x, y)$ then given a graph $G = (V, E)$ we describe their respective nodes such that $s \subseteq V$ corresponding to image $s(x, y)$ and $t \subseteq V$ corresponding to image $t(x, y)$ are connected with an edge $\{s, t\} \subseteq E$ with an edge cost of $f_{s,t}(x, y)^{-1}$. An example of the graph developed from implementing our method on a set of IVCM imagery can be seen in Fig 5.3.

To determine an optimal registration order for a cluster of images we consider an approach similar to the minimum spanning tree algorithm (MST). The MST is a subset of the edges of a connected undirected graph $G = (V, E_G)$ that connects all the nodes in a graph with the minimum possible total edge cost. At its basic core, the MST algorithm develops a tree $T = (V, E_T)$ for some subset of edges $E_T \subseteq E_g$

Figure 5.3: Example of a graph constructed from the registration algorithm used to find panoramas of IVCM imagery within a data set where nodes correspond to images in the data set and edges relate images that are to be registered together.

containing an arbitrary starting node $x \subseteq V$. At each step, the algorithm augments T with a least-weight edge between node x and node y such that $x \subseteq V$ is also in the tree T but $y \subseteq V$ has not yet been added to the tree. The algorithm iterates until all nodes in the original graph $G = (V, E_G)$ have been added to the MST $T = (V, E_T)$.

At this point, it's important to note that in our findings the construction of a graph has produced subgraphs that are essentially already in the form of an MST. These results have been completely coincidental based on the data we have acquired. Regardless we believe we should still consider cases where the graph constructions won't always produce an MST by default. This is why we implemented the next portion of our works.

In order to account for times when graph construction produces subgraphs that are not an MST by nature, we use an approach in our works similar to the MST algorithm with an emphasis more so on the order we traversed the graph to find the

appropriate image registration path from the subgraph and less so on the resulting MST itself. We initialize a tree $T = (V, E_T)$ with a starting node $a \subseteq V$, but we chose the initial node such that it contains the lowest edge cost in the entire subgraph. We iteratively traverse the graph, adding the next least-weight edge between the node a and a node $b \subseteq V$ not already contained within the graph, that is $E_T\{a, b\} \subseteq E_G$. We iterate until all nodes in the graph have been added to the tree. The node order in which we traverse the graph is retained and used as the order in which we register the nodes in a cluster. The sequential registration is accomplished using the same registration algorithm as that implemented previously for the pair-wise registration. This time, we find an affine transformation matrix that allows shearing as well for a more accurate registration. An example of a node cluster can be seen in Fig 5.4 with iterative results of a sequential image registration pipeline shown in Fig 5.5.

To better evaluate the imagery and produce quantifiable results from the registered panoramas we want to be able to seamlessly blend the images while limiting the loss of structural information. An elementary approach to blend registered images is simply taking the average of the intensity value of the pixels from both images where the overlapping occurs. Consider two images $I_1(x, y)$ and $I_2(x, y)$ with some overlapping region $R_{I_1, I_2}(x, y)$ between them. The average intensity value of a pixel located at $(i, j) \subseteq R$ would be described as:

$$b(i, j) = \frac{1}{2}[I_1(i, j) + I_2(i, j)] \tag{5.17}$$

Another popular option is alpha blending [97,98] used to weigh the intensity value of a pixel in the overlapping region given some kind of transparency metric. For 2D images, the alpha channel is an additional value between 0 and 1 that signifies the contribution of that image's corresponding pixel intensity in the overlapping region. Using the same images, $I_1(x, y)$ and $I_2(x, y)$ with some overlapping region $R_{I_1, I_2}(x, y)$ between them, we can define their respective alpha values as α_{I_1} and α_{I_2}. The alpha
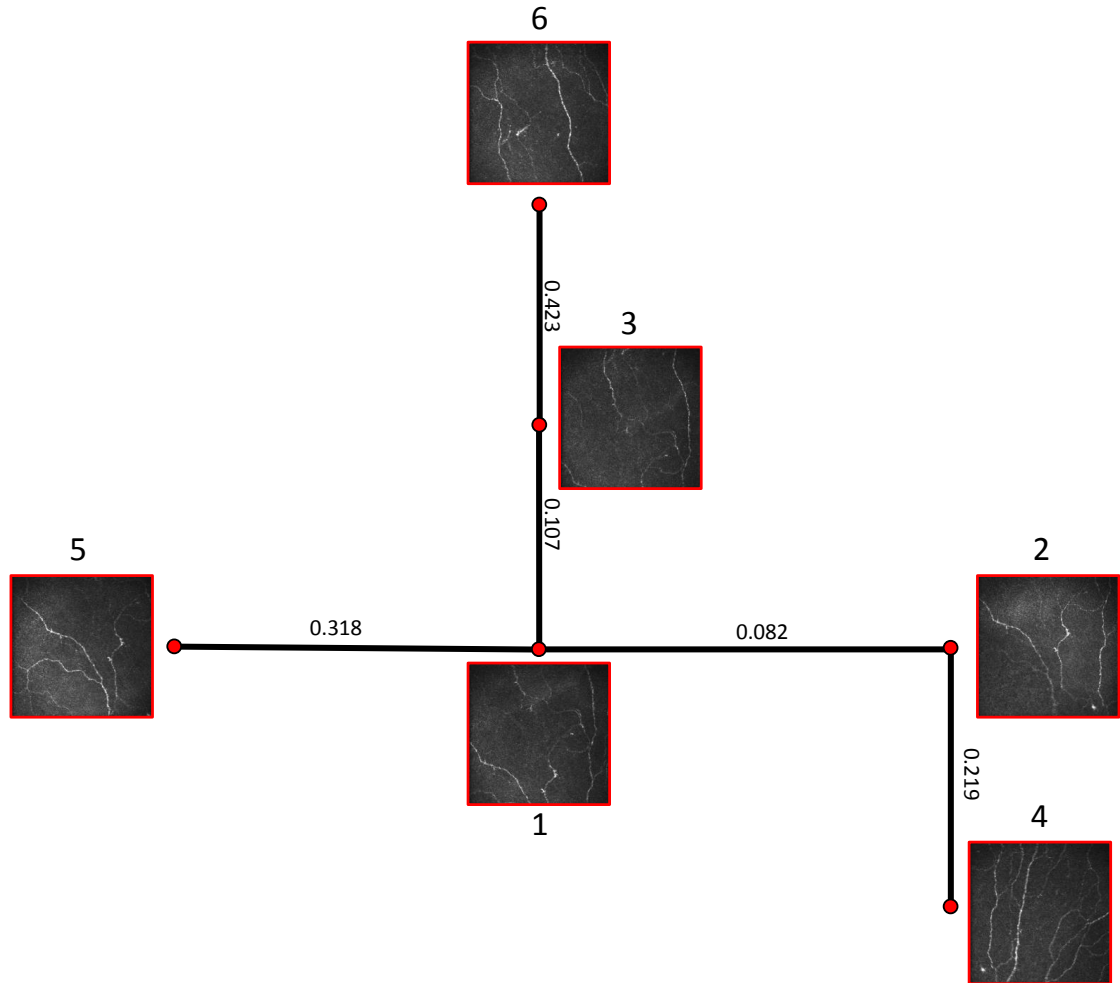
Figure 5.4: A subgraph derived from a data set of IVCM imagery. The nodes correspond to the images in the data set and the edges correspond to the edge weight. All images in the subgraph will be registered in a sequential order based on their edge weight. The number above each image shows the order in which it will come into play in the sequential registration pipeline.
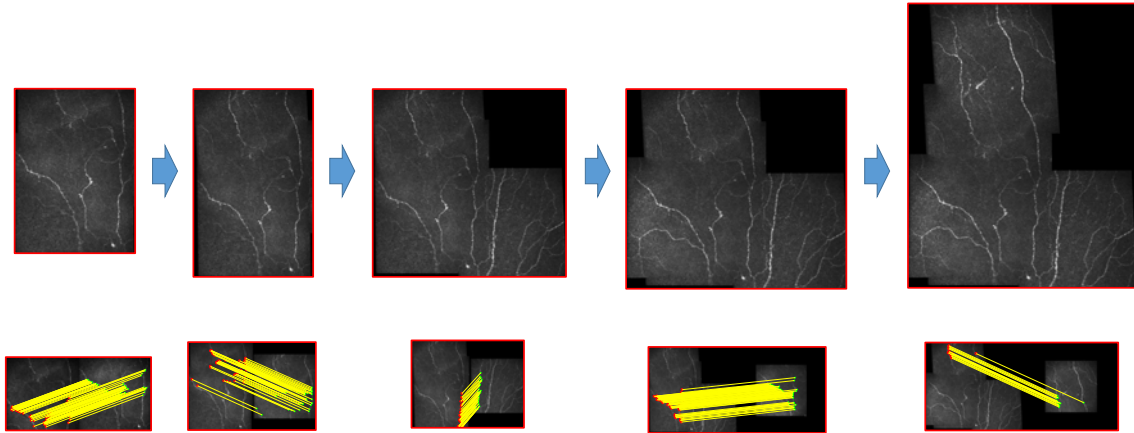
Figure 5.5: Iterative results of a sequential image registration pipeline of a subgraph after calculating the proper registration order.

blending for a pixel in the overlapping region is then defined as:

$$b(i,j) = \frac{I_1(i,j)\alpha_{I_1} + I_2(i,j)\alpha_{I_2}(1 - \alpha_{I_1})}{\alpha_{I_1} + \alpha_{I_2}(1 - \alpha_{I_1})} \tag{5.18}$$

The use of these blending metrics depends on the application and our method actually requires a modified mixture of the two. Averaging intensities for images that vary in illumination can cause artifacts especially when images have highly differentiating values at the edge of the images versus central regions like in IVCM imagery. Alpha blending gives us the ability to consider weighing the intensity in a region based on certain metric values of the image. For our method, we consider instead a blending scheme based on the distance of the pixel in the overlapping region with respect to the closest nonoverlapping pixel in each corresponding image. Once again if we consider images $I_1(x,y)$ and $I_2(x,y)$ with some overlapping region $R_{I_1,I_2}(x,y)$, we use a weighting scheme based on the distances to the pixel in question to a pixel in the nonoverlapping region from each image. That is, the closest Euclidean distance to a pixel that lies in the overlapping region from a pixel lying in image $I_1(x,y)$ that is not part of the overlapping region. For a pixel at location (i,j) in the overlapping

region we calculate this distance, normalize it, and define it as $d_{I_1}(i,j)$, and similarly, for image $I_2(x,y)$ the distance is defined as $d_{I_2}(i,j)$. The blended value at location (i,j) is then:

$$
\begin{aligned}
b(i,j) &= I_1(i,j)w_1(i,j) + I_2(i,j)w_2(i,j) \\
w_1(i,j) &= \frac{d_{I_1}(i,j)}{d_{I_1}(i,j) + d_{I_2}(i,j)} \\
w_2(i,j) &= \frac{d_{I_2}(i,j)}{d_{I_1}(i,j) + d_{I_2}(i,j)}
\end{aligned}
\tag{5.19}
$$

where we satisfy the condition that:

$$
w_1(i,j) = 1 - w_2(i,j)
\tag{5.20}
$$

Poletti et al. proposed a similar algorithm based on the same distance functions [79, 91] except they considered a form where the distance functions could be raised to a power, $d_{I_1}{}^n(i,j)$. In their works, the distance functions were squared while our work simply kept them as is. Examples of the blending results using the techniques previously described can be seen in Fig. 5.6. The artifacts of intensity averaging become apparent from the illumination difference in IVCM imagery which could further disrupt the extraction of structural information from the image. Alpha blending would be a great technique in and of itself if we want to consider a qualitative approach for evaluating the registration algorithm or for display purposes highlighting the registration region. If we wish to further quantitatively evaluate the structures in IVCM imagery it becomes apparent that our weighing scheme is the most appropriate choice for the matter.

It can be the case that during the initial pair-wise image registration, there may have been image pairs wherein a true overlap existed between these images but no connectivity was established between them in the graph due to their match metrics being too low on the global scale. Essentially, it's possible that image pairs showing
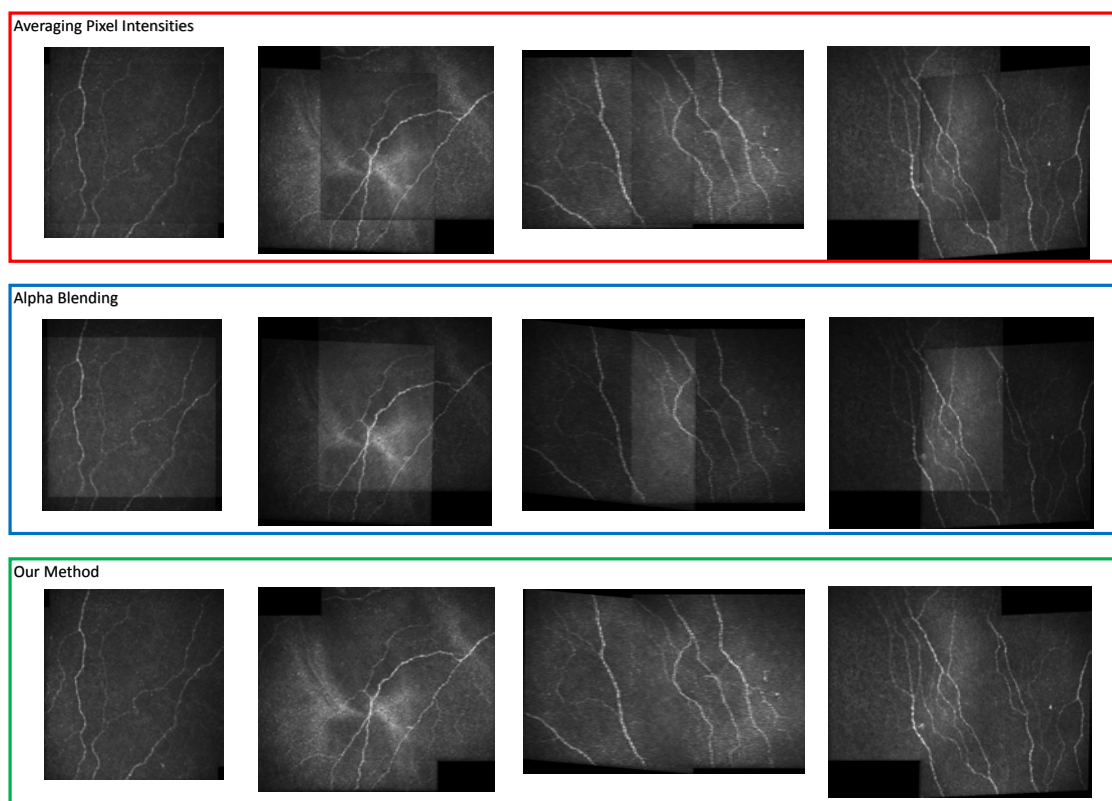
Figure 5.6: Examples of blending imagery after registration. Averaging can cause minor artifacts further disrupting quantitative analysis of the structures in IVCM imagery, alpha blending provides a qualitative option for evaluating registration results. Our method seamlessly blends the imagery for further quantitative analysis of the corneal structures.

weak connections in the initial pass can now have stronger connections with more matching points if either of these images is now part of a larger panorama. On a similar note, this can also help confirm the false positives found in the initial pass implying these images shouldn't be registered. We consider then, an iterative approach to the algorithm. We do the same pair-wise matching as before but this time using the resulting panoramas and any leftover images that had weak or no matches in the initial pass.

5.1.2 Segmenting Corneal Nerve Fibers from IVCM
Imagery of the Sub-Basal Nerve Plexus

Segmenting the corneal nerves poses many challenges that we need to overcome in order to achieve accurate segmentation results. The varying visual contrast and discontinuity of nerves due to the nature of their structure as they migrate and curve through the depth of the sub-basal nerve plexus is a hindrance on segmentation algorithms. In addition, applying pressure to the cornea from the apparatus can induce motion artifacts that also decrease segmentation accuracy. In Fig 5.7 we can see examples of notable IVCM imagery that could cause issues for standard segmentation techniques including illumination differences of the same structure and bends caused by the apparatus applying pressure to the cornea.

As discussed in Ch. 3, previous literature has shown that pixel-based machine learning algorithms are the most effective technique for dealing with these issues when segmenting single IVCM images. As such, to overcome the proposed challenges, we have adapted a pixel-based machine learning classification technique with features shown to have strong deterrence against the inherent noise in confocal imagery while providing good descriptions of elongated and tubular structures in the image. We develop the approach to be able to apply it to both segment single images and to the montage imagery we've developed in the previous section.

5.1.2.1 Candidate Pixel Selection

The corneal nerves make up a sparse portion of the pixels in IVCM imagery. This is something that we can take advantage of when considering pixel classification. Pushing for a brute force approach that uses all the pixels in each image makes for very large training and testing sets with very long training time. While this may be an ideal situation wherein we're able to consider all possible variations of an input-output relation, for clinical applications, the time and memory allocation requirements are just not feasible. In essence, we want to be able to construct a machine learning
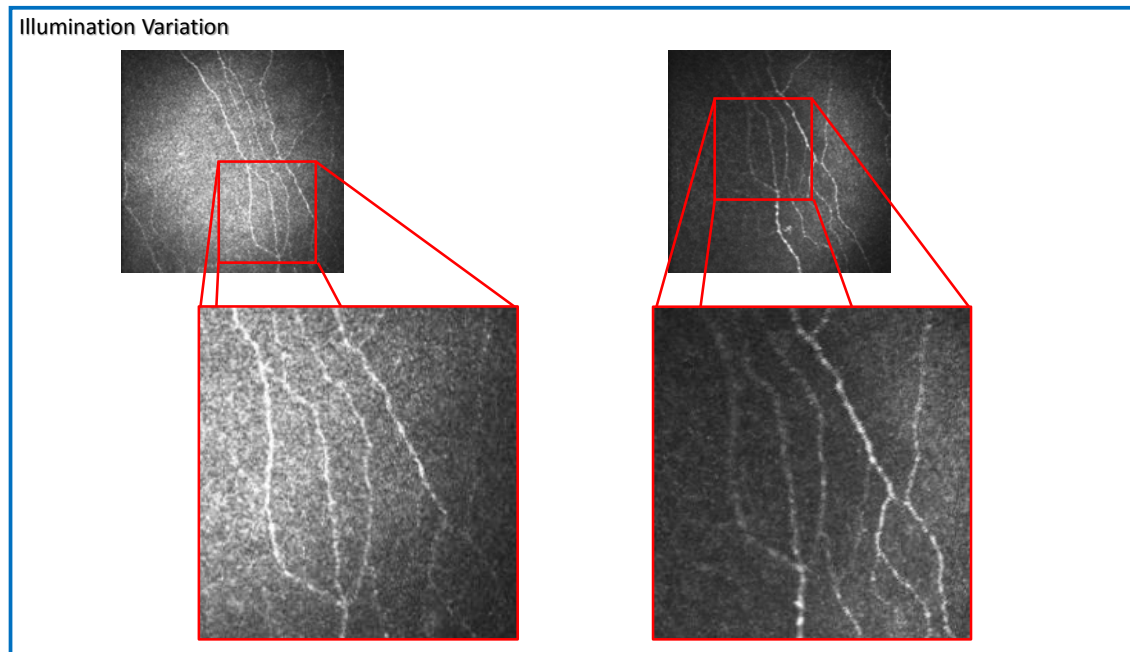
(a)
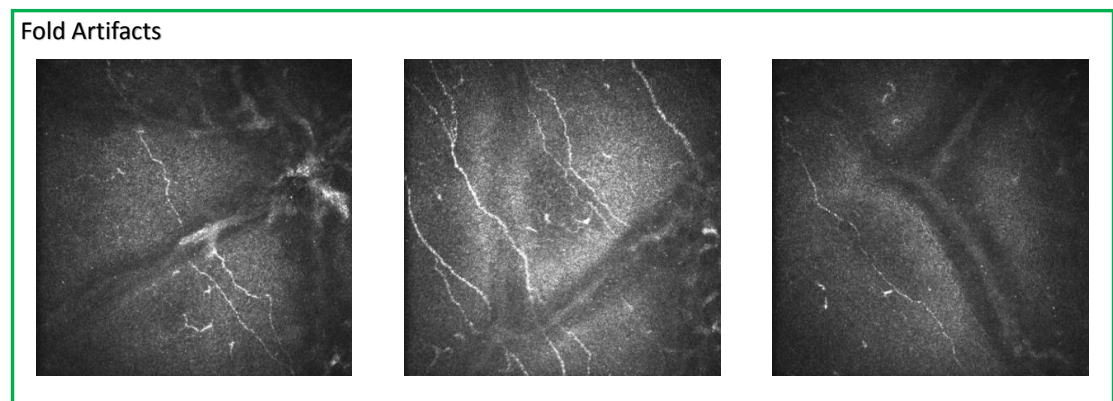
(b)

Figure 5.7: Examples of notable imagery that could cause issues for standard segmentation techniques. (a) Illumination differences found in the acquisition of IVCM imagery. The same structure can have vastly different intensity values due to the nonuniformity when adjusting the depth of the confocal microscope. (b) Pressure folds caused by pressing the confocal microscope up against the soft permeable tissue of the cornea.

scheme that is within the scope of clinical applications. This is why we consider an initializing step in our method before extracting features by exploiting the sparsity of the nerves to extract candidate pixels in each image. Morphological operators are used to describe a candidate set of pixels in which the majority are highly likely to be classified as nerves.

In Fig 5.7 we can see the impact of illumination difference on the imagery and to omit any complications that can arise from it we filter our input image using morphological top-hat filtering [96]. Top-hat filtering computes the morphological opening of the image (erosion of the image, followed by dilation on the erosion results) and then subtracts the result from the original image. The result is background equalization of the image. We continue by applying hysteresis thresholding to the image for its ability to use region information of pixels in the image that meet the high threshold value to determine if any pixels nearby are also candidate pixels based on the lower threshold and their vicinity to pixels that meet the higher threshold. Hysteresis thresholding often uses the results of Otsu's thresholding [99] as the higher threshold and half of that value for the lower threshold. That is what we implemented in our works as well. The results of this preprocessing step can be seen in Fig. 5.8.

5.1.2.2   Feature Extraction

The corneal nerves in the IVCM imagery of the sub-basal nerve plexus appear as elongated structures that can span across an entire image and even multiple images. If we consider these properties when developing our feature set, the notable filters that enhance these structures include log-Gabor filters [100–103] and multiscale vessel enhancement filters [104].

Log-Gabor filters are used in image processing because of their attractive 0 DC component, encompassing a relatively large bandwidth, and having a fairly uniform coverage in the frequency domain; this couples well with the size distribution of features in images oftentimes found to be logarithmic in scale [100,101]. In particular,
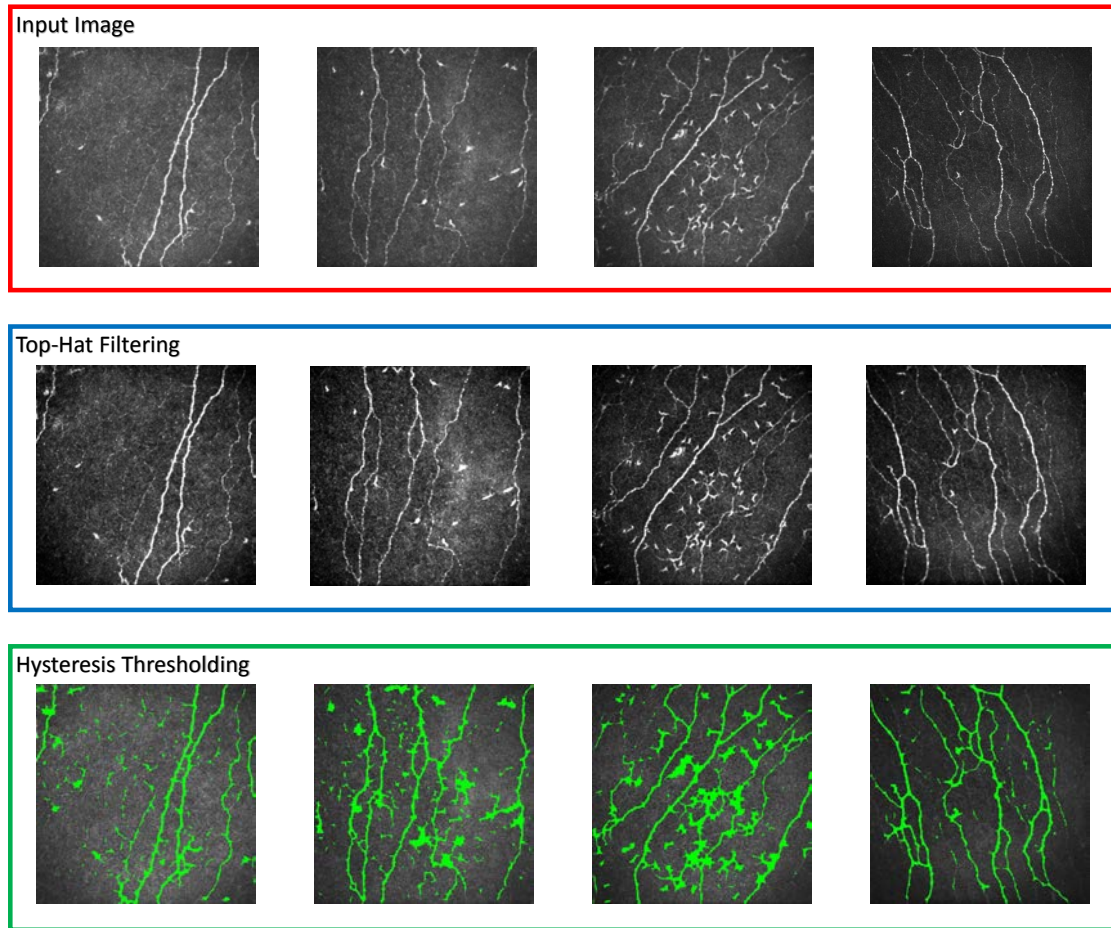
Figure 5.8: The preprocessing step we use to build a set of candidate pixels for classification using the machine learning approach.

they're well suited for local frequency estimation as well [102, 103]. Here we show an example of log-Gabor filters in the log-polar coordinate form in Fourier space (as Gaussians shifted from the origin):

$$G_{(s,t)}(\rho, \theta) = e^{-\frac{1}{2}(\frac{\rho - \rho_s}{\sigma_\rho})^2} e^{-\frac{1}{2}(\frac{\theta - \theta_{s,t}}{\sigma_\theta})^2} \tag{5.21}$$

where

$$\rho_s = log_2(n) - s \tag{5.22}$$

and

$$\theta_{s,t} = \begin{cases} \frac{\pi}{n_t}t & \text{if s is odd} \\ \\ \frac{\pi}{n_t}(t + \frac{1}{2}) & \text{if s is even} \end{cases} \tag{5.23}$$

where (ρ, θ) are the log_2 polar octave-scale coordinates, $(\rho_s, \theta_{s,t})$ are the filter centers, $(\sigma_\rho, \sigma_\theta)$ are the bandwidths in ρ and θ respectively with $n_s = 5$ as the number of multiresolution scales and $n_t = 8$ as the number of filter orientations wherein $s \in \{1, \cdots, n_s\}$ and $t \in \{1, \cdots, n_t\}$ [101]. Fig. 5.9 shows the results of a log-Gabor filter in our algorithm applied to an In-Vivo Confocal Microscopy image of the sub-basal nerve plexus at the aforementioned scales and orientations. For the purpose of example, we only show six orientations in the figure while our method uses eight total orientations.

In and of themselves, these responses provide only some of the structural information of the corneal nerves. To provide a better understanding of the underlying structure and orientation of the corneal nerves we consider the difference between the real and imaginary components of these results and extract the mean and standard deviation across all scales and orientations of this difference. That is, given an image $I(x, y)$, it will have a log-Gabor response $J_{n_s,n_t}(x, y)$. For a given scale n_s and orientation n_t we define $Ig_{n_s,n_t}(x, y)$ as:

$$Ig_{n_s,n_t}(x, y) = \Re(J_{n_s,n_t}(x, y)) - |\Im(J_{n_s,n_t}(x, y))| \tag{5.24}$$

(note, any negative values are set to 0) and we define $IG_m(x, y)$ and $IG_{std}(x, y)$ as the mean and standard deviation for the response of each pixel in Ig across all n_s and n_t. That is, for a given pixel intensity at x_i, y_i then
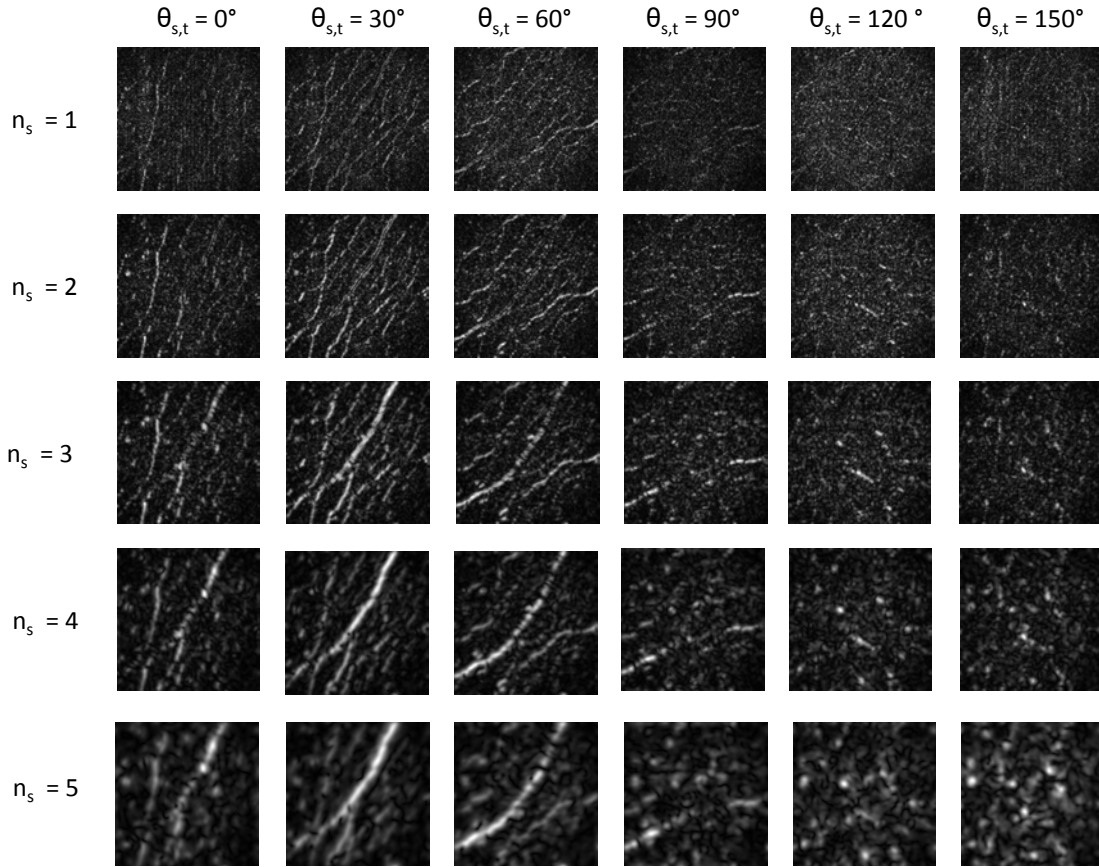
Figure 5.9: Results of a log-Gabor filter convolved with an IVCM image. Each row corresponds to a scale value n_s and each column corresponds to the various angle orientations $\theta_{s,t}$ as described in Eq. 5.21. For the purpose of example, we only show six orientations in this figure while our method used eight total orientations.

$$IG_m(x_i, y_i) = \frac{1}{n_s n_t} \sum_{i=1}^{n_s} \sum_{j=1}^{n_t} Ig_{n_{s_i}, n_{t_j}}(x_i, y_i) \tag{5.25}$$

and

$$IG_{std}(x_i, y_i) = \sqrt{\frac{1}{n_s n_t} \sum_{i=1}^{n_s} \sum_{j=1}^{n_t} (Ig_{n_{s_i}, n_{t_j}}(x_i, y_i) - IG_m(x_i, y_i))^2} \tag{5.26}$$

An example of $IG_m(x, y)$ and $IG_{std}(x, y)$ for a few images can be seen in Fig. 5.10

Other elongated structures found in medical imaging are the veins and arteries of
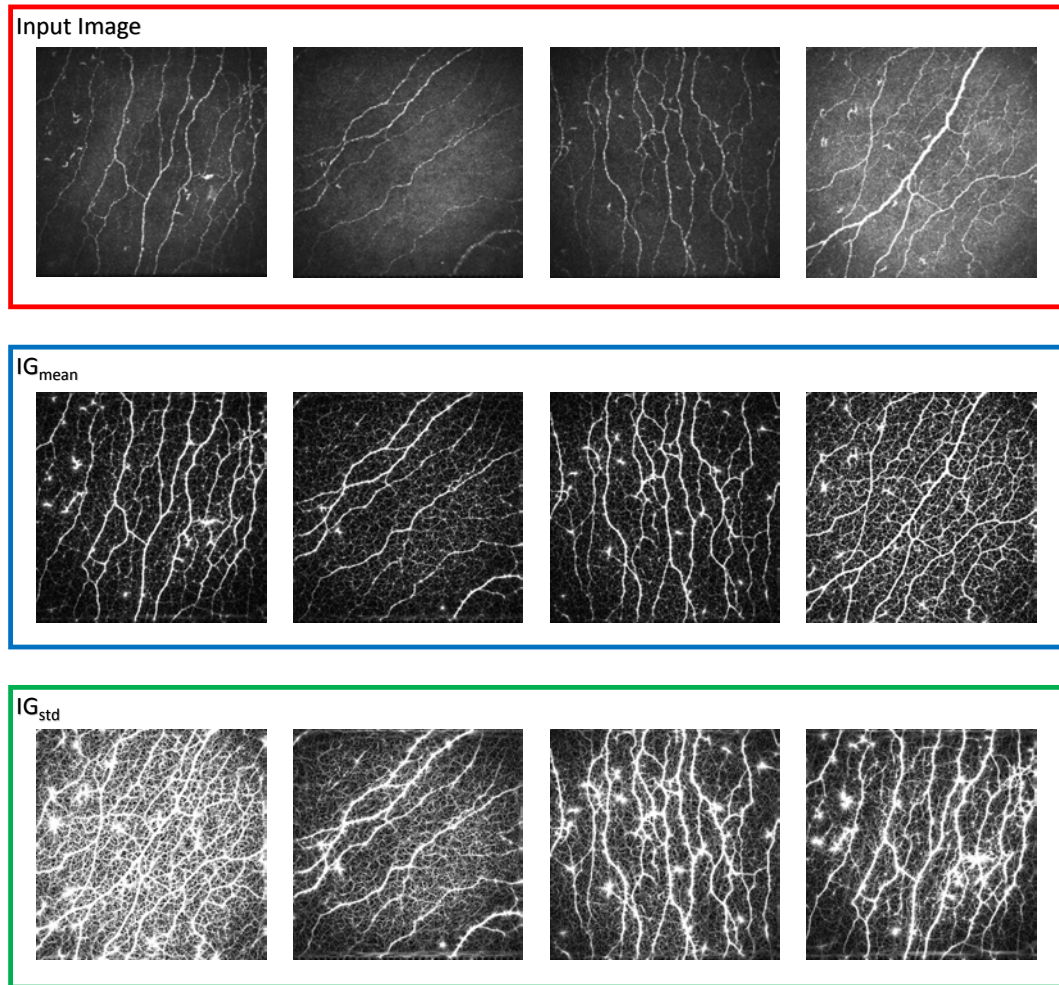
Figure 5.10: Results of the mean and standard deviation of the difference between the real and imaginary parts of the log-Gabor filter response to an image at various scales and orientations defined as $IG_m(x, y)$ and $IG_{std}(x, y)$ respectively.

Table 5.1: Eigenvalues of the Hessian [104] as they
pertain to the shape description of elongated
structures in 2D where $|\lambda_1| \leq |\lambda_2|$.

λ_1	λ_2	Descriptor
noisy	noisy	noisy, no specific direction
small	large(-)	tubular structure (bright)
small	large(+)	tubular structure (dark)
large(-)	large(-)	blob-like structure (bright)
large(+)	large(+)	blob-like structure (dark)

the peripheral vascular system. For these structures, Frangi et al. [104] developed a
multiscale local structure analysis of peripheral vascular images based on the eigen-
values of the Hessian of the image. For this purpose of our works, we will summarize
the work from Frangi as it applies to 2D images of the corneal nerves. Let us first
consider a straightforward description based on the eigenvalues of the Hessian matrix
and how their values describe the structures in an image by referring to Table. 5.1.

Here we've listed the eigenvalues in ascending order, such that $|\lambda_1| \leq |\lambda_2|$. Noisy
eigenvalues correspond to no specific directions meaning there are no tubular struc-
tures present. If λ_1 is small and λ_2 is large we can expect a tubular structure; the
structure will appear bright if λ_2 is negative or dark if λ_2 is positive. In the case where
both eigenvalues are large and positive, dark blob-like structures are expected to be
present in the image whereas if the large eigenvalues are negative, bright blob-like
structures are present. Frangi et al. describe the vesselness measure of a pixel as the
following:

$$V_o(s) = \begin{cases} 0 & \text{if } \lambda_2 > 0, \\ e^{-\frac{R_\beta^2}{2\beta^2}}\left(1 - e^{-\frac{S^2}{2c^2}}\right) & \text{otherwise} \end{cases} \quad (5.27)$$

with $R_\beta = \lambda_1/\lambda_2$ defined as the blobness descriptor ratio evident from possible eigen-
value variations summarized in Table. 5.1 and the second order "structureness" S is
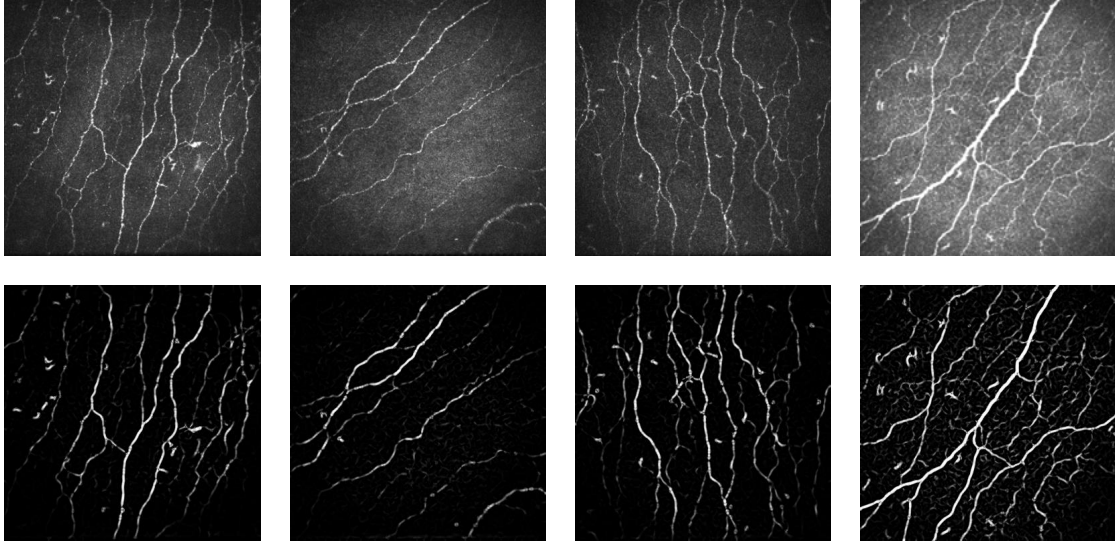
Figure 5.11: Results of applying a Frangi vesselness detection filter to various single IVCM images. The top row corresponds to the normal image and the bottom row is their Frangi vesselness filter responses as described in Eq. 5.27.

the Frobenius matrix norm for the Hessian of the image:

$$S = ||Hessian(I_{(x,y)})||_F = \sqrt{\sum_{j \leq 2} \lambda_j{}^2} \qquad (5.28)$$

for an empirically fixed $\beta = 0.5$ and c set as half the value of the maximum Hessian norm. An example of the Frangi vesselness response extracted from corneal images of the sub-basal nerve plexus can be seen in Fig. 5.11.

5.1.2.3 Classification

For the machine learning component of our algorithm, we used a support vector machine (SVM) with a radial basis kernel to support the multiple dimensions of the feature space. SVMs are a popular binary classification algorithm for separating two data classes first introduced by Cortes et al. [105]. In essence, SVMs find an optimal hyperplane in the feature dimension that best separates the classes. If it is the case that a hyperplane does not exist such that it can completely separate all the data

the SVM incorporates a soft margin on the hyperplane applying a penalty to data points depending on their proximity to the hyperplane. The primal formulation for the hyperplane is described in the works of Friedman et al. [106] and Shaw-Taylor et al. [107] and summarized here for the purpose of inclusion:

$$f(x) = x'\beta + b = 0 \tag{5.29}$$

where $\beta \in R^d$ and b is a real number. We define the separation problem in such a way that we want the hyperplane that creates the best decision boundary for our classification problem [106]. We then find β and b that minimize $||\beta||$ s.t. for all data points (x_j, y_j):

$$y_j f(x_j) \geq 1 \tag{5.30}$$

The support vectors then are the x_j components of the data that lie on the boundary for which $y_j f(x_j) = 1$. We can propose this equivalently as minimizing $||\beta||$. Finding the optimal solution $(\hat{\beta}, \hat{b})$ enables us to classify a feature vector z to determine the classification using:

$$class(z) = sign(z'\hat{\beta} + \hat{b}) = sign(\hat{f}(z)) \tag{5.31}$$

The feature space is then composed of the following features, and specifically derived for the candidate pixels depicted in Fig 5.8:

1. Intensity value from the IVCM imagery.

2. The mean of the difference between the real and imaginary components of the log-Gabor filter bank across all scales and orientations (5.10)

3. The standard deviation of the response of the difference between the real and imaginary components of the log-Gabor filter bank across all scales and orien-

tations (5.10)

4. The Frangi vesselness filter probability map (5.11)

The feature vectors are fed into the SVM classifier and the output of the SVM classifier is a probability map between 0 and 1 wherein values closer to 1 indicate a higher chance the pixel is a nerve. Once the images have been segmented, an optimal operating point (OOP) for thresholding can be derived from the ROC curve for a given sensitivity and specificity requirement. The optimal operating point is often chosen as the point on the curve closest to the point [0, 1] in the True Positive Rate/False Positive Rate coordinate system. This is also the point chosen for our results.

5.1.2.4 Post-Processing

In some of the IVCM imagery, dendritic cells can make an appearance in the sub-basal nerve plexus (Fig. 5.12). To omit them from our segmentation we also include a two-step post-processing procedure. Consisting of a quick first pass of removing any sporadic false positives through connected component analysis by removing any regions connected with five or fewer pixels. This can get rid of some portion of the dendritic cells without affecting the nerve segmentation. While increasing the thresholding for the minimum required number of connected components would remove more dendritic cells it would also affect pixels correctly classified as nerves. Instead, the second part of our post-processing step considers region property measurements. We measure the perimeter and area of the regions classified as nerves and obtain a roundness metric defined as $m = 4\pi \frac{area}{perimeter^2}$. A relatively high metric value corresponds to a round or blob object (where a perfect circle would have a roundness value of 1). A threshold value for the roundness metric is chosen so as to sustain a reasonable trade-off between removing dendritic cells and minimally affecting the pixels correctly identified as nerves. An example of the boundaries and metric values
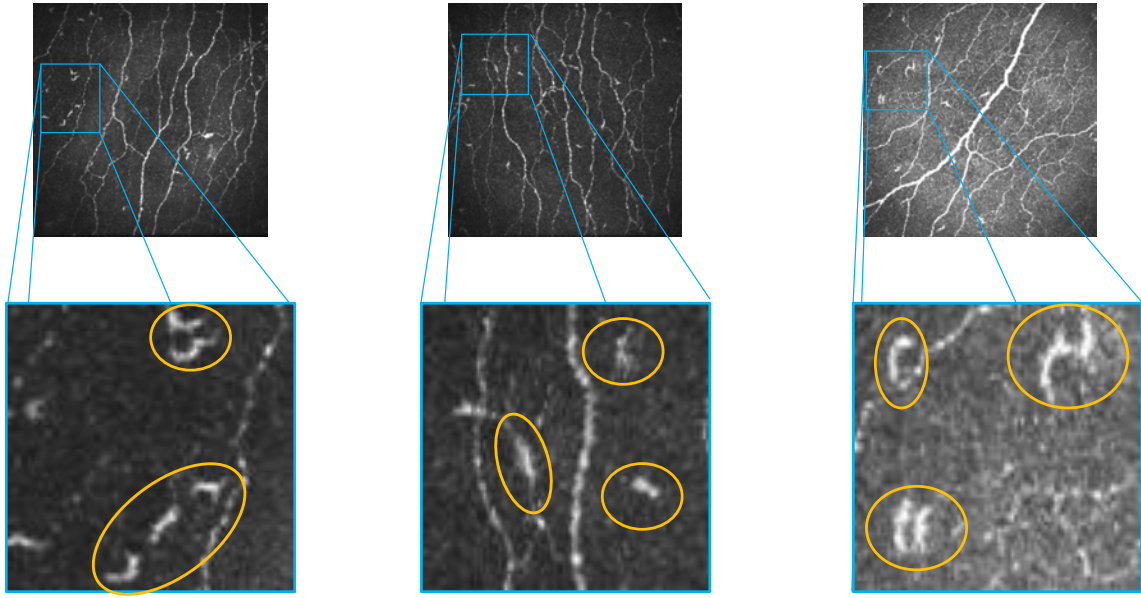
Figure 5.12: Dendritic cells that appear in some portions of the IVCM imagery, often times sharing similar intensity profiles to the corneal nerves.

obtains in the IVCM imagery can be seen in Fig. 5.13.

5.2   Experimental Methods

5.2.1   Data and Reference Standard

The dataset provided included 2D in-vivo confocal microscopy images of the human sub-basal nerve plexus acquired using the Heidelberg Retina Tomographer and Rostock Cornea Module (Heidelberg, Germany) at the University of Iowa. Each IVCM image represented a coronal section of the cornea that was 400 μm × 400 μm (384×384 pixels) in physical dimensions in the x-direction and y-direction respectively. The images were acquired at an 8-bit grayscale bit depth and at a physical depth of around 62 μm varying marginally to encompass areas where the corneal nerve fiber layers were most prevalent on a patient-by-patient basis. A disposable sterile cap made of polymethylmethacrylate (Tomo-Cap; Heidelberg Engineering) was filled with a layer of hypromellose 0.3% gel (GenTeal; Alcon, Forth Worth, TX, USA) and
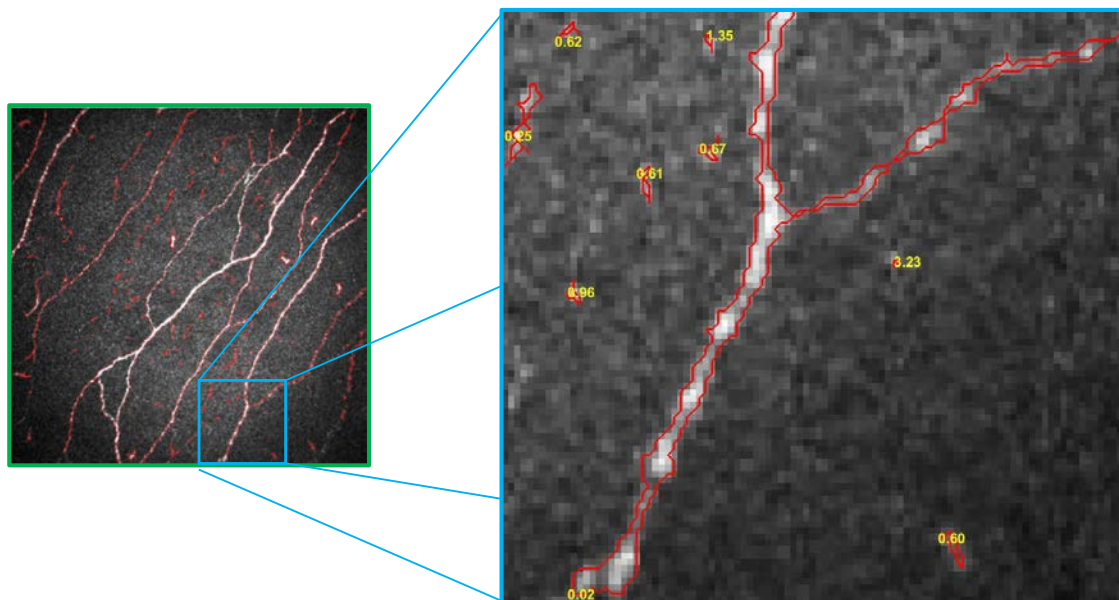
Figure 5.13: The computed boundaries and regional metric values for the post-processing step of removing dendritic cells in the IVCM imagery.

was mounted on the corneal module. Topical anesthesia with 0.5% proparacaine hydrochloride (Alcon) and a drop of hypromellose 0.3% gel was applied to both eyes. An additional layer of gel was placed on the outside tip of the Tomo-Cap for optimal optical coupling. The Corneal Module was then adjusted until the gel made contact with the surface of the cornea.

The imagery available for evaluating the montaging algorithm was comprised of four data sets from four normals, consisting of 84-221 IVCM images per data set. The imaging protocol from this data set was designed specifically in order to evaluate the montaging algorithm. The difficulty came in establishing a protocol the photographer could consistently execute where images could be acquired so as to provide as much overlap as possible between sequential images. This proved difficult to establish resulting in an overall smaller data set available for evaluation of the montaging algorithm. Reference standards for the registration were acquired using point-based

manual registration from two observers.

To evaluate the segmentation algorithm two images were chosen from each of 26 subjects. The data included images from 10 normals, 8 diabetics, and 8 patients with trigeminal nerve lesions. One image from the left eye and one from the right eye were chosen for a total of 52 IVCM images. The images were manually chosen based on how well they displayed the sub-basal nerve plexus. The reference standard for the segmentation was acquired by manually tracing the 52 images.

The registration algorithm and segmentation algorithm were run on a Windows 7 64-bit operating system with an Intel Xeon E5 1620 (4 cores) at 3.7Ghz and 64GB of RAM.

5.2.2   Experiments

To evaluate the accuracy of the registration, manual registration was performed on image pairs and compared to the automated results. The evaluation consisted of manually registering 101 unique image pairs (from 202 images) by two different observers. The observers chose a set of at least three corresponding points between image pairs and an affine transformation matrix $T_m(x, y)$ was computed based on the manually chosen points. In addition, an affine transformation matrix $T_a(x, y)$ was computed based on the results of the automated registration algorithm. A forward transformation was applied to the points on the moving images using $T_m(x, y)$ and $T_a(x, y)$. Applying the forward transforms from $T_m(x, y)$ and $T_a(x, y)$ gave us the points defined as (X_m, Y_m) and (X_a, Y_a) respectively. The mean distance between all points in (X_m, Y_m) and (X_a, Y_a) was computed to evaluate how close the automated registration was when compared to manual registration. Similarly for a pair of images given $T_{m1}(x, y)$ by observer 1 and $T_{m2}(x, y)$ by observer 2 and the points defined as (X_{m1}, Y_{m1}) and (X_{m2}, Y_{m2}) respectively we computed the mean distance between all points in (X_{m1}, Y_{m1}) and (X_{m2}, Y_{m2}) to determine inter-observer variation. Fig. 5.14 illustrated the described points.
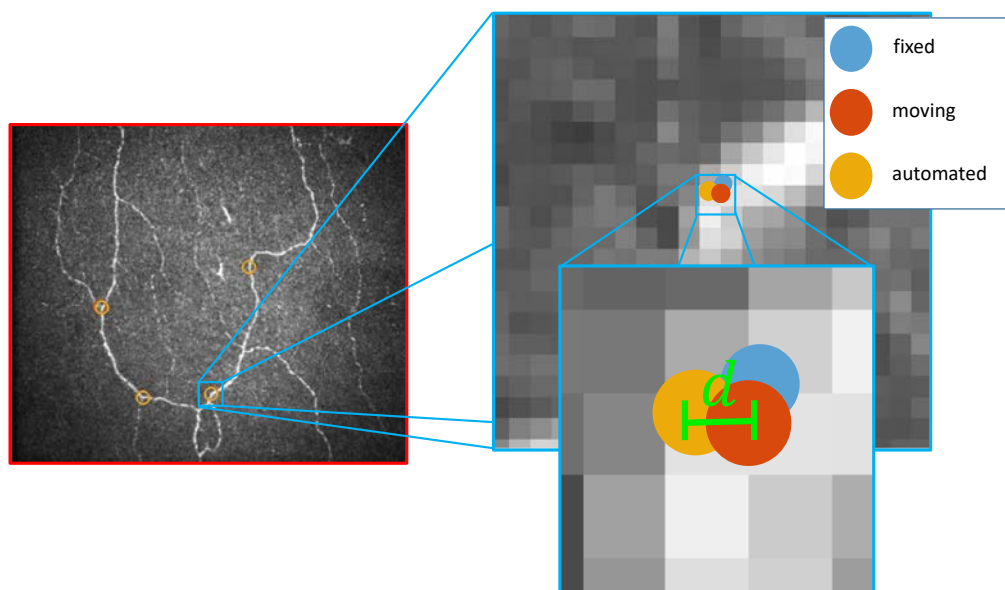
Figure 5.14: An example of fixed points and their corresponding moving image points transformed to fixed image space using the manual transformation and the automated registration transformation. The distance between the fixed image point and the point computed via the automated registration transformation is the metric considered for evaluation of the registration error.

To evaluate the automated segmentation algorithm we considered the use of manually segmented IVCM images. The images came from 26 patients of various backgrounds with two images coming from each patient. The patient groups included 10 normals, 8 diabetics, and 8 patients with trigeminal nerve lesions. Two images were acquired from each subject, one corresponding to each eye, for a total of 52 images. A leave-one-image-out approach was implemented for testing and training the machine learning component. The manually segmented images were used to create label images such that a pixel with a value of 0 in the label image corresponded to background pixels in the IVCM imagery and similarly a pixel with a value of 1 corresponded to nerve pixels in the IVCM imagery. For a single iteration of the leave-one-image-out approach, we used the set of candidate pixels (as shown in Fig 5.8) from one of the

images for testing and used a portion of the candidate pixels from the other remaining 51 images for training. For a single iteration of the leave-one-image-out scheme, we would then have n number of training samples and M number of testing samples. Given the sparsity of nerve pixels in IVCM imagery, we considered an even distribution of nerve and background pixels for the training. That is, if from the M-number of testing samples, only m-number are labeled as nerve pixels, we also include a randomly selected m-number of background pixels for a total of $2m$-number of evenly distributed testing samples. This allowed for a more comparable distribution of nerve pixels for training. An ROC curve was computed from the outputs of the leave-one-image-out approach to compare the performance of the machine learning algorithm versus simply thresholding the described features wherein we considered specificity, sensitivity, and accuracy.

5.3   Results

Examples of incorporating the image stitching and segmentation algorithms on the data sets can be seen in Fig. 5.15.

It should be noted that of the 101 image pairs that were manually registered, the automated approach failed on one of them. The algorithm found matching features between the images but the points corresponding to the matching features did not correspond with each other resulting in an incorrect registration. As such, it was omitted from evaluation leaving 100 image pairs for the final registration error evaluation. The accuracy of automated registration versus manual registration is reported in Table 5.2. The inter-observer variability was computed and found to be 2.36 ± 3.65 μm between observers. In addition, overall registration error between the manually transformed points and their automated counterparts was 2.13 ± 1.10 μm. Statistical analysis using a paired t-test showed statistically smaller errors when using the automated method versus using manual registration techniques ($p < 0.05$). These findings would have us consider the fact that the automated registration finds
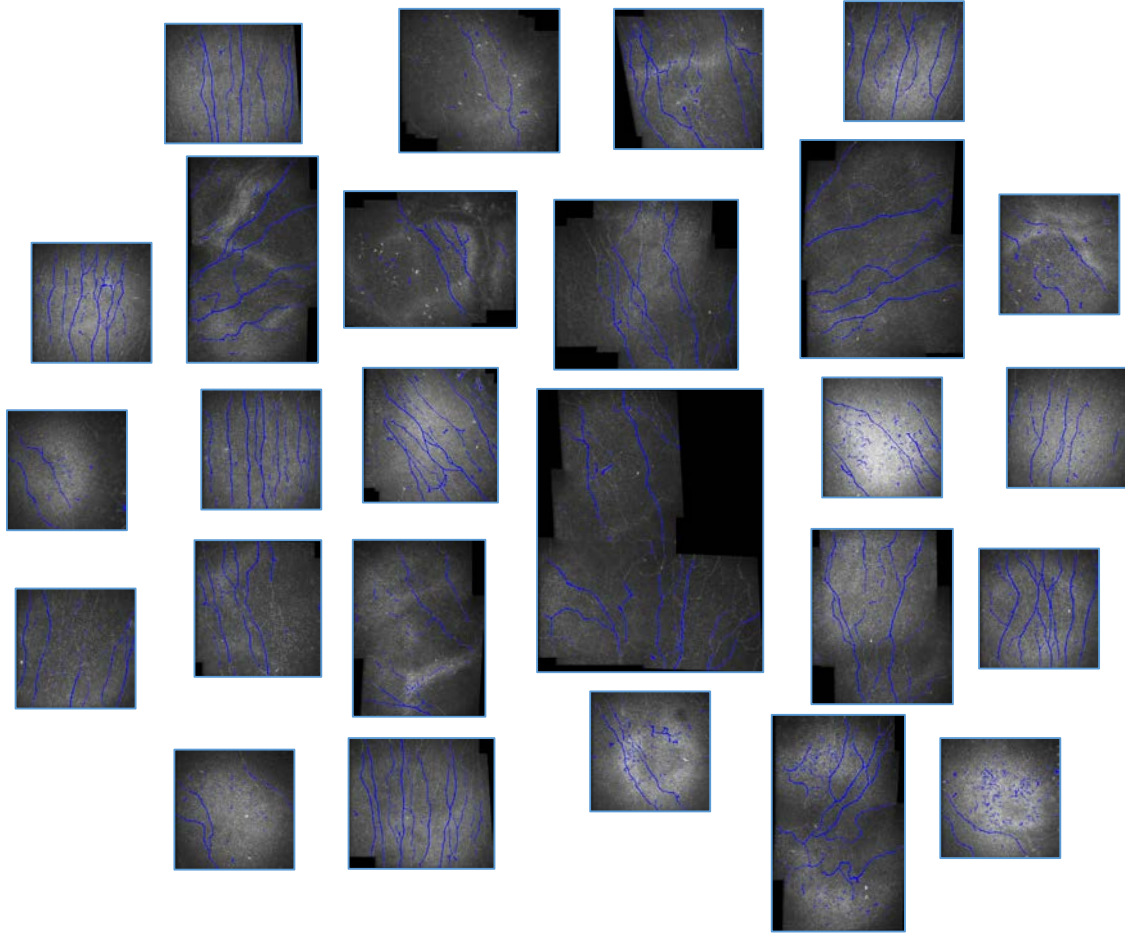
Figure 5.15: Panoramas developed from the registration algorithm along with single images, all segmented via our machine learning approach.

many more matching points between images versus manual methods to find the most accurate registration possible. We cannot conclude that it would be more accurate than manual methods unless further analysis introduced manual methods with an equivalent number of points as the automated method. Given a manual method with an equivalent number of corresponding points between images chosen by the observers we would be able to perform RANSAC analysis on these points for a more accurate manual registration as well.

The ROC curve for the segmentation algorithm is shown in Fig. 5.16

Table 5.2: Quantitative evaluation of the registration error as the mean distance between the fixed image points and the moving points after applying the transform matrix found in the manual and automated registration.

		Observer 1	Observer 2	Combined
Automated Results	Pixels	2.38 ± 1.18	2.07 ± 1.21	2.22 ± 1.15
	Microns	2.27 ± 1.13	1.98 ± 1.16	2.13 ± 1.10
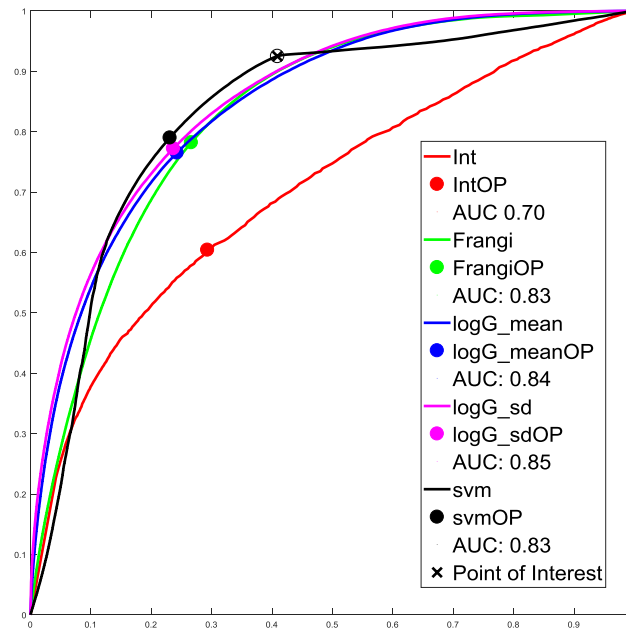
Figure 5.16: The ROC curve of the machine learning segmentation algorithm. Also depicted are the curves of the machine learning algorithm using single features and their corresponding AUC values.

along with the optimal operating point. The optimal operating point (OOP) is defined as the point on the curve closest to the point $[0, 1]$ in the $TruePositiveRate$ $(TPR)/FalsePositiveRate$ (FPR) coordinate system. That is, the OOP is the point at which costs of misclassifying nerve and not-nerve cases are equal. At this threshold value, the sensitivity is 0.79 and the specificity is 0.75 and the accuracy is 77.41%. Another point of interest on the ROC curve also considered is the point at which the classifier reached the sensitivity value of 0.93, more so because it reaches it at a lower FPR when compared to the thresholding of single features. Here, the specificity is 0.59 and the accuracy is 67.05%.

5.4 Discussion and Conclusion

In this chapter, we developed an algorithm that could successfully create panoramas of 2D in-vivo confocal microscopy images depicting the sub-basal nerve plexus. In addition, we developed a method to segment the corneal nerves found in these images for further quantitative analysis. The registration approach was developed using four data sets of IVCM imagery containing between 84-221 IVCM images per set with evaluations of registration applied on 101 image pairs. The segmentation approach was developed using 52 IVCM single images and was evaluated based on the sensitivity, specificity, and accuracy of the machine learning output.

Results showed the method's ability to effectively detect overlapping images in the data set and proved to be an effective method for accurate registration providing a time-efficient alternative to manual registration. The algorithm showed an accuracy of 1.16 ± 0.60 μm in the distance between manual and automated points when transforming the moving image to the fixed image space for image pairs. It also provided promising results for finding panoramas in the data sets without knowledge of image order *a prior* resulting in increased regions of interest for in-vivo confocal microscopy images. In addition, the segmentation algorithm provided an alternative for manual segmentation with the ability to tune the algorithm for variation in sensitivity and

accuracy based on the application.

Our method differs when compared to prior works in that it does not make assumptions on image order and does not require any modifications to the existing imaging protocols or imaging hardware/software interface. The approach can have limitations if there is not enough overlap between matching images in a data set such that the algorithm will fail to find any corresponding points for registration. While inherently independent of variations in illumination, the algorithm may also fail if extremities in illumination exist. In addition, while the current segmentation algorithm uses a viable scheme for pixel classification, it still has room for improvements in feature selection and execution time.

In summary, we showed strong evidence of an automated registration and segmentation algorithm, finding overlapping imagery in data sets containing over hundreds of images and with the ability to detect corneal structures in the images. The method proved effective in imagery regardless of subject backgrounds. It can be considered as the basis for an off-line unsupervised method for quantitative analysis of corneal structures in confocal microscopy imagery. We believe it will prove useful for further analysis of the impact ophthalmic diseases may have on the corneal structures.

CHAPTER 6
DETERMINING CORRELATIONS IN STRUCTURAL MEASUREMENTS OF MULTIMODAL CORNEAL IMAGERY OF OPHTHALMIC DISEASES KNOWN TO IMPACT CORNEAL STRUCTURES

6.1   Methods

The methodology in this chapter is divided into three core components. In order to extract structural measurements to perform statistical analysis, we first explore the options available from the segmentation results in previous chapters. At our disposal, we have the segmentation results that can be produced by our first method. These include the surfaces in 3D AS-OCT volumes of the cornea depicting the boundaries between the layers. These can be used to analyze the thicknesses and volume or area between boundaries to determine any differences across the various patient groups. We also have the results stemming from our second method depicting the segmentation of corneal nerves identified in in-vivo confocal microscopy images of the sub-basal nerve plexus. The distinct appearance of the nerves allows us to consider descriptive characteristics like length, density, or tortuosity. With relevant measurements in place, we can acquire the data most applicable for further analysis and apply these algorithms to said data.

6.1.1   Establish Structural Measurements from Corneal
Segmentations of 3D AS-OCT Volumes

In this section, we discuss the structural measurements we extracted from the segmentation of the AS-OCT volumes. When using AS-OCT to manually evaluate corneal thicknesses, manual measurements are taken at the center and on a single slice but AS-OCT images encapsulate a 3D view of the cornea. If we couple this 3D information with the segmentation results developed in Ch. 4 we can consider two other possible approaches for measuring corneal layers. We can measure thicknesses across multiple locations in 2D and 3D or even measure entire regions that encompass

corneal layers. Three specific boundaries on thickness measurements were considered for epithelial, stromal, and total thicknesses as shown in Fig. 6.1. Multiple points were also chosen for location-specific measurements. One point was a central area, two were in a peripheral area, and two outer boundary points which can be seen in Fig. 6.2. The peripheral and outer boundaries points were chosen at equidistant locations to the left and right of the center point of the cornea. This helps in the case where the outer boundaries of the image are not exactly equidistant from the center of the cornea which can often be the case due to patient movement of the eye. The global thickness measurements encompass entire regions in each B-scan that are depicted in Fig. 6.3 and the respective regions in each slice are shown in Fig. 6.4. The measurement we compute from these global measurements is the area in each B-scan, followed by a mean area across all available B-scans. The reason we used this measurement instead of measuring the entire volume is that some of the data had missing or corrupt B-scans in the volumes which can result in biased comparisons when it comes to analyzing volume measurements for statistical significance.

6.1.2 Extract Structural Measurements from Corneal Nerve Fibers Segmentations of IVCM Imagery

The methods in previous chapters dealing with in-vivo confocal microscopy have allowed us to consider further analysis on the corneal fibers present in the imagery. Given the relation between ophthalmic diseases and how they affect corneal nerve fibers, one natural response is to analyze how the inherent shapes of the corneal nerves are impacted. For this, we consider investigating the shape and geometric features of the corneal nerves extracted from the IVCM imagery. For our works we extract the following structural measurements:

1. **Nerve Density:** The nerve density can help describe the overall distribution of the nerves in the imagery. We believe it to be of considerable importance given a significance has already been established between nerve density and severity
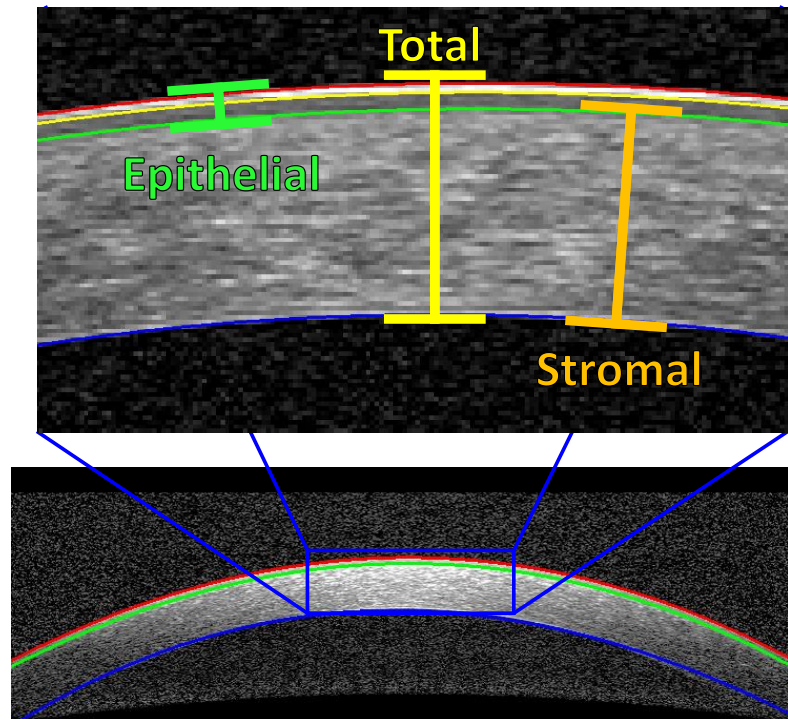
Figure 6.1: The corneal thickness measurements of significant interest. The epithelial thickness is shown in green with the stromal thickness and total thickness measurements shown in orange and yellow respectively.
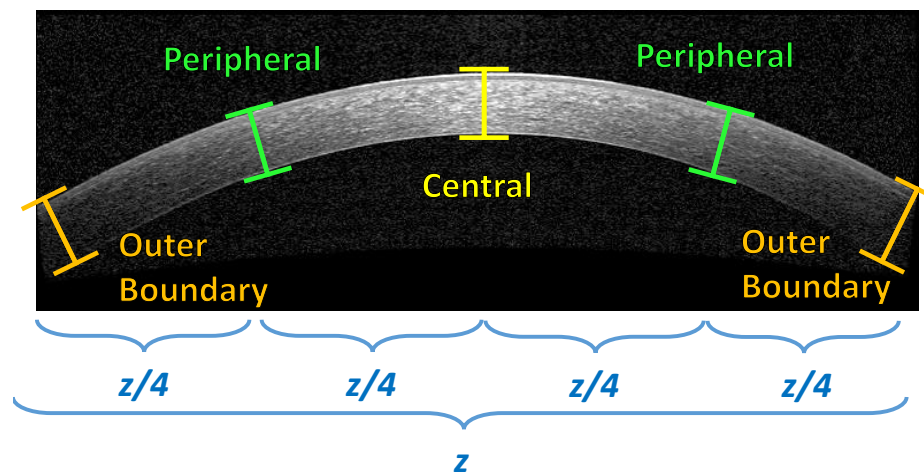
Figure 6.2: The specific points of interest where we measure for further analysis of corneal thickness measurements. The highest point on the image is considered as the central region with the peripheral and outer boundaries taken by traversing equidistantly from the central region outwards.
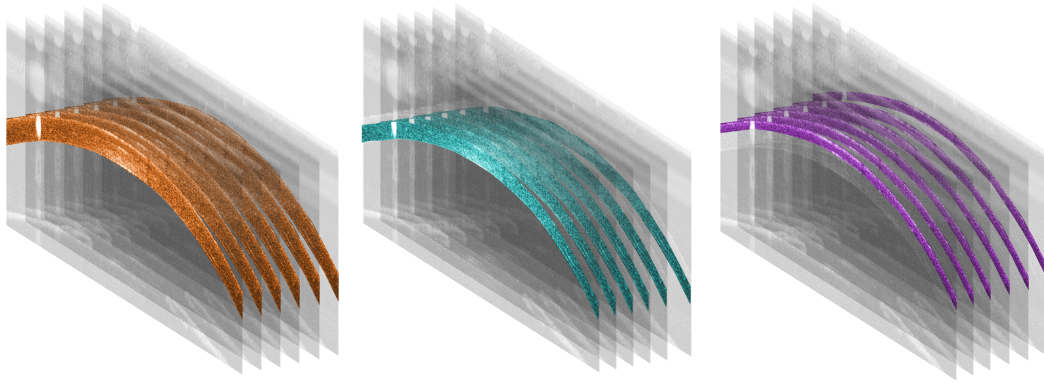
Figure 6.3: Region encompassing global total corneal thickness measurements shown in orange (left), region encompassing global stromal thickness measurements in cyan (center), and region encompassing global epithelial thickness measurements in purple (right) where we take global measurements.

of diabetic neuropathy [11]. It is only logical we would want to further consider nerve density for other diseases. To measure the corneal nerve density in IVCM imagery we apply the segmentation approach described in Ch. 5 to extract the corneal nerves. Then we compute the density as the number of pixels in the image classified as nerves over the total number of pixels in the image as:

$$Density_{nerves} = \frac{\sum NervePixels}{ImageArea} \tag{6.1}$$

2. **Mean Nerve Length & Max Nerve Length:** The length of the nerves in the imagery can aid in better illustrating the overall composition of the corneal nerves so as to determine how the nerves contribute to the nerve density computed prior. For example, given a large density measure, the nerve length can help illustrate whether the density measurements come from a large number of short nerves or from a short number of long nerves. To calculate the nerve length of each nerve in the image we first skeletonize the segmentation and find the ends of the nerve (including branch ends) exhibiting the
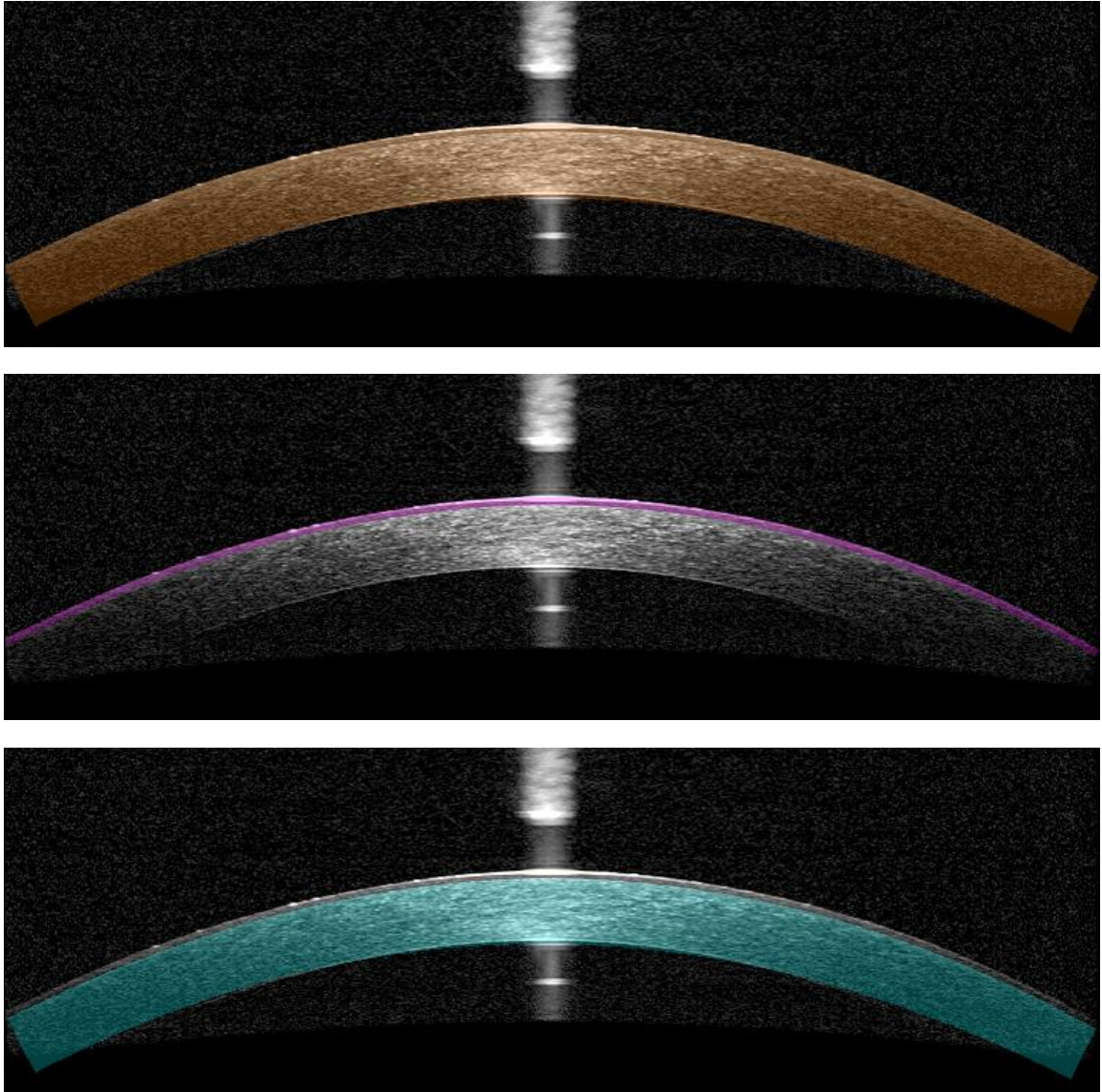
Figure 6.4: Region encompassing total corneal area in a single slice shown in orange (top), region encompassing corneal epithelial area in purple (middle) and region encompassing corneal stromal area in cyan (bottom).

largest Euclidean distance between them. Then we compute the nerve length as the path on the skeleton we have to travel from one endpoint to reach the other endpoint. Given these endpoints at coordinates (x_{end_1}, y_{end_1}) and (x_{end_2}, y_{end_2}) the path on the skeleton consists of a group of points described as $[(x_{end_1}, y_{end_1}), \ldots, (x_{i-1}, y_{i-1}), (x_i, y_i), (x_{i+1}, y_{i+1}), \ldots, (x_{end_2}, y_{end_2})]$. The nerve length is computed by summing the individual Euclidean distances between adjacent pixels on the skeleton path from one endpoint to the other. As such, the distance between adjacent points on the skeleton path is computed as:

$$dist_{i,i+1} = \sqrt{(x_{i+1} - x_i)^2 + (y_{i+1} - y_i)^2} \tag{6.2}$$

Given a total n pixels on the path between endpoints (including the starting and endpoints) the nerve length is then computed as a sum of these individual distances as:

$$nerve_{length} = \sum_{i}^{n-1} dist_{i,i+1} \tag{6.3}$$

We compute the length of all the nerves found in an image as well as the longest nerve in the image. These measurements are then averaged across all the images from all the sessions and visits for each patient.

3. **Tortuosity:** The nerves in the sub-basal nerve plexus can exhibit multiple variations of contorted shapes. These shapes have been known to vary throughout the sub-basal nerve plexus and produce a spiraling whorl-like pattern inferonasal to the corneal apex described as the vortex [108]. A well-known measurement to describe these patterns is tortuosity. Many variations exist for calculating tortuosity; the most common being the arc-chord ratio, described as $\tau = \frac{L}{C}$, where L is the length of the curve and C is the shortest distance between the endpoints. Al-Fahdawi et al. [81] describe the use of this measurement as a

tortuosity coefficient in their measurements of the corneal nerve fibers. This is the basis for our description of tortuosity but we also consider the closest point distance between the chord and the points that lie on the shortest line connecting the endpoints in addition to the total length of the nerve. Our tortuosity coefficient measurement is computed as follows:

$$TC_{nerves} = \frac{L}{C} \log(A + 1) \tag{6.4}$$

where the length of the endpoints is C computed by measuring the Euclidean distance between the furthest endpoints of a nerve. L is as previously described as the nerve length. A is described as the sum of the distances between each pixel on the skeleton and its corresponding closest point on the line that connected the endpoints. Examples of the tortuosity measurements described in our works are illustrated in Fig 6.5.

6.1.3   Data Acquisition & Measurements

We have three distinct groups of human subjects that make up the core data for the analysis in this chapter. This includes 10 normal subjects, 9 diabetics, and 8 subjects with trigeminal nerve lesions. For the 10 normal subjects, we only had AS-OCT data available for 7 of them. For the 9 diabetic subjects, we had AS-OCT data for 8 of them. Finally, for the 8 subjects with trigeminal nerve lesions, we had AS-OCT data for 6 of them. The IVCM imagery was available for all but one diabetic subject. We also want to make it clear that since we have one diabetic patient who had missing AS-OCT imagery and one diabetic missing IVCM imagery, it is not the same patient. IVCM data was also acquired before any methodology was set in place for montaging IVCM imagery, and as such, the imaging protocol was not developed for outputting images for potential montages. Instead, the imaging protocol was set so as to traverse through varying depths on the subject's eye to cover more than the sub-basal nerve
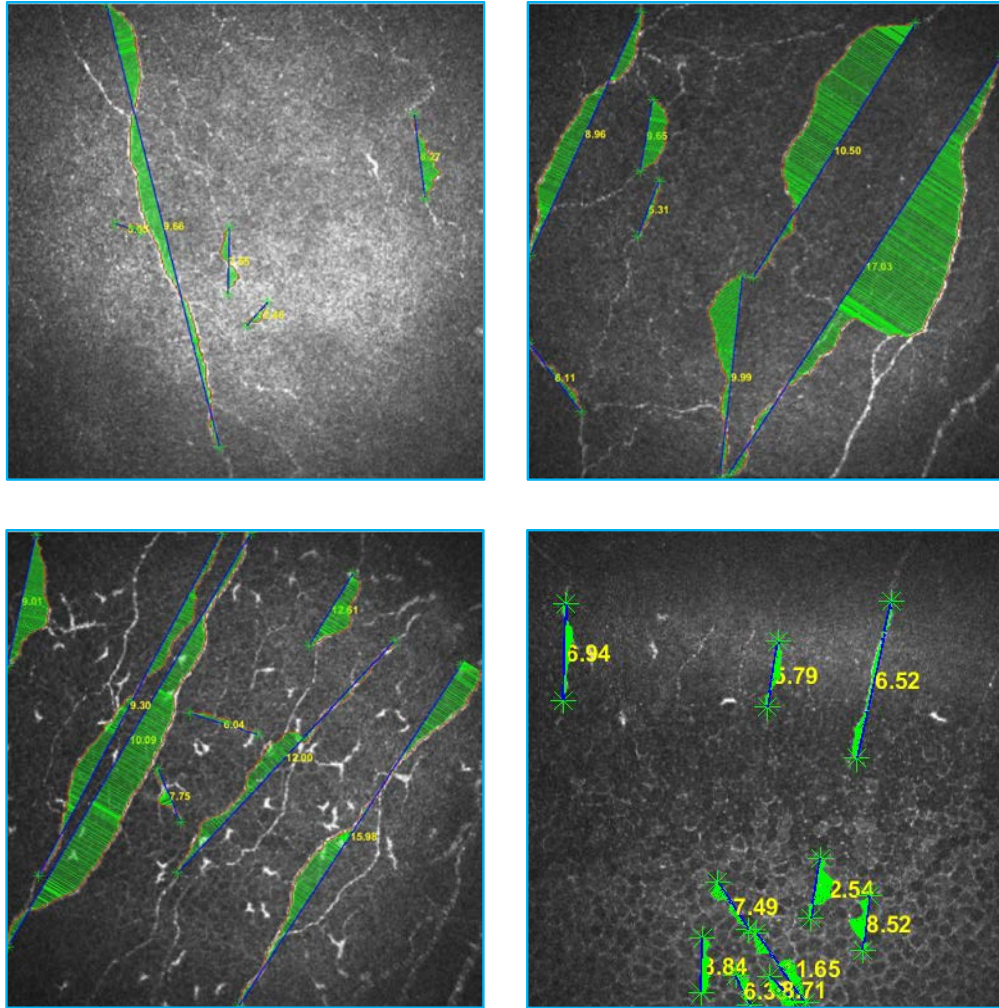
Figure 6.5: Tortuosity measurements of the nerves found in the IVCM imagery. The blue line connects the endpoints of the segmented nerve, the red path is the longest path to traverse along the skeleton between the endpoints, and the green lines are the closest point on the skeleton path w.r.t. the line connecting the endpoints. The tortuosity coefficient is displayed in yellow for each nerve.

Table 6.1: Summary of the data set available for statistical analysis of the corneal structures. It should be noted that the subject missing an AS-OCT volume from the diabetic group is not the same subject who is missing IVCM data.

Subject Group	AS-OCT Available	IVCM Available	IVCM Visits/Subject	IVCM Sessions/Visit	IVCM Total Images OD/OS
Normals (10)	7	10	5	5	250/250
Diabetics(9)	8	8	5	5	200/200
TNL (8)	6	8	1	5	40/40
Total (27)	21	26			490/490

plexus. For all the normals and all but one of the diabetics, each subject came in for 5 different visits. During each visit, the IVCM imagery was acquired from 5 distinct sequential sessions for each eye. Subjects exhibiting trigeminal nerve lesions had only one visit but were similarly scanned in 5 distinct continuous sessions for each eye during their single visit. It was also the case that during some of these sessions the imagery did not exhibit the sub-basal nerve plexus resulting in imagery without corneal nerves present. After parsing for candidate IVCM imagery exhibiting the corneal nerves and confirming AS-OCT imagery existed for the subjects, our overall data set consisted of the items summarized in Table 6.1.

We provide here a quick review of the image acquisition as previously described in Ch. 4 and Ch. 5. The AS-OCT data was acquired through raster-protocol scans using a Spectralis optical coherence tomographer (Heidelberg Engineering Inc., Carlsbad, CA) at the University of Iowa. The size of each scan was $768\times25\times242$ voxels given in the x-y-z direction, respectively at an 8-bit grayscale bit depth. The physical dimensions were 8.3 mm in the x-direction, and 2.61 mm in the z-direction with a distance of 0.69 mm in the y-direction between slices. Let us also note that 6 of the AS-OCT volumes did not have the full 25 slices available due to unknown

irregularities in the image acquisition. These volumes are the reason why we don't consider a full global volume for statistical analysis because it would show biased numbers for imagery with all slices available and instead we consider the average area in each B-scan in order to provide an even comparison among all the AS-OCT volumes.

The IVCM imagery consisted of over 980 images of the sub-basal nerve plexus corresponding to different subjects from each patient group. Each IVCM image represented a coronal section of the cornea that is 400 μm $\times$ 400 μm (384 $\times$ 384 pixels) in physical dimensions in the x-direction and y-direction respectively. The images were acquired at an 8-bit grayscale bit depth as well.

A summary of the relevant structural measurements acquired from the imagery by applying the methodologies designed in previous chapters is summarized below:

- **AS-OCT Structural Measurements**

    1. Central Thickness (Epithelial/Stromal/Total)

    2. Peripheral Thickness (Epithelial/Stromal/Total)

    3. Outer Thickness (Epithelial/Stromal/Total)

    4. B-Scan Area (Epithelial/Stroma/Total)

- **IVCM Imagery Structural Measurements**

    1. Nerve Density

    2. Mean Nerve Length

    3. Max Nerve Length

    4. Tortuosity

       The AS-OCT structural measurements were acquired from each patient as the mean measurement across all B-scans. The IVCM structural measurements were averaged across all the images from all the sessions and visits

for each subject and also averaged across all subjects in each group.

6.1.4 Statistical Analysis of Structural Measurements of Corneal Anatomy in Imaging Modalities

Once we extracted measurements, we performed statistical analysis on inter-subject groups and intra-subject structural measurements. One-way analysis of variance (ANOVA) was applied to compare the total central thicknesses, total peripheral thicknesses, total outer thicknesses and average B-scan area from AS-OCT segmentations (Fig. 6.2) in addition to density and tortuosity in IVCM imagery. The analysis was across all patient groups: normals, diabetics, and patients with trigeminal nerve lesions at a significance level $\alpha = 0.05$ to determine any statistical significance in these measurements across the patient groups. Given we tested $m = 6$ null hypotheses, after Bonferroni correction, the p-value used to determine if we reject the null hypothesis was $p < 0.05/m = 0.0083$, the null hypothesis being that the means of the OCT structural measurements across all the patient groups were the same. If the results of the ANOVA produced a significant effect, making the assumption that the normals are the control group, post hoc analysis via multiple comparison tests was applied to test the null hypothesis that the mean of the structural measurements in the experimental groups was the same as the control group.

The availability of structural measurements from different modalities and a means of comparing them for the various subject groups is also a key component in our studies. As such, we further investigated the structural measurements found in AS-OCT and IVCM imagery to determine any correlations between them. This is performed using the sample Pearson's correlation coefficient defined as:

$$\rho(x, y) = \frac{\sum_{i=1}^{n}(x_i - \bar{x})(y_i - \bar{y})}{\sqrt{\sum_{i=1}^{n}(x_i - \bar{x})^2}\sqrt{\sum_{i=1}^{n}(y_i - \bar{y})^2}} \tag{6.5}$$

where n is the sample size, x_i and y_i are the corresponding IVCM and AS-OCT measurements of the i'th patient in one of the groups of subjects (normals, diabetics,

or trigeminal nerve lesions). In addition, $\bar{x}$ and $\bar{y}$ are the sample means of the IVCM and AS-OCT measurements to be compared and were computed as:

$$\bar{x} = \frac{1}{n} \sum_{i=1}^{n} x_i \tag{6.6}$$

and

$$\bar{y} = \frac{1}{n} \sum_{i=1}^{n} y_i \tag{6.7}$$

We computed correlation coefficients with tortuosity and nerve density measurements from IVCM imagery and central corneal thickness, mean B-scan area, and epithelial thickness from AS-OCT imagery. It had been recently shown that epithelial thickness can exhibit age-related changes [109] and therefore was considered for correlation computations in our analysis.

6.2   Results

A summary of the regional and global measurements for structural measurements extracted from AS-OCT imagery is in Table 6.2. Similarly, for IVCM imagery, a summary of the measurements for each group is in Table 6.3. Plots comparing measurements between AS-OCT and IVCM imagery are shown in Fig. 6.6. The corresponding Pearson's correlation coefficients are reported in Table 6.5, Table 6.6, and Table 6.7.

The results of the ANOVA showed a statistical significance between the means of the three different subject groups when considering total central thicknesses, total peripheral thicknesses, and total outer thicknesses in AS-OCT images ($p < 0.0083$). Post-hoc analysis showed that statistical significance existed between the means of normals and diabetics and between the means of normals and patients with trigeminal nerve lesion in regards to total central thicknesses and total peripheral thicknesses ($p < 0.05$). Additionally, for IVCM measurements, the results of the ANOVA showed

no statistical significance between tortuosity measurements in the subject groups ($p > 0.0083$) but showed statistical significance between the nerve density between normals and patients with trigeminal nerve lesions.

Furthermore, the multi-modal structural measurement correlations in Table 6.5, Table 6.6, and Table 6.7 show inconclusive evidence in regards to statistical significance ($p > 0.0083$) for correlation between corneal structural measurements from the two imaging modalities. The most notable of these results is central corneal thickness versus corneal nerve density in normal subjects ($\rho = -0.815, p = 0.026$). Regardless, after Bonferonni correction we found no statistical significance to be the case.

6.3 Discussion and Conclusion

In this chapter, we implemented the use of structural measurements that could be extracted from imaging modalities for whom methodologies were developed for in previous chapters for the statistical analysis of data from various groups: normal subjects, diabetics, and patients with trigeminal nerve lesions. The methodology was implemented to determine any significance, relations, or correlations between the structural measurements in anterior-segment optical coherence tomography images depicting the corneal layers and in-vivo confocal microscopy images of the sub-basal nerve plexus depicting corneal nerves. A summary of the data set is in Table 6.1.

We implemented the use of thickness measurements of the corneal layers from AS-OCT images. The boundaries of considerable interest were the epithelial-stromal boundary, the stromal-endothelium boundary, and the boundary encompassing the entire cornea (Fig 6.1, Fig 6.2) found using the algorithm developed in Ch. 4. These translated into local epithelial thicknesses, stromal thicknesses, and total thicknesses. The region of interest for these measurements was taken at the outer boundaries, peripheral boundaries, and central location of the imagery. In addition, global measurements of volume for the areas of significant interest were computed, including epithelial area, stromal area, and total area in each slice along with the average area

Table 6.2: Mean and standard deviation of the structural measurements from AS-OCT imagery of the various subject groups.

Subject Group	Central Epithelial Thickness (Microns)	Central Stromal Thickness (Microns)	Central Total Thickness (Microns)
Normals (7)	59.80 ± 3.90	506.45 ± 24.15	566.26 ± 23.53
Diabetics (8)	59.49 ± 4.09	488.74 ± 21.54	548.23 ± 21.58
TNL (6)	60.87 ± 4.02	485.35 ± 31.45	546.22 ± 33.75
Total (21)	59.99 ± 4.04	494.10 ± 27.16	554.09 ± 27.67
	Peripheral Epithelial Thickness (Microns)	Peripheral Stromal Thickness (Microns)	Peripheral Total Thickness (Microns)
Normals (7)	58.66 ± 3.16	520.26 ± 25.08	578.92 ± 25.65
Diabetics (8)	57.63 ± 3.13	512.31 ± 22.34	569.94 ± 22.55
TNL (6)	59.21 ± 3.79	504.98 ± 36.43	564.19 ± 38.84
Total (21)	58.44 ± 3.40	513.09 ± 28.48	571.53 ± 29.56
	Outer Epithelial Thickness (Microns)	Outer Stromal Thickness (Microns)	Outer Total Thickness (Microns)
Normals (7)	56.00 ± 3.29	558.92 ± 54.17	614.92 ± 55.93
Diabetics (8)	53.04 ± 3.37	576.84 ± 34.75	629.88 ± 35.99
TNL (6)	55.15 ± 5.03	559.15 ± 54.66	614.30 ± 57.39
Total (21)	54.68 ± 4.08	565.53 ± 48.86	620.22 ± 50.53
	Epithelial Mean B-Scan Area (Microns^2)	Stromal Mean B-Scan Area (Microns^2)	Total Mean B-Scan Area (Microns^2)
Normals (7)	44854.05 ± 2319.25	402778.40 ± 20607.98	447632.44 ± 21256.93
Diabetics (8)	43903.72 ± 2254.38	398753.71 ± 17706.32	442657.43 ± 17935.92
TNL (6)	45162.09 ± 2931.58	392300.13 ± 29229.09	437462.22 ± 31107.57
Total (21)	44592.55 ± 2537.92	398388.25 ± 22800.41	442980.80 ± 23727.07

Table 6.3: Mean and standard deviation of nerve density and nerve tortuosity from IVCM imagery of the various subject groups.

Subject Group	Tortuosity Index	Nerve Density (Pixels/Area)
Normals (10)	14.25 ± 20.64	0.0438 ± 0.0157
Diabetics (8)	15.21 ± 32.14	0.0416 ± 0.0168
TNL (8)	16.04 ± 57.02	0.0270 ± 0.0130
Total (27)	14.77 ± 32.33	0.04 ± 0.02

Table 6.4: Mean and standard deviation of nerve length measurements from IVCM imagery of the various subject groups.

Subject Group	Avg. Nerve Length/Image (Microns)	Max Nerve Length/Image (Microns)
Normals (10)	380.33 ± 721.74	1253.83 ± 2986.75
Diabetics (8)	443.18 ± 1194.62	1623.99 ± 5164.68
TNL (8)	465.58 ± 2334.35	694.55 ± 2317.04
Total (27)	415.75 ± 1220.82	1341.60 ± 4130.78

Table 6.5: Correlation coefficients of the central thickness measurements in AS-OCT imagery versus nerve density and tortuosity from IVCM imagery.

Subject Group	CCT (OCT) vs Tortuosity (IVCM)	CCT (OCT) vs Density (IVCM)
Normals (7)	-0.258 ($p = 0.576$)	-0.815 ($p = 0.026$)
Diabetics (7)	0.497 ($p = 0.257$)	-0.047 ($p = 0.920$)
TNL (6)	-0.461 ($p = 0.357$)	-0.446 ($p = 0.375$)

Table 6.6: Correlation coefficients of the mean B-scan area in AS-OCT imagery versus nerve density and tortuosity from IVCM imagery.

Subject Group	Mean B-scan Area (OCT) vs Tortuosity (IVCM)	Mean B-scan Area (OCT) vs Density (IVCM)
Normals (7)	-0.595 (p = 0.159)	-0.646 (p = 0.117)
Diabetics (7)	0.434 (p = 0.331)	0.058 (p = 0.902)
TNL (6)	-0.624 (p = 0.186)	-0.496 (p = 0.317)

Table 6.7: Correlation coefficients of the epithelial thickness in AS-OCT imagery versus nerve density and tortuosity from IVCM imagery.

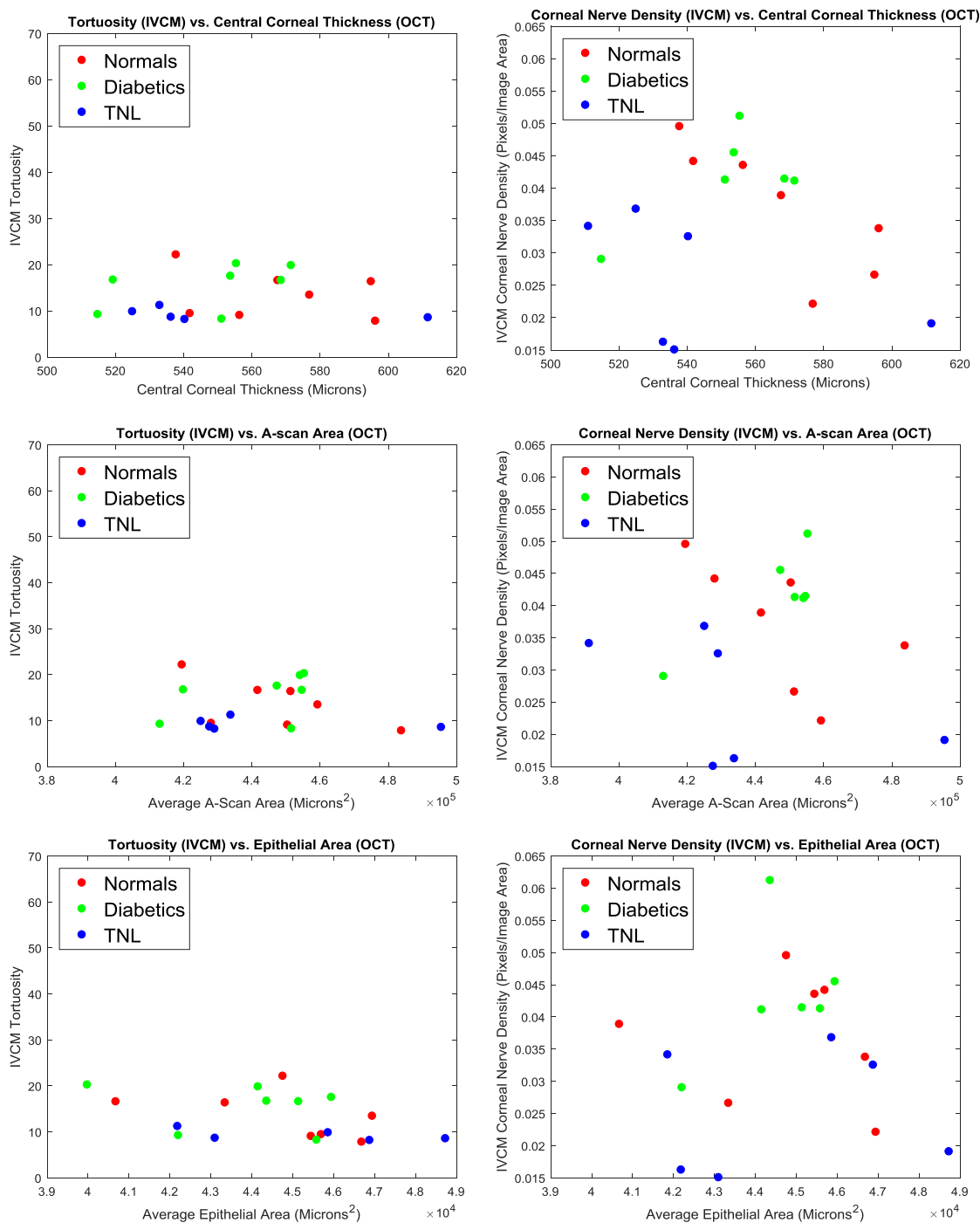| Subject Group	Epithelial Thickness (OCT) vs Density (IVCM)	Epithelial Thickness (OCT) vs Tortuosity (IVCM)
Normals (7)	-0.157 (p = 0.736)	-0.511 (p = 0.241)
Diabetics (7)	-0.001 (p = 0.998)	-0.212 (p = 0.649)
TNL (6)	0.130 (p = 0.806)	-0.537 (p = 0.272)

Figure 6.6: Plots of structural measurements of IVCM versus AS-OCT depicting possible correlations in these measurements between the imaging modalities.

among all slices. These structural measurements are shown in Table 6.2.

Furthermore, we presented the use of structural measurements describing the behavior of corneal nerves from in-vivo confocal microscopy images of the sub-basal nerve plexus (SBNP). The segmentation algorithm developed in Ch. 5 was applied to single images of the SBNP from the three subject groups from different visits and the multiple sessions within each visit. We considered the nerve density of the image along with the mean nerve length and maximum nerve length of the nerves found in each image as well as the tortuosity measurement to describe the shape of the nerves. Table 6.3 and Table 6.4 summarize these measurements. Statistical analysis using ANOVA was performed on the AS-OCT measurements, specifically the total thickness at specified regions of interest. The test showcased a statistical significance in the means between the three patient groups ($p < 0.0083$). Additionally, post-hoc analysis showed a statistical significance between the means of normals and diabetics and between the means of normals and patients with trigeminal nerve lesion in regards to total central thicknesses and total peripheral thicknesses ($p < 0.05$). This leads us to believe that the regions around the center of the cornea could exhibit a difference between normals and other patient groups. We would do well to consider further studies in confirming these findings, especially when controlling for factors like age and the time since a disease was first diagnosed or the time since physical trauma was induced.

We also considered comparing measurements across imaging modalities to determine any correlation between the subject groups. The correlation coefficients shown in Table 6.5, Table 6.6, and Table 6.7 leads us to believe that, at the moment, only inconclusive evidence exists for correlating structural measurements across the imaging modalities in our work. Even if conclusive evidence or statistical significance were to exist it would still prove difficult to support those claims due to the exiguous amount of data. As it stands, the analysis in this chapter still showed promising value for the

consideration of the structural measurements from the imagery involved. The future continuation of this work would need to entail a larger data set for higher statistical power. In addition, future works would be wise to include imaging protocols that could take advantage of the image stitching algorithm for IVCM imagery encompassing larger regions of interest and imaging protocols of AS-OCT able to differentiate the various corneal layers at a higher resolution to consider thicknesses of specific layers and areas.

To summarize, our method proved effective for extracting structural measurements from corneal imaging modalities. The results from the segmentation algorithms along with the methodology for extracting measurements presented in this chapter confirmed the algorithms' place as automated alternatives to manual measurement of corneal structures. We were also pleased to find the methods developed in previous chapters adapted to imagery from a new data set with no modifications. Overall, we also believe in future potential in using the methodologies implemented herein for studying ophthalmic diseases and their impact on the corneal structures.

CHAPTER 7
CONCLUSION

The overall cornerstone of our work was to exploit the non-invasive nature of imaging modalities to examine the changes in corneal structures. The works created in our thesis were three-fold. Aim 1 was to develop an algorithm that segmented the corneal layers in the eye using AS-OCT of humans and murine. Aim 2 was to develop an algorithm that created a montage of in vivo confocal microscopy (IVCM) images of the corneal sub-basal nerve plexus and segment the corneal nerves in single and montage images. Finally, Aim 3 considered the correlation and statistical analysis of structural measurements of the cornea. This aim included a culmination of the previous algorithms to extract corneal structures from multiple imaging modalities in various subject groups for use in observing corneal structure differences among the subject groups.

The graph-based algorithm implemented in Ch. 4 proved effective in segmenting the corneal layers in anterior segment-optical coherency tomography imagery to find the air-epithelium, Bowman's layer-stroma boundary, and the endothelium-aqueous humor boundary. The approach was successful for segmenting 58 murine images and 37 human images utilizing the shape-prior information of the cornea that was incorporated into the graph-theoretic approach. The total unsigned border positioning error for the mouse data set was 4.36 ± 4.13 μm (2.85 ± 2.70 pixels) and for the human data set it was 13.67 ± 12.72 μm (1.27 ± 1.18 pixels). The method differed from prior works [12–14, 16, 17, 19, 20, 71] due mainly to its novelty in segmenting all the surface simultaneously in 3D whereas previous approaches segmented boundaries as a combination of 2D techniques on individual surfaces, in automated or semi-automated fashions. The limitations of this algorithm became apparent when considering a trade-off between robustness and accuracy. The smoothness constraints of the graph algorithm can be finely tuned for an assemblage of corneal layer thicknesses giving

rise to a narrow but more accurate segmentation. On the opposite side of the spectrum, it can also allow for a larger variety of expected thicknesses in AS-OCT images allowing for the ability to include a larger variety of data but at a loss of segmentation accuracy. To the best of our knowledge, this was also the only approach to have segmented murine data providing support to the robustness of the method in being able to evaluate corneal structures of varying physical dimensions.

The montaging and segmentation algorithm from Ch. 5 was able to successfully detect overlapping imagery and segment the corneal nerves contained within in-vivo confocal microscopy images of the sub-basal nerve plexus. The registration approach was developed using four data sets of IVCM imagery containing between 84-221 IVCM images per set with evaluations of registration applied on 100 image pairs. The registration algorithm proved accurate with the distance between the manually transformed points and their automated counterparts being $2.13 \pm 1.10 \ \mu$m. We also found statistically smaller errors when using the automated method versus using manual registration techniques ($p < 0.05$) giving way to our registration approach as an alternative method versus manual implementations. The segmentation algorithm was developed using 52 IVCM single images with a support vector machine to perform pixel classification via testing and training on the 52 images. The performance was evaluated based on the sensitivity, specificity, and accuracy of the machine learning output where at the optimal operating point the sensitivity was 0.79, the specificity was 0.75, and the accuracy was 77.41%. Our current work relies on the assumption that we find all possible image montages so an ostensible disadvantage of our work could be its lack of validation for determining if the algorithm successfully found all image montages in a data set. The notable distinction of our works as compared to previous methodologies [30, 77–80] is that it did not make assumptions on image order *a priori* and could be implemented without a need to substantially modify the existing imaging protocols or imaging hardware/software interface. It has the poten-

tial as a basis for an off-line unsupervised method for quantitative analysis of corneal structures in confocal microscopy imagery.

In the conclusions to our work, we implemented the use of structural measurements in Ch. 6 for the statistical analysis of said measurements from various groups: normal subjects, diabetics, and patients with trigeminal nerve lesions. We considered the use of thickness measurements of the corneal layers from AS-OCT images and structural measurements describing the behavior of corneal nerves from in-vivo confocal microscopy images of the sub-basal nerve plexus. These measurements were extracted by using methodologies implemented in previous chapters for new applicative use. Statistical tests via analysis of variance (ANOVA) was performed on the AS-OCT measurements, specifically the total thickness at specified regions of interest showcasing statistical significance in the means between the three patient groups ($p < 0.0167$). Post-hoc analysis showed a statistical significance between the means of normals and diabetics and between the means of normals and patients with trigeminal nerve lesion in regards to total central thicknesses and total peripheral thicknesses ($p < 0.05$). We also considered comparing measurements across imaging modalities to determine any correlation for the subject groups but even through simple visual inspection of the reported correlation coefficients, we found that the p-values would likely be much higher than a typical significant level $\alpha = 0.05$ commonly used for statistical significance testing. This leads us to believe that only inconclusive evidence exists for correlating structural measurements across imaging modalities from our data set. It became apparent that the exiguous amount of data in our work would result in said evidence.

We believe the future continuation of this work needs to entail a larger data set for higher statistical power to support any claims as a result of statistical analysis. Future works would also be wise to implement imaging protocols that take advantage of the image stitching algorithm for IVCM imagery encompassing larger regions of

interest and imaging protocols of AS-OCT able to differentiate the various corneal layers at a higher resolution to consider thicknesses of specific layers and areas for analysis. To summarize, our methodologies proved effective for extracting structural measurements from corneal imaging modalities for the statistical analysis of the corneal structures. The method also showcased the robustness of methods developed in previous chapters to adapt to imagery from differentiating data sets. Overall, we believe in future potential in using the methodologies developed herein for studying diseases that impact the corneal structures.

REFERENCES

[1] D. Huang, E. A. Swanson, C. P. Lin, J. S. Schuman, W. G. Stinson, W. Chang, M. R. Hee, T. Flotte, K. Gregory, and C. A. Puliafito, "Optical coherence tomography," *Science*, vol. 254, no. 5035, pp. 1178–1181, Nov. 1991.

[2] J. A. Izatt, M. R. Hee, E. A. Swanson, C. P. Lin, D. Huang, J. S. Schuman, C. A. Puliafito, and J. G. Fujimoto, "Micrometer-scale resolution imaging of the anterior eye in vivo with optical coherence tomography," *Arch. Ophthalmol.*, vol. 112, no. 12, pp. 1584–1589, Dec 1994.

[3] E. Silversmith, "Schematic diagram of the human eye with English annotations," 2006, [Online; accessed June 29, 2016]. [Online]. Available: https://en.wikipedia.org/wiki/File:Schematic_diagram_of_the_human_eye_with _English_annotations.svg

[4] M. Minsky, "Memoir on inventing the confocal scanning microscope," *Scanning*, vol. 10, no. 4, pp. 128–138, 1988.

[5] I. Jalbert, F. Stapleton, E. Papas, D. F. Sweeney, and M. Coroneo, "In vivo confocal microscopy of the human cornea," *Br. J. Ophthalmol.*, vol. 87, no. 2, pp. 225–236, Feb 2003.

[6] B. E. Klein, R. Klein, W. E. Sponsel, T. Franke, L. B. Cantor, J. Martone, and M. J. Menage, "Prevalence of glaucoma. the beaver dam eye study," *Ophthalmology*, vol. 99, no. 10, p. 1499, 1992.

[7] D. S. Friedman, R. C. Wolfs, B. J. Ocolmain, B. E. Klein, H. R. Taylor, S. West, M. C. Leske, P. Mitchell, N. Congdon, and J. Kempen, "Prevalence of open-angle glaucoma among adults in the united states," *Arch. Ophthalmol.*, vol. 22, no. 4, p. 532, 2004.

[8] F. A. Medeiros, P. A. Sample, L. M. Zangwill, C. Bowd, M. Aihara, and R. N. Weinreb, "Corneal thickness as a risk factor for visual field loss in patients with preperimetric glaucomatous optic neuropathy," *Am. J. Ophthalmol.*, vol. 136, no. 5, pp. 805–813, 2003.

[9] "Statistics About Diabetes," http://www.diabetes.org/diabetes-basics/statistics/?loc=db-slabnav note = Accessed: 2016-02-16.

[10] N. V. Nielsen and F. S. Lund, "Diabetic polyneuropathy, corneal sensitivity, vibratory perception and Achilles tendon reflex in diabetics," *Acta Neurol. Scand.*, vol. 59, no. 1, pp. 15–22, Jan 1979.

[11] M. E. Rosenberg, T. M. Tervo, I. J. Immonen, L. J. Muller, C. Gronhagen-Riska, and M. H. Vesaluoma, "Corneal structure and sensitivity in type 1 diabetes mellitus," *Invest. Ophthalmol. Vis. Sci.*, vol. 41, no. 10, pp. 2915–2921, Sep 2000.

[12] F. Graglia, J. L. Mari, G. Baikoff, and J. Sequeira, "Contour detection of the cornea from OCT radial images," *Conf. Proc. IEEE Eng. Med. Biol. Soc.*, vol. 2007, pp. 5612–5615, 2007.

[13] J. A. Eichel, K. K. Bizheva, D. A. Clausi, and P. W. Fieguth, "Automated 3-D reconstruction and segmentation from optical coherence tomography," in *Proceedings of the 11th European Conference on Computer Vision: Part III*, ser. ECCV'10.   Berlin, Heidelberg: Springer-Verlag, 2010, pp. 44–57.

[14] F. LaRocca, S. J. Chiu, R. P. McNabb, A. N. Kuo, J. A. Izatt, and S. Farsiu, "Robust automatic segmentation of corneal layer boundaries in SD-OCT images using graph theory and dynamic programming," *Biomed. Opt. Express*, vol. 2, no. 6, pp. 1524–1538, 2011.

[15] V. A. Robles, B. J. Antony, D. R. Koehn, M. G. Anderson, and M. K. Garvin, "3D graph-based automated segmentation of corneal layers in anterior-segment optical coherence tomography images of mice," *Proc. SPIE*, vol. 9038, pp. 90 380F–90 380F–7, 2014.

[16] M. K. Jahromi, R. Kafieh, H. Rabbani, A. M. Dehnavi, A. Peyman, F. Hajizadeh, and M. Ommani, "An automatic algorithm for segmentation of the boundaries of corneal layers in optical coherence tomography images using Gaussian mixture model," *J. Med. Signals. Sens.*, vol. 4, no. 3, pp. 171–180, Jul 2014.

[17] D. Williams, Y. Zheng, F. Bao, and A. Elsheikh, "Fast segmentation of anterior segment optical coherence tomography images using graph cut," *Eye and Vision*, vol. 2, no. 1, 2015.

[18] J. W. Console, L. M. Sakata, T. Aung, D. S. Friedman, and M. He, "Quantitative analysis of anterior segment optical coherence tomography images: the Zhongshan Angle Assessment Program," *Br. J. Ophthalmol.*, vol. 92, no. 12, pp. 1612–1616, Dec 2008.

[19] M. Ang, W. Chong, H. Huang, W. T. Tay, T. Y. Wong, M. G. He, T. Aung, and J. S. Mehta, "Comparison of anterior segment optical tomography parameters measured using a semi-automatic software to standard clinical instruments," *PLoS ONE*, vol. 8, no. 6, p. e65559, 2013.

[20] E. Kim and K. Ehrmann, "Assessment of accuracy and repeatability of anterior segment optical coherence tomography and reproducibility of measurements using a customized software program," *Clin. Exp. Optom.*, vol. 95, no. 4, pp. 432–441, Jul 2012.

[21] F. Scarpa, E. Grisan, and A. Ruggeri, "Automatic recognition of corneal nerve structures in images from confocal microscopy," *Invest. Ophthalmol. Vis. Sci.*, vol. 49, no. 11, pp. 4801–4807, Nov 2008.

[22] M. A. Dabbah, J. Graham, I. N. Petropoulos, M. Tavakoli, and R. A. Malik, "Automatic analysis of diabetic peripheral neuropathy using multi-scale quantitative morphology of nerve fibres in corneal confocal microscopy imaging," *Med. Image Anal.*, vol. 15, no. 5, pp. 738–747, Oct 2011.

[23] A. Ferreira, A. M. Morgado, and J. S. Silva, "A method for corneal nerves automatic segmentation and morphometric analysis," *Computer Methods and Programs in Biomedicine*, vol. 107, no. 1, pp. 53 – 60, 2012, advances in Biomedical Engineering and Computing: the MEDICON conference case.

[24] E. Poletti and A. Ruggeri, "Automatic nerve tracking in confocal images of corneal subbasal epithelium," in *Proceedings of the 26th IEEE International Symposium on Computer-Based Medical Systems*, June 2013, pp. 119–124.

[25] P. Guimaraes, J. Wigdahl, E. Poletti, and A. Ruggeri, "A fully-automatic fast segmentation of the sub-basal layer nerves in corneal images," *Conf. Proc. IEEE. Eng. Med. Biol. Soc.*, vol. 2014, pp. 5422–5425, 2014.

[26] R. Annunziata, A. Kheirkhah, S. Aggarwal, P. Hamrah, and E. Trucco, "A fully automated tortuosity quantification system with application to corneal nerve fibres in confocal microscopy images," *Med. Image Anal.*, vol. 32, pp. 216–232, Aug 2016.

[27] X. Chen, J. Graham, M. Dabbah, I. Petropoulos, M. Tavakoli, and R. Malik, "An automatic tool for quantification of nerve fibres in corneal confocal microscopy images," *IEEE. Trans. Biomed. Eng.*, Jun 2016.

[28] D. V. Patel and C. N. McGhee, "Mapping of the normal human corneal sub-basal nerve plexus by in vivo laser scanning confocal microscopy," *Invest. Ophthalmol. Vis. Sci.*, vol. 46, no. 12, pp. 4485–4488, Dec 2005.

[29] X. Fan and S. Xia, *Feature Based Automatic Stitching of Microscopic Images*, D.-S. Huang, L. Heutte, and M. Loog, Eds. Berlin, Heidelberg: Springer Berlin Heidelberg, 2007.

[30] J. T. Turuwhenua, D. V. Patel, and C. N. McGhee, "Fully automated montaging of laser scanning in vivo confocal microscopy images of the human corneal subbasal nerve plexus," *Invest. Ophthalmol. Vis. Sci.*, vol. 53, no. 4, pp. 2235–2242, Apr 2012.

[31] P. Guimaraes, J. Wigdahl, and A. Ruggeri, "A fast and efficient technique for the automatic tracing of corneal nerves in confocal microscopy," *Transl. Vis. Sci. Technol.*, vol. 5, no. 5, p. 7, Sep 2016.

[32] B. Cassin and S. Solomon, "Dictionary of Eye Terminology," 1990.

[33] K. KR, *Morphology and pathologic responses of the cornea to disease*, ser. The Cornea. Scientific Foundations and Clinical Practice. Little, Brown & Co, 1983.

[34] C. Oyster, *The human eye: structure and function.* Sinauer, 1999.

[35] S. E. Wilson and J. W. Hong, "Bowman's layer structure and function: critical or dispensable to corneal function? A hypothesis," *Cornea*, vol. 19, no. 4, pp. 417–420, Jul 2000.

[36] N. Lagali, J. Germundsson, and P. Fagerholm, "The role of Bowman's layer in corneal regeneration after phototherapeutic keratectomy: a prospective study using in vivo confocal microscopy," *Invest. Ophthalmol. Vis. Sci.*, vol. 50, no. 9, pp. 4192–4198, Sep 2009.

[37] R. F. Guthoff, H. Wienss, C. Hahnel, and A. Wree, "Epithelial innervation of human cornea: a three-dimensional study using confocal laser scanning fluorescence microscopy," *Cornea*, vol. 24, no. 5, pp. 608–613, Jul 2005.

[38] Y. Tamura, H. Konomi, H. Sawada, S. Takashima, and A. Nakajima, "Tissue distribution of type VIII collagen in human adult and fetal eyes," *Invest. Ophthalmol. Vis. Sci.*, vol. 32, no. 9, pp. 2636–2644, Aug 1991.

[39] D. S. Friedman, R. C. W. Wolfs, B. J. O'Colmain, B. E. Klein, H. R. Taylor, S. West, M. C. Leske, P. Mitchell, N. Congdon, and J. Kempen, "Prevalence of open-angle glaucoma among adults in the United States." *Arch. Ophthalmol.*, vol. 122, no. 4, pp. 532–8, Apr 2004.

[40] H. A. Quigley and A. T. Broman, "The number of people with glaucoma worldwide in 2010 and 2020," *B. J. Ophthalmol*, vol. 90, no. 3, pp. 262–267, 2006.

[41] B. K. Nayak, Q. B. Maskati, and R. Parikh, "The unique problem of glaucoma: under-diagnosis and over-treatment." *Indian. J. Ophthalmol.*, vol. 59 Suppl, pp. S1–2, Jan 2011.

[42] Petr Kratochvil, "Eyeball sculpture," [Online; accessed June 29 2016]. [Online]. Available: http://www.publicdomainpictures.net/pictures/30000/velka/mom-and-child-in-autumn.jpg

[43] A. T. Broman, N. G. Congdon, K. Bandeen-Roche, and H. A. Quigley, "Influence of corneal structure, corneal responsiveness, and other ocular parameters on tonometric measurement of intraocular pressure," *J. Glaucoma*, vol. 16, no. 7, pp. 581–588, 2007.

[44] C. Y. Shih, J. S. Graff Zivin, S. L. Trokel, and J. C. Tsai, "Clinical significance of central corneal thickness in the management of glaucoma," *Arch. Ophthalmol.*, vol. 122, no. 9, pp. 1270–1275, Sep 2004.

[45] H. Goldmann and T. Schmidt, "Applanation tonometry," *Ophthalmologica*, vol. 134, no. 4, pp. 221–42, Oct 1957.

[46] N. Ehlers, F. K. Hansen, and H. Aasved, "Biometric correlations of corneal thickness." *Acta. Ophthalmol. (Copenh.)*, vol. 53, no. 4, pp. 652–9, Sep 1975.

[47] N. Ehlers and F. K. Hansen, "Central corneal thickness in low-tension glaucoma." *Acta. Ophthalmol. (Copenh.)*, vol. 52, no. 5, pp. 740–6, 1974.

[48] N. Ehlers, T. Bramsen, and S. Sperling, "Applanation tonometry and central corneal thickness." *Acta. Ophthalmol. (Copenh.)*, vol. 53, no. 1, pp. 34–43, Mar 1975.

[49] E. Aghaian, J. E. Choe, S. Lin, and R. L. Stamper, "Central corneal thickness of Caucasians, Chinese, Hispanics, Filipinos, African Americans, and Japanese in a glaucoma clinic," *Ophthalmology*, vol. 111, no. 12, pp. 2211–2219, Dec 2004.

[50] A. E. Kitabchi, G. E. Umpierrez, J. M. Miles, and J. N. Fisher, "Hyperglycemic crises in adult patients with diabetes," *Diabetes Care*, vol. 32, no. 7, pp. 1335–1343, Jul 2009.

[51] K. Skarbez, Y. Priestley, M. Hoepf, and S. B. Koevary, "Comprehensive review of the effects of diabetes on ocular health," *Expert. Rev. Ophthalmol.*, vol. 5, no. 4, pp. 557–577, Aug 2010.

[52] J. Saito, M. Enoki, M. Hara, N. Morishige, T. Chikama, and T. Nishida, "Correlation of corneal sensation, but not of basal or reflex tear secretion, with the stage of diabetic retinopathy," *Cornea*, vol. 22, no. 1, pp. 15–18, Jan 2003.

[53] K. C. Yoon, S. K. Im, and M. S. Seo, "Changes of tear film and ocular surface in diabetes mellitus," *Korean. J. Ophthalmol.*, vol. 18, no. 2, pp. 168–174, Dec 2004.

[54] R. A. Hyndiuk, E. L. Kazarian, R. O. Schultz, and S. Seideman, "Neurotrophic corneal ulcers in diabetes mellitus," *Arch. Ophthalmol.*, vol. 95, no. 12, pp. 2193–2196, 1977.

[55] D. Cogan, *Neurology of the ocular muscles*. Thomas, 1956. [Online]. Available: https://books.google.com/books?id=gF0uAAAAIAAJ

[56] F. Walsh and W. Hoyt, *Clinical neuro-ophthalmology*, ser. Clinical Neuro-ophthalmology. Williams & Wilkins, 1969, no. v. 3. [Online]. Available: https://books.google.com/books?id=z6xsAAAAMAAJ

[57] J. Spillane, *An Atlas of Clinical Neurology*, ser. Oxford medical publications. Oxford University Press, Incorporated, 1975. [Online]. Available: https://books.google.com/books?id=We5rAAAAMAAJ

[58] A. Brodal, *Neurological Anatomy in Relation to Clinical Medicine*, ser. Books of related interest. Oxford University Press, 1981. [Online]. Available: https://books.google.com/books?id=Wa1qAAAAMAAJ

[59] S. Gilman, *Clinical Examination of the Nervous System*. McGraw-Hill, Health Professions Division, 2000. [Online]. Available: https://books.google.com/books?id=galrAAAAMAAJ

[60] P. Hamrah, A. Cruzat, M. H. Dastjerdi, L. Zheng, B. M. Shahatit, H. A. Bayhan, R. Dana, and D. Pavan-Langston, "Corneal sensation and subbasal nerve alterations in patients with herpes simplex keratitis: an in vivo confocal microscopy study," *Ophthalmology*, vol. 117, no. 10, pp. 1930–1936, Oct 2010.

[61] A. Cruzat, D. Pavan-Langston, and P. Hamrah, "In vivo confocal microscopy of corneal nerves: analysis and clinical correlation," *Semin. Ophthalmol.*, vol. 25, no. 5-6, pp. 171–177, 2010.

[62] K. Li, X. Wu, D. Chen, and M. Sonka, "Optimal surface segmentation in volumetric images–a graph-theoretic approach," *IEEE Trans. Pattern Anal. Mach. Intell.*, vol. 28, no. 1, pp. 119–134, 2006.

[63] M. Wojtkowski, R. Leitgeb, A. Kowalczyk, T. Bajraszewski, and A. F. Fercher, "In vivo human retinal imaging by Fourier domain optical coherence tomography," *J. Biomed. Opt.*, vol. 7, no. 3, pp. 457–463, Jul. 2002.

[64] M. Wojtkowski, T. Bajraszewski, I. Gorczyńska, P. Targowski, A. Kowalczyk, W. Wasilewski, and C. Radzewicz, "Ophthalmic imaging by spectral optical coherence tomography," *Am. J. Ophthalmol.*, vol. 138, no. 3, pp. 412–419, Sep. 2004.

[65] M. Wojtkowski, V. Srinivasan, J. G. Fujimoto, T. Ko, J. S. Schuman, A. Kowalczyk, and J. S. Duker, "Three-dimensional retinal imaging with high-speed ultrahigh-resolution optical coherence tomography," *Ophthalmology*, vol. 112, no. 10, pp. 1734–1746, Oct. 2005.

[66] A. F. Fercher, C. K. Hitzenberger, G. Kamp, and S. Y. El-Zaiat, "Measurement of intraocular distances by backscattering spectral interferometry," *Optics Communications*, vol. 117, pp. 43–48, Feb. 1995.

[67] J. M. Schmitt, "Optical coherence tomography (OCT): a review," *IEEE Journal of Selected Topics in Quantum Electronics*, vol. 5, no. 4, pp. 1205–1215, Jul 1999.

[68] D. C. DeBuc, "A review of algorithms for segmentation of retinal image data using optical coherence tomography," in *Image Segmentation*, P.-G. Ho, Ed. InTech, 2011.

[69] K. Lee, M. Niemeijer, M. K. Garvin, Y. H. Kwon, M. Sonka, and M. D. Abràmoff, "Segmentation of the optic disc in 3D-OCT scans of the optic nerve head," *IEEE Trans. Med. Imag.*, vol. 29, no. 1, pp. 159–168, 2010.

[70] M. D. Abràmoff, K. Lee, M. Niemeijer, W. L. M. Alward, E. C. Greenlee, M. K. Garvin, M. Sonka, and Y. H. Kwon, "Automated segmentation of the cup and rim from spectral domain OCT of the optic nerve head," *Invest. Ophthalmol. Vis. Sci.*, vol. 50, no. 12, pp. 5778–5784, Dec. 2009.

[71] Y. Li, R. Shekhar, and D. Huang, "Segmentation of 830-nm and 1310-nm LASIK corneal optical coherence tomography images," pp. 167–178, 2002.

[72] R. Szeliski, "Image alignment and stitching: A tutorial," *Foundations and Trends in Computer Graphics and Computer Vision*, vol. 2, no. 1, December 2006.

[73] D. G. Lowe, "Object recognition from local scale-invariant features," in *Proceedings of the International Conference on Computer Vision-Volume 2 - Volume 2*, ser. ICCV '99.   Washington, DC, USA: IEEE Computer Society, 1999, pp. 1150–.

[74] M. Brown and D. G. Lowe, "Automatic panoramic image stitching using invariant features," *Int. J. Comput. Vision*, vol. 74, no. 1, pp. 59–73, Aug. 2007.

[75] D. G. Lowe, "Distinctive image features from scale-invariant keypoints," *International Journal of Computer Vision*, vol. 60, no. 2, pp. 91–110.

[76] N. Dalal and B. Triggs, "Histograms of oriented gradients for human detection," in *Computer Vision and Pattern Recognition, 2005. CVPR 2005. IEEE Computer Society Conference on*, vol. 1, June 2005, pp. 886–893 vol. 1.

[77] A. Zhivov, M. Blum, R. Guthoff, and O. Stachs, "Real-time mapping of the subepithelial nerve plexus by in vivo confocal laser scanning microscopy," *Br. J. Ophthalmol.*, vol. 94, no. 9, pp. 1133–1135, Sep 2010.

[78] N. Pritchard, K. Edwards, A. M. Shahidi, G. P. Sampson, A. W. Russell, R. A. Malik, and N. Efron, "Corneal markers of diabetic neuropathy," *Ocul. Surf.*, vol. 9, no. 1, pp. 17–28, Jan 2011.

[79] E. Poletti, J. Wigdahl, P. Guimaraes, and A. Ruggeri, "Automatic montaging of corneal sub-basal nerve images for the composition of a wide-range mosaic," *Conf. Proc. IEEE Eng. Med. Biol. Soc.*, vol. 2014, pp. 5426–5429, 2014.

[80] S. Allgeier, S. Maier, R. Mikut, S. Peschel, K. M. Reichert, O. Stachs, and B. Kohler, "Mosaicking the subbasal nerve plexus by guided eye movements," *Invest. Ophthalmol. Vis. Sci.*, vol. 55, no. 9, pp. 6082–6089, Aug 2014.

[81] S. Al-Fahdawi, R. Qahwaji, A. S. Al-Waisy, S. Ipson, R. A. Malik, A. Brahma, and X. Chen, "A fully automatic nerve segmentation and morphometric parameter quantification system for early diagnosis of diabetic neuropathy in corneal images," *Comput. Methods. Programs. Biomed.*, vol. 135, pp. 151–166, Oct 2016.

[82] X. Wu and D. Z. Chen, "Optimal net surface problems with applications," in *Proc. of the 29th International Colloquium on Automata, Languages, and Programming (ICALP), LNCS 2380.*   Springer-Verlag, 2002, pp. 1029–1042.

[83] M. K. Garvin, M. D. Abràmoff, X. Wu, S. R. Russell, T. L. Burns, and M. Sonka, "Automated 3-D intraretinal layer segmentation of macular spectral-domain optical coherence tomography images," *IEEE Trans. Med. Imag.*, vol. 28, no. 9, pp. 1436–1447, 2009.

[84] M. Haeker, X. Wu, M. D. Abàmoff, R. Kardon, and M. Sonka, "Incorporation of regional information in optimal 3-D graph search with application for intraretinal layer segmentation of optical coherence tomography images," in *Information Processing in Medical Imaging (IPMI)*, vol. 4587, no. 1. Springer-Verlag, Jan. 2007, pp. 607–618.

[85] M. Mohammad Saleh, "A multimodal machine-learning graph-based approach for segmenting glaucomatous optic nerve head structures from SD-OCT volumes and fundus photographs," Ph.D. dissertation, University of Iowa, 2016.

[86] Q. Song, J. Bai, M. K. Garvin, M. Sonka, J. M. Buatti, and X. Wu, "Optimal multiple surface segmentation with shape and context priors," *IEEE Trans. Med. Imag.*, vol. 32, no. 2, pp. 376–386, Feb. 2013.

[87] J. D. Brandt, M. O. Gordon, F. Gao, J. A. Beiser, J. P. Miller, and M. A. Kass, "Adjusting intraocular pressure for central corneal thickness does not improve prediction models for primary open-angle glaucoma," *Ophthalmology*, vol. 119, no. 3, pp. 437–442, Mar 2012.

[88] W. S. Cleveland, *Visualizing Data*. Hobart Press, 1993.

[89] J. Fox, "Robust regression: Appendix to an r and s-plus companion to applied regression," 2002.

[90] J. Beaufort, "Eyeball sculpture," 2006, [Online; accessed June 29 2016]. [Online]. Available: http://www.publicdomainpictures.net/pictures/180000/velka/eyeball-sculpture.jpg

[91] E. Poletti, G. Benedetti, and A. Ruggeri, "Super-image mosaic of infant retinal fundus: selection and registration of the best-quality frames from videos," *Conf Proc IEEE Eng Med Biol Soc*, vol. 2013, pp. 5883–5886, 2013.

[92] E. Rosten and T. Drummond, "Fusing points and lines for high performance tracking," in *Proceedings of the Tenth IEEE International Conference on Computer Vision - Volume 2*, ser. ICCV '05. Washington, DC, USA: IEEE Computer Society, 2005, pp. 1508–1515.

[93] M. S. Miri, K. Lee, M. Niemeijer, M. D. Abràmoff, Y. H. Kwon, and M. K. Garvin, "Multimodal segmentation of optic disc and cup from stereo fundus and SD-OCT images," in *Proc. SPIE, Med. Img. 2013: Img. Proc.*, vol. 8669, Orlando, Florida, Mar. 2013, p. 86690O (9pages).

[94] T. M. Cover and J. A. Thomas, *Elements of Information Theory (Wiley Series in Telecommunications and Signal Processing)*. Wiley-Interscience, 1991.

[95] M. Ceccarelli, M. Di Bisceglie, C. Galdi, G. Giangregorio, and S. L. Ullo, "Image registration using non-linear diffusion," in *International Geoscience and Remote Sensing Symposium (IGARSS)*, vol. 5, 2008, pp. V220–V223. [Online]. Available: www.scopus.com

[96] R. C. Gonzalez and R. E. Woods, *Digital Image Processing (4th Edition)*. Pearson, 2017.

[97] B. A. Wallace, "Merging and transformation of raster images for cartoon animation," *SIGGRAPH Comput. Graph.*, vol. 15, no. 3, pp. 253–262, Aug. 1981. [Online]. Available: http://doi.acm.org/10.1145/965161.806813

[98] T. Porter and T. Duff, "Compositing digital images," in *Proceedings of the 11th Annual Conference on Computer Graphics and Interactive Techniques*, ser. SIGGRAPH '84. New York, NY, USA: ACM, 1984, pp. 253–259. [Online]. Available: http://doi.acm.org/10.1145/800031.808606

[99] "A threshold selection method from gray-level histograms," *IEEE Transactions on Systems, Man, and Cybernetics*, vol. 9, no. 1, pp. 62–66, Jan 1979.

[100] D. J. Field, "Relations between the statistics of natural images and the response properties of cortical cells," *J Opt Soc Am A*, vol. 4, no. 12, pp. 2379–2394, Dec 1987.

[101] S. Fischer, F. Šroubek, L. Perrinet, R. Redondo, and G. Cristóbal, "Self-invertible 2D log-Gabor wavelets," *International Journal of Computer Vision*, vol. 75, no. 2, pp. 231–246, Nov 2007. [Online]. Available: https://doi.org/10.1007/s11263-006-0026-8

[102] D. Boukerroui, J. A. Noble, and M. Brady, "On the choice of band-pass quadrature filters," *Journal of Mathematical Imaging and Vision*, vol. 21, no. 1, pp. 53–80, Jul 2004. [Online]. Available: https://doi.org/10.1023/B:JMIV.0000026557.50965.09

[103] G. H. Granlund and H. Knutsson, *Signal processing for computer vision.* Springer Science & Business Media, 2013.

[104] A. F. Frangi, W. J. Niessen, K. L. Vincken, and M. A. Viergever, *Multiscale vessel enhancement filtering.* Berlin, Heidelberg: Springer Berlin Heidelberg, 1998, pp. 130–137. [Online]. Available: https://doi.org/10.1007/BFb0056195

[105] C. Cortes and V. Vapnik, "Support-vector networks," *Mach. Learn.*, vol. 20, no. 3, pp. 273–297, Sep. 1995. [Online]. Available: https://doi.org/10.1023/A:1022627411411

[106] T. Hastie, R. Tibshirani, and J. Friedman, *The Elements of Statistical Learning: Data Mining, Inference, and Prediction, Second Edition (Springer Series in Statistics).* Springer, 2009.

[107] N. Cristianini and J. Shawe-Taylor, *An Introduction to Support Vector Machines and Other Kernel-based Learning Methods.* Cambridge University Press, 2000.

[108] T. Utsunomiya, T. Nagaoka, K. Hanada, T. Omae, H. Yokota, A. Abiko, M. Haneda, and A. Yoshida, "Imaging of the corneal subbasal whorl-like nerve plexus: more accurate depiction of the extent of corneal nerve damage in patients with diabetes," *Investigative Ophthalmology & Visual Science*, vol. 56, no. 9, p. 5417, 2015.

[109] Y. Yang, J. Hong, S. X. Deng, and J. Xu, "Age-related changes in human corneal epithelial thickness measured with anterior segment optical coherence tomography," *Invest. Ophthalmol. Vis. Sci.*, vol. 55, no. 8, pp. 5032–5038, Jul 2014.